



저작자표시-비영리-변경금지 2.0 대한민국

이용자는 아래의 조건을 따르는 경우에 한하여 자유롭게

- 이 저작물을 복제, 배포, 전송, 전시, 공연 및 방송할 수 있습니다.

다음과 같은 조건을 따라야 합니다:



저작자표시. 귀하는 원저작자를 표시하여야 합니다.



비영리. 귀하는 이 저작물을 영리 목적으로 이용할 수 없습니다.



변경금지. 귀하는 이 저작물을 개작, 변형 또는 가공할 수 없습니다.

- 귀하는, 이 저작물의 재이용이나 배포의 경우, 이 저작물에 적용된 이용허락조건을 명확하게 나타내어야 합니다.
- 저작권자로부터 별도의 허가를 받으면 이러한 조건들은 적용되지 않습니다.

저작권법에 따른 이용자의 권리는 위의 내용에 의하여 영향을 받지 않습니다.

이것은 [이용허락규약\(Legal Code\)](#)을 이해하기 쉽게 요약한 것입니다.

[Disclaimer](#)

Doctoral Thesis

Theoretical Study on Crystal Structure and  
Morphology Control of Semiconductor  
Nanomaterials via Multiscale Simulation

Ju Hyun Park

School of Energy and Chemical Engineering  
(Chemical Engineering)

Ulsan National Institute of Science and Technology

2021

Theoretical Study on Crystal Structure and  
Morphology Control of Semiconductor  
Nanomaterials via Multiscale Simulation

Ju Hyun Park

School of Energy and Chemical Engineering  
(Chemical Engineering)

Ulsan National Institute of Science and Technology

Theoretical Study on Crystal Structure and  
Morphology Control of Semiconductor  
Nanomaterials via Multiscale Simulation

A thesis/dissertation submitted to  
Ulsan National Institute of Science and Technology  
in partial fulfillment of the  
requirements for the degree of  
Doctor of Philosophy

Ju Hyun Park

12/15/2020 of submission

Approved by



Advisor

Sang Kyu Kwak

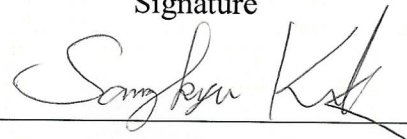
Theoretical Study on Crystal Structure and  
Morphology Control of Semiconductor  
Nanomaterials via Multiscale Simulation

Ju Hyun Park

This certifies that the thesis/dissertation of Ju Hyun Park is approved.

12/15/2020 of submission

Signature



Advisor: Sang Kyu Kwak

Signature



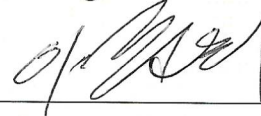
Seok Ju Kang: Thesis Committee Member #1

Signature



Jiseok Lee: Thesis Committee Member #2

Signature



Jun Hee Lee: Thesis Committee Member #3

Signature



Sang-Wook Kim: Thesis Committee Member #4

## Abstract

Crystalline solids are prevalent materials used in industrial applications and daily life. By controlling the crystal structure and morphology of the materials, the manufacturing process of high-value-added products can be improved. Crystal structure and morphology are influenced by both internal and external factors, where internal factors refer to the modification of the chemistry at a molecular level and external factors refer to the aspects beyond the crystal itself (i.e., temperature, pressure, concentration, solvent types, and ligand interaction). Depending on the specific molecular chemistry, the crystal structure and morphology of a material can be altered. Meanwhile, external factors can be manipulated to change the structure or morphology of a substance during crystallization. Moreover, they influence the thermodynamics (i.e., interaction between crystal surface and ligand) and kinetics (i.e., reaction rate) of reaction, resulting in different crystallization paths. During crystallization process composed of nucleation and crystal growth stages, numerous physicochemical properties of the materials are determined. Consequentially, thermodynamic, electronic, optical, and catalytic properties are dependent on the crystal structure and morphology.

In this dissertation, the crystal structure and morphology of semiconductor nanomaterials applied in electrochemical energy storage and optoelectronic fields were extensively studied. Various processes were used for the modification of these properties and in each case the principal mechanisms involved was investigated using multiscale simulation. In Chapter 1, a brief background on crystallization is given, including information on internal and external factors that influence the crystal structure and morphology during crystallization. We discuss how a variety of physicochemical phenomena can be investigated using a multiscale simulation approach that includes density functional theory (DFT) calculation, Monte Carlo (MC) simulation, molecular dynamics (MD) simulation, and morphology model. In Chapter 2, we designed the crystal structures of these nanomaterials (i.e., solid solution and co-crystal methods) by focusing on contorted hexabenzocoronene (cHBC), fluorinated cHBC, and fullerene ( $C_{60}$ ) molecules. Also, the detailed Li-ion storage mechanisms of each electrode materials were explored. Crystal structures vary depending on the molecules and the specific elemental composition, which results in materials exhibiting different electrochemical behaviors. These differences can be attributed to the difference in adsorption sites of Li-ions. In Chapter 3, using solvent engineering, the crystal structure and morphology were controlled by manipulating the crystallization process in perovskite materials. In dimethylformamide (DMF) solvent environment, DMF molecules have a relatively strong coordination with  $PbI_2$  due to the carbonyl group, resulting in  $PbI_2 \cdot DMF$  intermediate phase. Through slow nucleation and crystal growth in closed system, the intermediate phase of  $PbI_2 \cdot DMF$  crystal exhibited the one dimensional (1D) granular wire shape. From this granular wire morphology, many defects and grain boundaries appeared on the surface. Due to its surface

characteristics of granular wire morphology, the ultrahigh photo-detectivity can be obtained from the easy generation of deep trap states at surface and upward band bending at grain boundaries. In Chapter 4, the morphological changes of zinc-blended structures in ZnSe, the shell material of quantum dots, were ascribed to the interaction of Zn with the oleate ligand. Due to the strong adsorption of oleate on the (111) surface, a tetrahedron shape around the (111) surface was formed. As the reaction temperature increased by heating-up method, the stabilization effect of the oleate decreased, resulting in morphological changes in the form of a truncated tetrahedron. Depending on the morphology, different optical performance of QDs can be expected due to morphology-dependent quantum confinement effect. Overall, these studies demonstrated the design and control strategies of crystal structure and morphology of semiconductor materials. Crystal engineering, solvent engineering, and morphological engineering are expected to improve the electrical and optical performances of each semiconductor material.





## Contents

<b>Abstract.....</b>	<b>I</b>
<b>Contents .....</b>	<b>III</b>
<b>List of Tables.....</b>	<b>V</b>
<b>List of Figures.....</b>	<b>VI</b>
<b>Chapter 1. Introduction.....</b>	<b>1</b>
<b>1.1 Crystallization.....</b>	<b>1</b>
1.1.1 Nucleation .....	1
1.1.2 Crystal growth.....	3
<b>1.2 Introduction to Control of Crystal Structure and Morphology .....</b>	<b>4</b>
1.2.1 Chemical modification .....	4
1.2.2 Solvent engineering.....	7
1.2.3 Ligand interaction .....	10
<b>1.3 Simulation Methods.....</b>	<b>14</b>
1.3.1 Multiscale simulation .....	14
1.3.2 Morphology model.....	16
<b>1.4 References .....</b>	<b>18</b>
<b>Chapter 2. Crystal Engineering of Hexabenzocoronene Derivatives and C<sub>60</sub> with Ion Storage Mechanisms for Organic Anode Materials.....</b>	<b>21</b>
<b>2.1 Introduction.....</b>	<b>21</b>
<b>2.2 Computational details.....</b>	<b>24</b>
2.2.1 Crystal structure prediction .....	24
2.2.2 Monte Carlo simulation.....	24
2.2.3 Density functional theory calculation.....	25
2.2.4 HOMO and LUMO energy levels .....	25
<b>2.3 Results and Discussion.....</b>	<b>27</b>
2.3.1 Contorted hexabenzocoronene (cHBC).....	27
2.3.2 Fluorinated contorted hexabenzocoronene (F-cHBC).....	34
2.3.3 cHBC/F-cHBC solid solution.....	40
2.3.4 C <sub>60</sub> /cHBC cocrystal .....	46
<b>2.4 Conclusion .....</b>	<b>53</b>
<b>2.5 References .....</b>	<b>54</b>

<b>Chapter 3. Solvent Engineering of Perovskite Granular Wire with High Photodetectivity.....</b>	<b>57</b>
<b>3.1 Introduction.....</b>	<b>57</b>
<b>3.2 Computational details.....</b>	<b>59</b>
3.2.1 Growth morphology .....	59
3.2.2 Forcefield parameterization.....	59
3.2.3 Molecular dynamics simulation.....	62
3.2.4 Young's modulus calculation.....	62
<b>3.3 Results and Discussion.....</b>	<b>63</b>
<b>3.4 Conclusion .....</b>	<b>75</b>
<b>3.5 References .....</b>	<b>76</b>
<b>Chapter 4. Morphological Engineering of Quantum Dots through Oleate Ligand-ZnSe Shell Interaction with Temperature Control.....</b>	<b>78</b>
<b>4.1 Introduction.....</b>	<b>78</b>
<b>4.2 Computational details.....</b>	<b>80</b>
4.2.1 Density functional theory calculation.....	80
4.2.2 Gibbs free energy for temperature effect.....	80
<b>4.3 Results and Discussion.....</b>	<b>82</b>
<b>4.4 Conclusion .....</b>	<b>92</b>
<b>4.5 References .....</b>	<b>93</b>
<b>Chapter 5. Summary and Future Perspectives .....</b>	<b>95</b>
<b>List of Publications .....</b>	<b>98</b>
<b>Acknowledgements .....</b>	<b>100</b>

## List of Tables

- Table 3.1** Potential parameters for  $\text{PbI}_2 \cdot \text{DMF}$  crystal. C3 and C indicate the carbon atom of alkyl group and amide group, respectively, while H1 and H5 indicate hydrogen atom of alkyl group and amide group, respectively
- Table 3.2** Comparison of lattice parameters and Young's modulus obtained by DFT and fitted forcefield based calculations. Data are provided for the  $x(Y_x)$ ,  $y(Y_y)$ , and  $z(Y_z)$  directions of  $\text{PbI}_2 \cdot \text{DMF}$  crystal optimized by DFT and fitted forcefield calculations.
- Table 3.3** Lattice parameters for exposed surfaces. Lattice parameters are given for the (020), (011), (110),  $(10\bar{1})$ , and  $(11\bar{2})$  surfaces of  $\text{PbI}_2 \cdot \text{DMF}$  crystal.
- Table 3.4** Planar density of exposed surfaces and coordination number (CN) of outermost dangling atoms.
- Table 4.1** Interplanar distance according to the miller indices of the possible growth surfaces of zinc-blende ZnSe
- Table 4.2** Lattice parameters  $a$ ,  $b$ , and  $\varphi$  for the slab models and coverage ( $\theta$ ) of  $\text{Zn}(\text{oleate})_2$  to each surface for used in the calculation for the relaxed surface free energy.  $\theta$  was assumed to be equal to the number of dangling Se on each surface divided by twice of area. Since the ligand consists of two oleate ions, the coverage for ligand adsorption was taken to be a half of the number of dangling Se exposed on each surface.

## List of Figures

### Chapter 1

- Figure 1.1** Free energy diagram for homogeneous nucleus formation as a function of particle radius ( $r$ ).
- Figure 1.2** Schematic representation of mechanisms for (a) classical nucleation theory and (b) non-classical nucleation theory.
- Figure 1.3** LaMer diagram for crystallization.  $C_s$ ,  $C^*_{\min}$ , and  $C^*_{\max}$  are the solubility of crystal, minimum and maximum of supersaturation levels for nucleation, respectively. Reprinted with permission from ref 20. Copyright © 1952 American Chemical Society.
- Figure 1.4** Different crystal structures and properties depending on the crystallization method. The example of molecule unit is *p*-aminobenzoic acid (*p*ABA). Reprinted with permission from ref 23. Copyright © 2020 The Author(s).
- Figure 1.5** Schematic representation of modification of molecular unit chemistry and crystal engineering to form cocrystals and solid solutions.
- Figure 1.6** Schematic process of phase transition of (a) cHBC and (b) fluorinated cHBC. Reprinted with permission from ref 24 and 25, respectively. Copyright © 2014 American Chemical Society, and Copyright © 2017 American Chemical Society, respectively.
- Figure 1.7** Schematic illustration of different intermediate structures with morphologies depending on the polar solvents; DMF, GBL, NMP, and DMSO. Reprinted with permission from ref 40, 42, and 44, respectively. Copyright © 2016 WILEY-VCH Verlag GmbH & Co. KGaA, Weinheim, Copyright © 2017 Elsevier Ltd, and Copyright © 2016 American Chemical Society, respectively.
- Figure 1.8** (a) Different LaMer diagrams according to crystallization method, (b) nucleation and growth rate as a function of degree of supersaturation (left) and resulting cluster size (right). Reprinted with permission from ref 45. Copyright © 2017 Science China Press and Springer-Verlag GmbH Germany. (c) Schematic illustration of different intermediate structures with morphologies depending on the polar solvents; DMF, GBL, NMP, and DMSO. Reprinted with permission from ref 46. Copyright © The Royal Society of Chemistry 2017.

- Figure 1.9** (a) Different morphologies of Cu<sub>2</sub>O NCs depending on the ratio of growth rate along  $\langle 100 \rangle$  and  $\langle 111 \rangle$  directions. (b) Shape evolution of Cu<sub>2</sub>O NCs depending on ligand coverage. Reprinted with permission from ref 47. Copyright © The Royal Society of Chemistry 2009. (c) Schematic representation of modulation of catalytic properties with precise morphology control. Reprinted with permission from ref 48. Copyright © 2014 American Chemical Society.
- Figure 1.10** Surface energies and equilibrium shape of PbSe NCs as a function of surface coverage. Reprinted with permission from ref 49. Copyright © 2012 American Chemical Society.
- Figure 1.11** Classification of ligands according to covalent bonding to the surface of CdSe NCs. Reprinted with permission from ref 50. Copyright © 2016 Nature Publishing Group, a division of Macmillan Publishers Limited.
- Figure 1.12** Different shapes of CdSe NCs depending on the temperature. (a, b) sphere, (c, d) cubic, (e, f) tetrahedron, (g, h) branched shapes. Reprinted with permission from ref 51. Copyright © 2009 American Chemical Society.
- Figure 1.13** Multiscale computational approach according to time and length scales which covers density functional theory (DFT) calculation, Monte Carlo (MC) simulation and molecular dynamics (MD) simulation, and morphology model.
- Figure 1.14** Progress on morphology modelling and theory.

## Chapter 2

- Figure 2.1** (a) Face-on (left) and edge-on (right) molecular structure of cHBC. The crystal structure of cHBC exhibits two concave surfaces. (b) Schematic of proposed Li-ion intercalation mechanism in cHBC. (c) Galvanostatic discharge–charge voltage profile of a Li metal/separator/cHBC anode half-cell at a current density of  $0.1 \text{ A g}^{-1}$ . The inset figures show digital photographs of cHBC anode after  $\text{Li}^+$  de-intercalation and after Li-intercalation. (d) XRD pattern of as-synthesized cHBC. The inset figure represents schematic of cHBC slurry, which consists of cHBC and a poly(vinylidene fluoride) binder.
- Figure 2.2** (a) 1D diffraction traces for the sample series with as-prepared (black line), THF-annealed (red line), and THF-330 °C annealed (blue line) cHBC films. Significantly decreased peaks at both  $q_1 = 1.04$  and  $q_2 = 1.15 \text{ \AA}^{-1}$  indicate the phase transformation of cHBC from polymorph II to polymorph II'. (b) XRD patterns of cHBC: experimental (black line), Rietveld refined (red line), their difference (green line), and the  $R\bar{3}$  crystal phase (blue line). (c) Projection views of the  $R\bar{3}$  crystal phase along [001] and [100] directions, respectively. For clarity, the cHBC molecules in different layers are represented by yellow, light gray, and dark gray colors.
- Figure 2.3** (a) Galvanostatic discharge–charge profiles of THF-annealed (black dotted line) and THF–330 °C annealed (red dotted line) cHBC anodes at fixed current density of  $0.2 \text{ A g}^{-1}$ . (b) The differential capacity curve of the THF–330 °C annealed cHBC anode. (c)  $R\bar{3}$  crystal phase and (d) graphite projection views with Connolly surface. Carbon and hydrogen are colored yellow and white, respectively.
- Figure 2.4** The optimized structure of Li-intercalated cHBC and the electrostatic potential maps of cHBC without Li-ion. The electrostatic potential is mapped onto the Connolly surface (top) and (001) and (010) planes across the center of Li-ion (bottom left and right). Carbon, hydrogen, and lithium are colored yellow, white, and purple, respectively.
- Figure 2.5** (a) Projection views of the optimized stable structures of 3, 6, 9, and 18 Li-intercalated  $R\bar{3}$  crystal phase. Carbon, hydrogen, and lithium are colored yellow, white, and purple, respectively. (b) Formation energies of Li-intercalated cHBC as a function of the number of Li ions. The convex hull is shown as a red line. (c) The experimental (black line) and calculated (red line) voltage profiles.

- Figure 2.6** (a) Chemical structures and (b) energy diagrams of the molecular orbitals of contorted hexabenzocoronene (cHBC) and fluorinated cHBC (F-cHBC).
- Figure 2.7** (a) XRD patterns of F-cHBC: experimental (black line), Rietveld refined (red line), their difference (green line), and the  $P2_1/c$  crystal phase (blue line). ( $R_{wp}$  = 13.21 %,  $R_p$  = 9.74 %), (b) Projection views of the  $P2_1/c$  crystal structure along [100] and [010] directions, respectively. Carbon, hydrogen, and fluorine are grey, white, and red, respectively.
- Figure 2.8** (a) Galvanostatic discharge–charge profiles of F-cHBC anode. (b) Cyclic voltammograms of cell containing F-cHBC at scan rates from 0.1 to 1.0  $\text{mV s}^{-1}$ . The inset figure represents log–log plot of scan rate ( $\nu$ ) versus peak current ( $i_p$ ) and regression to estimate  $b$ . (c) Change in contributions of pseudocapacitive behavior. F-cHBC is located in the pseudocapacitive area. (d) CV curve at 1.0  $\text{mV s}^{-1}$ . Shaded region represented the capacitive contribution ( $k_1\nu$ ) to total charge storage.
- Figure 2.9** (a) Projection views of optimized  $P2_1/c$  crystal structure of Li-adsorbed F-cHBC along [100] (top) and [010] (bottom) directions. Grey: Carbon, red: fluorine, white: hydrogen yellow: lithium in site I, purple: lithium in site II. (b) Magnified view of Li-ion at site I (top) and site II (bottom). Black dotted arrow: distance between Li-ion and fluorine or between Li-ion and the centroid of the bent edge aromatic ring. Orange line: interaction of adsorbed Li-ion with negatively-charged atoms. (c) Formation energies of Li-adsorbed F-cHBC as a function of Li-ion content. Red line: convex hull. (d) Experimental (black line) and the calculated (red line) voltage profiles.
- Figure 2.10** (a) Galvanostatic discharge–charge profiles of (a) F-cHBC and (b) cHBC anodes contained in Li-ion cells. Corresponding differential capacity curves of (c) F-cHBC and (d) cHBC anodes.
- Figure 2.11** Schematic of solid solution formation using cHBC and F-cHBC molecules. Carbon and fluorine atoms are colored by yellow and red, respectively.
- Figure 2.12** (a) 1D diffraction traces of 2D GIWAXS results of cHBC, cHBC/F-cHBC blend ratios of 7:3, 5:5, 3:7, and F-cHBC electrode. (b) 1D diffraction traces of the pristine and fully lithiated cHBC/F-cHBC electrodes. (c) Postmortem X-ray diffraction patterns of solid solution electrodes (5:5 and 3:7) after fully lithiation. (d) 1D diffraction trace of 2D GIWAXS of lithiated cHBC/F-cHBC 5:5 electrode after 400 cycles in cell.

- Figure 2.13** (a) Comparison of the 1D diffraction trace of the lithiated cHBC/F-cHBC (5:5) electrode and the simulated XRD pattern of  $P2_1/n$  crystal phase of cHBC/F-cHBC solid solution. (b) Projection views of  $P2_1/n$  crystal phase of cHBC/F-cHBC solid solution along [010], [001], and [100] directions. cHBC and F-cHBC molecules are shown in gray and yellow, respectively. Note that fluorine is shown in red.
- Figure 2.14** (a) Galvanostatic charge-discharge profiles of cHBC, F-cHBC, and cHBC/F-cHBC blend solid solution electrodes with ratio of 3:7 and 5:5. (b) CV profiles at sweep speed of  $0.4 \text{ mV s}^{-1}$ . Shaded region represented the capacitive contribution ( $k_1v$ ) to total charge storage.
- Figure 2.15** Projection views of  $P2_1/n$  crystal phase of cHBC/F-cHBC solid solution with Li-ions along [010], [001], and [100] directions. cHBC molecules, F-cHBC molecules, Li-ions sandwiched between aromatic rings of cHBC and F-cHBC molecules, Li-ions between the aromatic rings of cHBC molecule and fluorine of F-cHBC molecule, and Li-ions on aromatic rings of cHBC and F-cHBC molecules are shown in gray, yellow, purple, magenta, and blue, respectively. Note that fluorine atoms are colored in red.
- Figure 2.16** Magnified views of adsorption site of Li-ions in optimized structure of  $P2_1/n$  crystal phase of cHBC/F-cHBC solid solution with Li-ions; (a) Li-ion sandwiched between aromatic rings of cHBC and F-cHBC molecules (site I, purple), (b) Li-ion between the aromatic ring of cHBC and fluorine of F-cHBC (site II, magenta), (c) Li-ion on aromatic ring of F-cHBC molecule (site III, blue). cHBC and F-cHBC molecules are shown in gray and yellow, respectively. Note that fluorine atoms are colored in red. The close contact of Li-ions are represented by orange dotted line.
- Figure 2.17** (a) Schematic of electron transfer mechanism in  $C_{60}/\text{cHBC}$  blend electrode, (b) XRD patterns of pristine cHBC, pristine  $C_{60}$ ,  $C_{60}/\text{cHBC} = 1:1$ ,  $2:1$ , and  $1:2$  electrodes.
- Figure 2.18** (a) Experimental *in situ* 1D-GIWAXS pattern of  $C_{60}/\text{cHBC}=1:1$  film annealed at  $330 \text{ }^\circ\text{C}$  (black line) and simulated XRD pattern of the orthorhombic Pnnm phase of  $C_{60}/\text{cHBC}$  cocrystal (blue line). (b) Projection views of the orthorhombic Pnnm phase of  $C_{60}/\text{cHBC}$  cocrystal along [001] and [010] directions. White dashed line represents the lattice of the unit cell.
- Figure 2.19** Magnified projection views of the orthorhombic Pnnm phase of  $C_{60}/\text{cHBC}$  cocrystal along [001], [100] and [010] directions. Central single  $C_{60}$  molecule (space-filling model) and its surrounding molecules (ball and stick model) are only visualized for clarity.  $C_{60}$  molecules and cHBC molecules are gray and yellow, respectively.



- Figure 2.20** Front, top, and side views of a single sheet of (001) and (100) planes of orthorhombic Pnnm phase of  $C_{60}$ /cHBC cocrystal.  $C_{60}$  and cHBC molecules are colored by gray and yellow, respectively.
- Figure 2.21** (a) Galvanostatic charge-discharge profiles and (b) corresponding reversible capacity values of pristine  $C_{60}$ , pristine cHBC,  $C_{60}$ /cHBC = 1:2, 2:1, and 1:1.
- Figure 2.22** Projection views of Pnnm phase of  $C_{60}$ /cHBC cocrystal with Connolly surface (light gray) along [001], [100] and [010] directions. The space enclosed by the Connolly surface represents the vacant space.  $C_{60}$  molecules and cHBC molecules are gray and yellow, respectively.
- Figure 2.23** Experimental (black line) and the calculated (red line) voltage profiles. Inset figures represent projection views of the optimized Pnnm phase of Li-ion inserted  $C_{60}$ /cHBC cocrystal along [001] direction.
- Figure 2.24** Projection views of Pnnm phase of Li-ion inserted  $C_{60}$ /cHBC cocrystal along [100] and [010] directions; a) stage I, b) stage II, c) stage III.  $C_{60}$  molecules, cHBC molecules, inserted Li-ion at stage I, additionally inserted Li-ion at stage II, and additionally inserted Li-ion at stage III are gray, yellow, green, cyan, and blue, respectively.
- Figure 2.25** The optimized structure of Pnnm phase of Li-ion inserted  $C_{60}$ /cHBC cocrystal at each stage and magnified views of Li-ion insertion site; a) stage I, b) stage II, c) stage III.  $C_{60}$  molecules, cHBC molecules, inserted Li-ion at stage I, additionally inserted Li-ion at stage II, and additionally inserted Li-ion at stage III are gray, yellow, green, cyan, and blue, respectively. The distances between Li-ion and centroid of hexagonal or pentagonal aromatic ring of  $C_{60}$  or cHBC molecules and close contact of Li-ion are black dotted arrow and orange line, respectively. The total charges of carbon of aromatic rings are represented by blue color.

## Chapter 3

- Figure 3.1** XRD data from experiment, DFT and MD simulations. XRD data are shown for  $\text{PbI}_2 \cdot \text{DMF}$  crystal: experimental (black), DFT calculations (red), and fitted forcefield based optimization (blue).
- Figure 3.2** Schematic images of the (a) synthesis process for PGWs and (b) crystal structure corresponding to each experiment process.
- Figure 3.3** (a) XRD patterns of PDGWs,  $\text{PbI}_2$  GWs, and PGWs, (b) crystal structure of  $\text{PbI}_2 \cdot \text{DMF}$ . Pb, I, C, N, O and H atom are dark grey, brown, grey, blue, red and white color, respectively.
- Figure 3.4** (a) Schematic images of the precipitation process of  $\text{PbI}_2$  solution based on DMF and GBL solvent in the open system. Optical microscopy images of extracted (b)  $\text{PbI}_2 \cdot \text{DMF}$  from DMF solvent-based solution and (c)  $\text{PbI}_2$  from GBL solvent-based solution in the open system (inset: XRD patterns of  $\text{PbI}_2$  from GBL solvent-based solution). (d) Schematic images of the precipitation process of  $\text{PbI}_2$  solution based on DMF and GBL solvent in the closed system. Optical microscopy images of extracted (e)  $\text{PbI}_2 \cdot \text{DMF}$  from DMF solvent-based solution and (f)  $\text{PbI}_2$  from GBL solvent-based solution in the open system (inset: SEM image of randomly aggregated  $\text{PbI}_2$  particles extracted in GBL).
- Figure 3.5** Transmission electron microscopy (TEM) images of (a) PDGW and (b) PGW.
- Figure 3.6** (a) Growth morphology of  $\text{PbI}_2 \cdot \text{DMF}$ , (b) SEM images of  $\text{PbI}_2 \cdot \text{DMF}$  seed crystals (scale bar: 100 nm). Pb, I, C, N, O and H atom are dark grey, brown, grey, blue, red and white color, respectively.
- Figure 3.7** Attachment energies and interplanar distances of the exposed surfaces.
- Figure 3.8** The optimized bulk structure and the cleaved (020), (011), (110),  $(10\bar{1})$ , and  $(11\bar{2})$  surfaces of  $\text{PbI}_2 \cdot \text{DMF}$  crystal are shown. Pb, I, C, N, O, and H atoms are represented by dark gray, brown, gray, blue, red, and white, respectively.
- Figure 3.9** Initial configurations of the interface model system. (a) A schematic shows model system interfaces composed of (b) identical surfaces, i.e., A-A interface, and (c) different surfaces, i.e., A-B interface. Pb, I, C, N, O, and H atoms are represented by dark gray, brown, gray, blue, red, and white, respectively.

- Figure 3.10** Final configurations of the interface model system. (a) Final configurations are shown for the (020), (011), (110),  $(10\bar{1})$ , and  $(11\bar{2})$  surfaces after 1 ns MD simulations. Final configurations are shown for (b) A-A interfaces, and (c) A-B interfaces after 1 ns MD simulations. Pb, I, C, N, O, and H atoms are represented by dark gray, brown, gray, blue, red, and white, respectively.
- Figure 3.11** Binding energies between the exposed surfaces.
- Figure 3.12** Atomic configurations of bulk and each surface are shown with the atom type and coordination number. The subscript denotes the coordination number (Table 3.4). Pb, I, C, N, O, and H atom are shown in dark gray, brown, gray, blue, red, and white, respectively. Purple dotted lines represent close contact.
- Figure 3.13** Granular wire growth scheme and its interfacial structures between identical (110) surfaces and between (110) and  $(10\bar{1})$  surface. Bulk Pb and I atoms and DMF molecules are shown in dark gray, brown, and green, respectively. 5- and 4-coordinated Pb atoms are shown in red and purple while 2- and 1- coordinated I atoms are shown in orange and cyan, respectively.
- Figure 3.14** Schematic of band bending of PGWs due to trap states on the surface in the radial direction.

## Chapter 4

- Figure 4.1** Absorption and PL data of InGaP/ZnSe by ZnSe shell coating temperature at (a) 270 °C, (b) 300 °C and (c) 320 °C.
- Figure 4.2** TEM image of InGaP/ZnSe; (a,d) shell coated at 270 °C, (b,e) shell coated at 300 °C, and (c,f) shell coated at 320 °C.
- Figure 4.3** PXRD patterns of InGaP/ZnSe by ZnSe shell coating temperature at 270 °C, 300 °C, and 320 °C.
- Figure 4.4** (a) PL & absorption data of InGaP/ZnSe/ZnS, (b) PXRD pattern of InGaP/ZnSe/ZnS.
- Figure 4.5** Optimized slab models of (a) ZnSe (111) surface, (b) (11 $\bar{1}$ ) surface, (c) (200) surface, and (d) (220) surface. The numbers below each figure represent the surface energy (in kcal/mol/Å<sup>2</sup>). The bottom blue regions were fixed to theoretically mimic the bulk phase. Zn and Se are represented by navy and orange colored spheres, respectively.
- Figure 4.6** Optimized ligand models of (a) oleate, (b) Zn(oleate)<sub>2</sub>. The acetate ion was used to represent the oleate ion, which have the same carboxylate group. Zn, O, C, and H are represented by navy, red, grey and white colored spheres, respectively.
- Figure 4.7** Optimized structures of each ZnSe surface with Zn(oleate)<sub>2</sub> model; (a) ZnSe (111) surface, (b) (11 $\bar{1}$ ) surface, (c) (200) surface, and (d) (220) surface. The bottom blue regions were fixed to theoretically mimic the bulk phase. Zn, Se, O, C, and H are represented by navy, orange, red, grey and white colored spheres, respectively.
- Figure 4.8** (a) Gibbs free energy for adsorption of oleate ( $\Delta G_{ad}$ ) —  $\Delta G_{ad}$  is calculated from Eqs. (1) and (3). (b) Gibbs free energy of binding of Zn(oleate)<sub>2</sub> ( $\Delta G_{bind}$ ) to each ZnSe surface depending on temperature, —  $\Delta G_{bind}$  is calculated from Eqs. (1) and (2).
- Figure 4.9** (a) Relaxed surface free energy ( $\gamma_r$ ) as a function of the temperature —  $\gamma_r$  is calculated from Eq.(8). (b) Surface free energy as a function of the temperature —  $\gamma$  is calculated from Eq.(7). (c) Gibbs free energy for structural change of adsorbed Zn(oleate)<sub>2</sub> ( $\Delta G_{struc}$ ) as a function of the temperature —  $\Delta G_{struc}$  is calculated from Eqs. (1) and (5), (d) Gibbs free energy for reconstruction of surface ( $\Delta G_{rec}$ ) as a function of the temperature —  $\Delta G_{rec}$  is calculated from Eqs. (1) and (4).
- Figure 4.10** Equilibrium morphology based on  $\gamma_r$  with respect to temperature — red and black represent the (111) and (220) surfaces, respectively.
- Figure 4.11** (a) Predicted morphology at 327 °C, and (b) HR-TEM image of InGaP/ZnSe at 320 °C.

## Chapter 1. Introduction

### 1.1 Crystallization

Crystallization is an important process to elucidate, as the crystal structure and morphology influences each performance that have applications in the electronic [1,2], energy storage [3-5], pharmaceutical [6,7], and catalysis industry [8]. Crystallization is controlled to achieve specific functionality and targeted physical and chemical properties, as these properties of crystal materials are affected by the crystal polymorph, shape, size, chemical impurity, etc [9]. During crystallization, many variables can be controlled. Thus, to design and control the molecular solid-state structure (i.e., crystal engineering), an in-depth understanding of the overall crystallization mechanism namely nucleation and crystal growth is necessary.

#### 1.1.1 Nucleation [10-12]

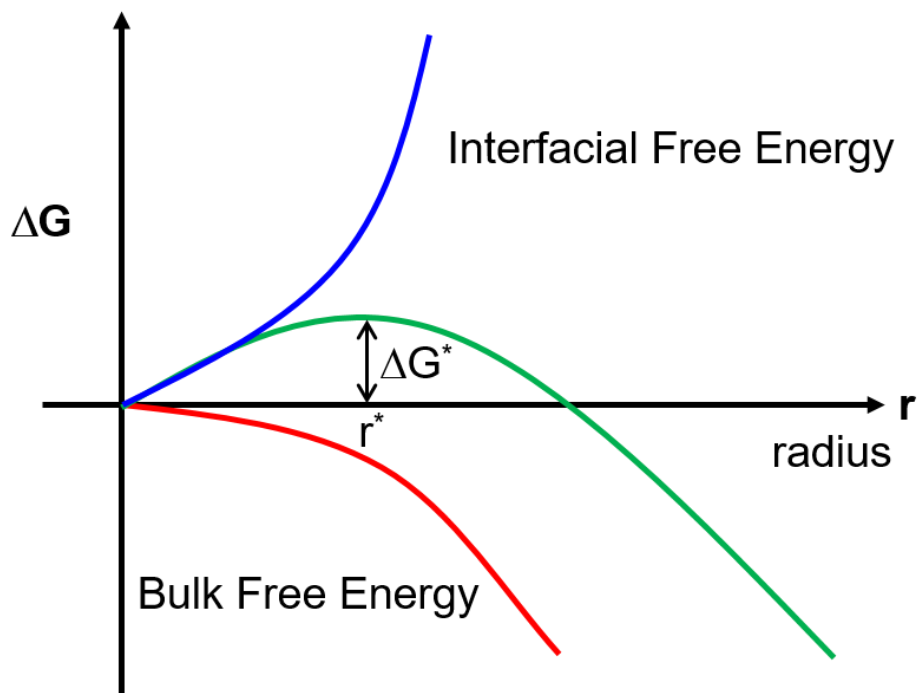


**Figure 1.1** Free energy diagram for homogeneous nucleus formation as a function of particle radius ( $r$ ).

During the first stage of crystallization, an atom/molecule aggregates to form a nucleus and the first new phase appears as part of the crystallization process. The mechanism of nucleation, based on the classical nucleation theory (CNT) [13], which is derived from fundamental thermodynamic principles, describes the nucleation pathways. Under supersaturation conditions, a nucleus in the shape of a spherical particle can form and is described thermodynamically by calculating the sum of the interfacial free energy and bulk free energy (**Figure 1.1**).

During homogeneous nucleation, the total free energy ( $\Delta G$ ) of a spherical particle of nucleus with a radius of  $r$  defined as follows,

$$\Delta G = \Delta G_b + \Delta G_i = -\frac{4\pi r^3}{3}\Delta G_c + 4\pi r^2\gamma$$

where  $\Delta G_b$ ,  $\Delta G_i$  and  $\Delta G_c$  are the total bulk free energy, interfacial free energy, and free energy of bulk crystal, respectively, and  $\gamma$  is the interfacial energy. The free energy of a nucleus particle consisting of the sum of the bulk free energy which is always negative and is proportional to  $r^3$ , and interfacial free energy (i.e., surface free energy) which is always positive and is proportional to  $r^2$ . It is possible to obtain a critical radius ( $r^*$ ) which has the maximum free energy of the nucleus. During nucleation,  $r^*$  is of thermodynamic significance because when  $r < r^*$ , the new nucleus will dissolve back into solution, but when  $r > r^*$ , the new nucleus will become thermodynamically stable ( $\Delta G < 0$ ) and result in continuing crystal growth.

In addition to CNT, there are several reports that have gained interest in the past decade, where non-classical nucleation theory using a two-step nucleation mechanism is described (**Figure 1.2**) [13-16]. Based on non-classical nucleation theory, specifically for colloidal crystal, protein, and mineral crystallization, it has been demonstrated that there are pre-nucleation steps where stable pre-nucleation clusters can form. Compared to optimal bulk free energy, the relatively low interfacial free energy can induce low activation barriers in crystallization path, resulting in the favorable formation of pre-nucleation cluster [17]. In the early stage of the nucleation, additive effects such as the interaction between solvent and precursor can affect the crystallization path.

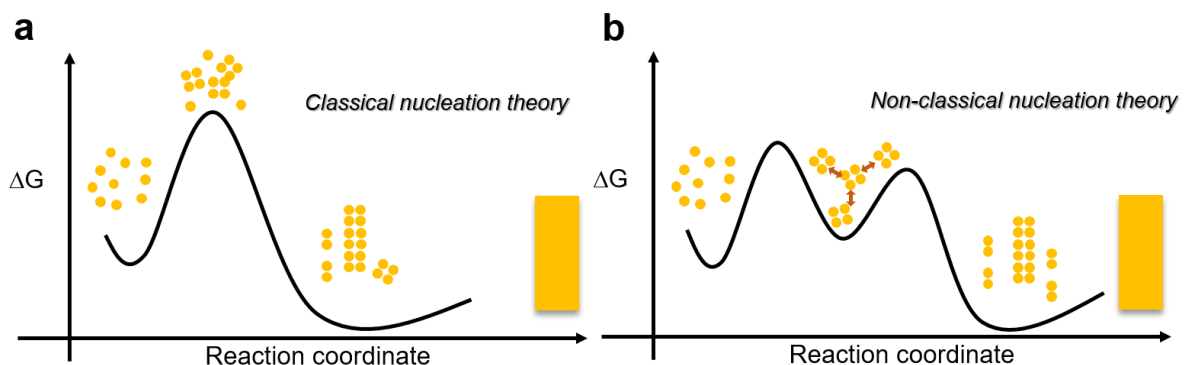


**Figure 1.2** Schematic representation of mechanisms for (a) classical nucleation theory and (b) non-classical nucleation theory.

### 1.1.2. Crystal growth [18-20]

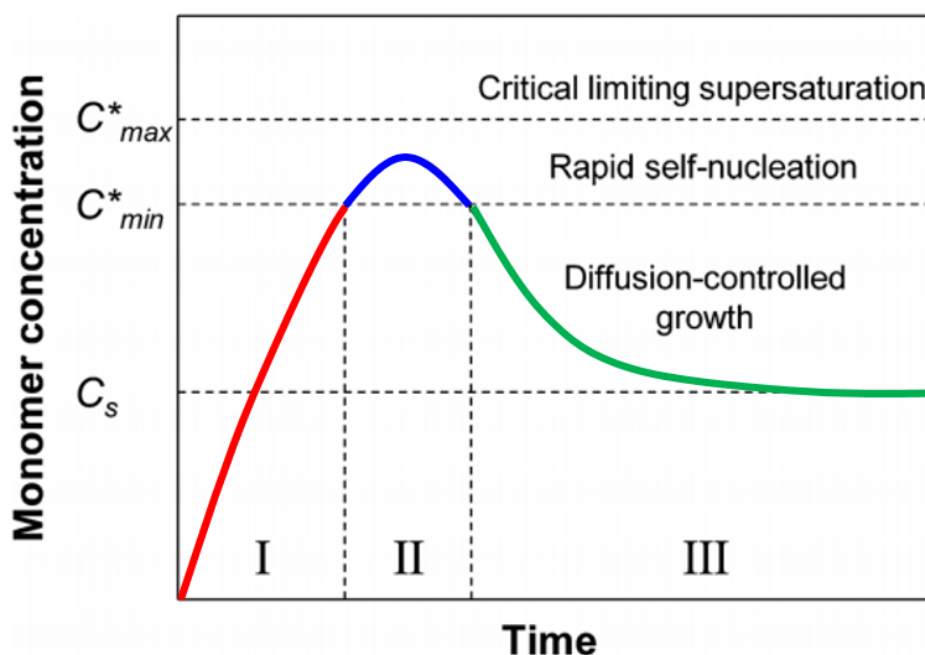


**Figure 1.3** LaMer diagram for crystallization.  $C_s$ ,  $C_{min}^*$ , and  $C_{max}^*$  are the solubility of crystal, minimum and maximum of supersaturation levels for nucleation, respectively. Reprinted with permission from ref 20. Copyright © 1952 American Chemical Society.

The LaMer model was developed which describes the nucleation and growth stages. As shown in **Figure 1.3**, the crystallization process is described by three stages: pre-nucleation (I), nucleation (II), and crystal growth (III) [21]. As the concentration increases until  $C_s$  (solubility level of the bulk solid), the remarkable reaction cannot occur like formation of nucleation (stage I). The monomer concentration reaches a critical level ( $C_{min}^*$ ), resulting in the formation of nucleation. Then, the concentration of monomer decreases as it becomes part of the forming nuclei (stage II). At stage III, the crystal will grow until the equilibrium is reached. Crystal growth occurs within a competitive system where increasing interfacial free energy favors dissolution, and decreasing bulk free energy favors growth, as described in the equation in the previous paragraph. As can be seen from the description of these crystallization mechanisms, various factors such as temperature, solvent, capping agent, interparticle interaction, lattice mismatch, etc. can play a role in controlling the crystal structure and morphology during nucleation and crystal growth.

## 1.2 Introduction to Control of Crystal Structure and Morphology

### 1.2.1 Chemical modification

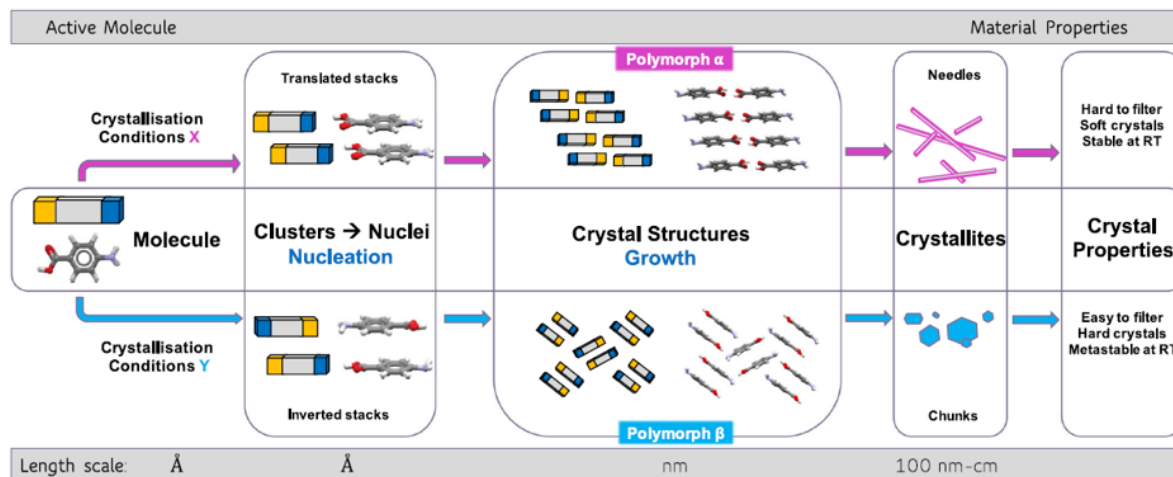


**Figure 1.4** Different crystal structures and properties depending on the crystallization method. The example of molecule unit is *p*-aminobenzoic acid (*p*ABA). Reprinted with permission from ref 23. Copyright © 2020 The Author(s).

The crystal structures of polymorphs, specifically for an organic material, is dependent on the molecular composition, temperature, pressure, etc. The molecule packing determines its properties such as boiling/melting points, mechanical hardness, solubility, charge carrier mobility, etc (**Figure 1.4**). Using the crystal structure prediction (CSP) method [22], many variables such as lattice parameters, symmetry, molecular conformations, and packing arrangement need to be known to determine crystal structure. Even if the molecular formulae for two substances are the same, the molecular arrangement of each may vary depending on crystallization conditions, which results in different crystal structures and morphologies [23]. In a second case, if the molecular units are different (**Figure 1.5**), the expected crystal structures and morphologies are even more complex. As an example of chemical modification, by using non-linear polyaromatic hydrocarbons (PAHs), Hiszpanski et al. [24] observed that three different polymorphs of contorted hexabenzocoronene (cHBC) depending on different synthesis methods (**Figure 1.6a**). Chemical modification is easily applied in cHBC organic materials. The substitution of hydrogen atoms with fluorine atoms is widely performed to improve the electronic properties of materials. The referenced authors also continuously demonstrated a series of four fluorinated cHBC (FcHBC) derivatives depending on the amount of fluorine [25]. A solvent vapor annealing process was applied to induce a phase transition to polymorph II, and thermal annealing of polymorph II produced polymorph II', which is a preferred orientation in cHBC. However, in the case of FcHBC, the polymorph II can only be accessed in an amorphous form (**Figure 1.6b**). Through



fluorination, a modification of the molecular chemistry, different phase transition mechanisms between polymorphs can be observed, and the properties of the crystals are also expected to be different. Although the authors did not clarify the detailed structures of polymorphs II and II', the highest hole mobilities of each phase were given: given: for polymorph I it was  $2 \times 10^{-3} \text{ cm}^2 \text{ V}^{-1} \text{ S}^{-1}$ , for polymorph II it was  $3.3 \times 10^{-4} \text{ cm}^2 \text{ V}^{-1} \text{ S}^{-1}$ , and for polymorph II' it was  $3.6 \times 10^{-3} \text{ cm}^2 \text{ V}^{-1} \text{ S}^{-1}$ . These differing values are due to different packing arrangements of  $\pi$  orbitals. The charge transport in small molecules in the crystalline phase of semiconductors is highly sensitive to changes in the polymorph structure because of the intermolecular  $\pi$  orbital overlap. In addition, the halogenated cHBC molecular semiconductors can modulate the electronic properties of the molecule e.g., lower the molecular orbital energy levels [26]. It can provide new insights into engineering new polymorphs and characterizing the performance improvements of these polymorphs for application in organic semiconductors.

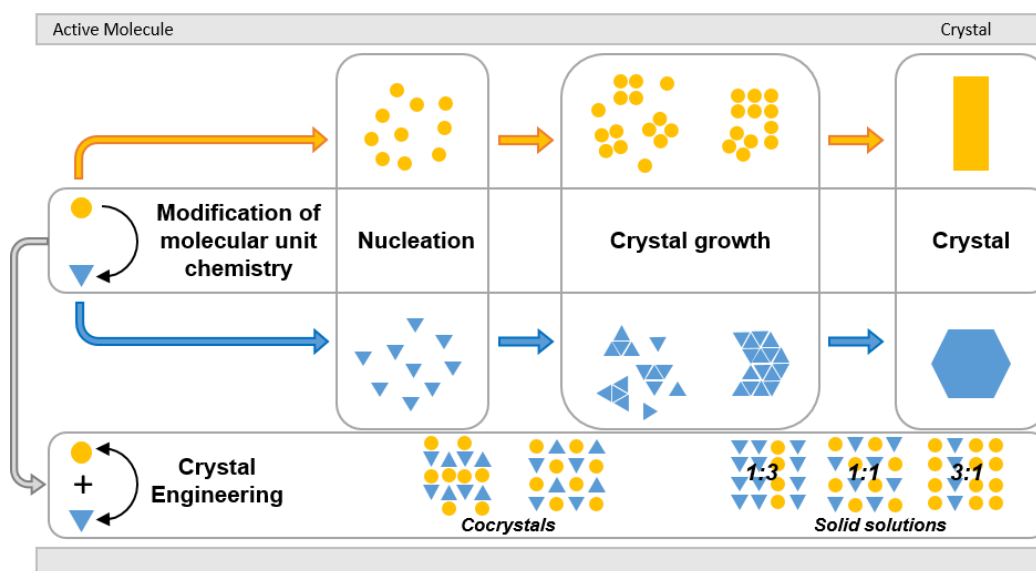


**Figure 1.5** Schematic representation of modification of molecular unit chemistry and crystal engineering to form cocrystals and solid solutions.

Therefore, to design an organic semiconductor material with enhanced electrochemical performance, it is necessary to control the crystal structure through chemical modification on a molecular level. Since the charge transport and electronic properties of organic semiconductor materials differ, as a result of varying molecular chemistry and molecular packing, theoretical research on the crystal structure is important for the strategic design and effective application of organic semiconductor materials. We will examine the theoretical studies of organic electrode materials related to the determination of crystal structure based on the molecular unit and the corresponding ion storage mechanism in Chapter 2.

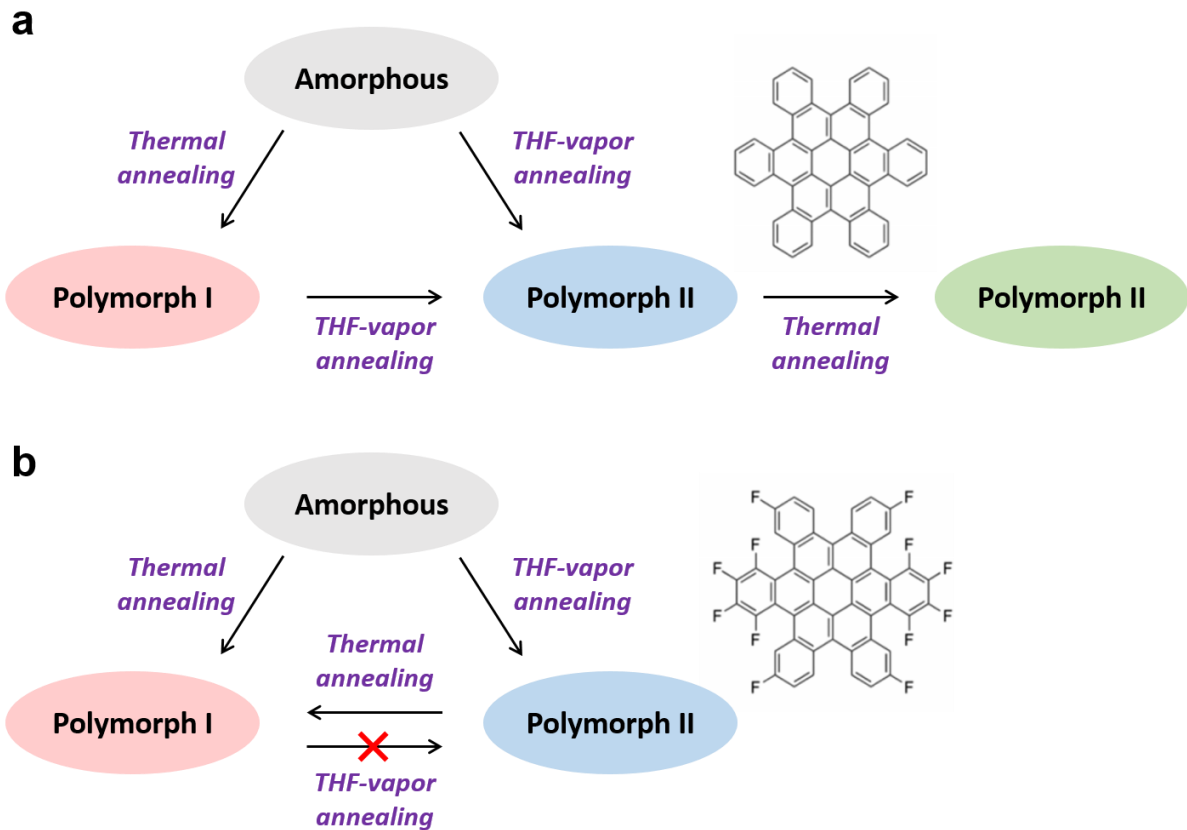


**Figure 1.6** Schematic process of phase transition of (a) cHBC and (b) fluorinated cHBC. Reprinted with permission from ref 24 and 25, respectively. Copyright © 2014 American Chemical Society, and Copyright © 2017 American Chemical Society, respectively.

### 1.2.2 Solvent engineering

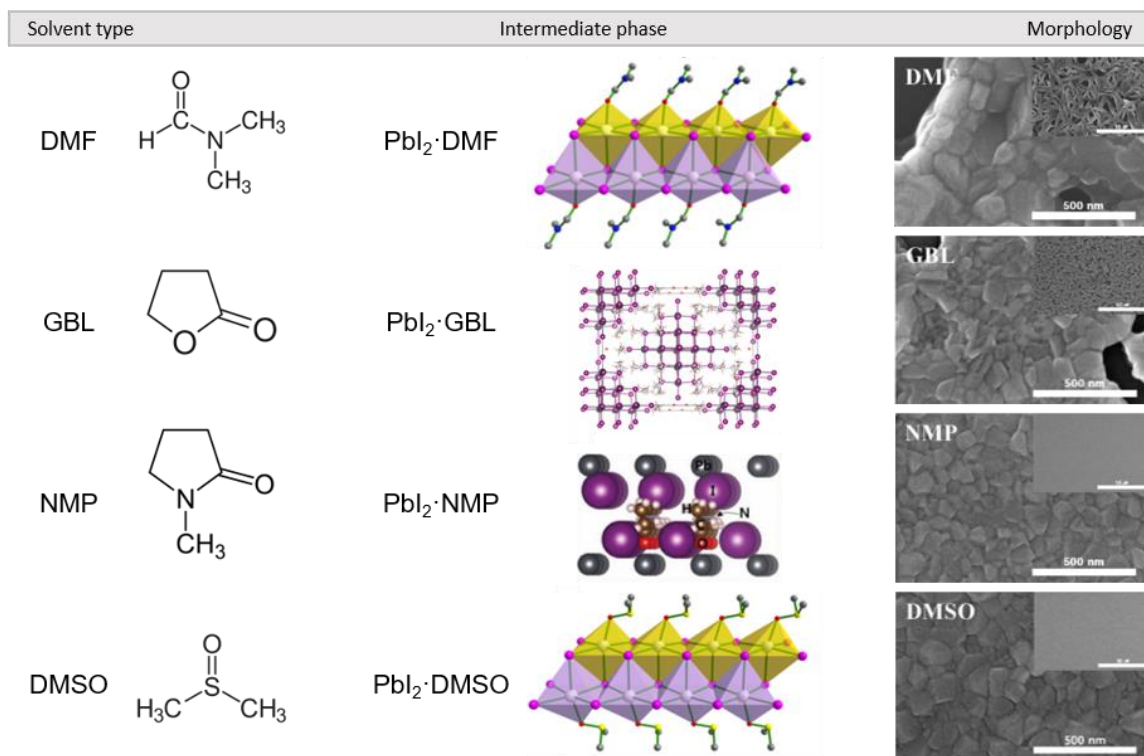


**Figure 1.7** Schematic illustration of different intermediate structures with morphologies depending on the polar solvents; DMF, GBL, NMP, and DMSO. Reprinted with permission from ref 40, 42, and 44, respectively. Copyright © 2016 WILEY-VCH Verlag GmbH & Co. KGaA, Weinheim, Copyright © 2017 Elsevier Ltd, and © 2016 American Chemical Society, respectively.

By controlling the crystallization path in solution, engineered materials have potential to be used in various industrial fields; particularly in this study the focus is on perovskite-based optoelectronic applications. The interaction between precursor of perovskite and solvent is important to determine an intermediate phase (**Figure 1.7**). Polar solvents that are widely used in perovskite precursor solutions include dimethylformamide (DMF) [27-33],  $\gamma$ -butyrolactone (GBL) [34-38], dimethyl sulfoxide (DMSO) [39], N-methyl-2-pyrrolidone (NMP) [40,41], etc. Solvent engineering refers to assembly processes such as solvent-modification and solvent-removal. Especially, the solvent engineering is effectively applied to finetuning the morphology of perovskite materials in solar cell device [42]. The most common solvent engineering procedure used for perovskite is where first of all,  $PbI_2$  and methyl ammonium iodide (MAI) are dissolved in a polar solvent, following which the layered structure is transformed into an intermediate phase, and then the relatively weak binding solvent molecules are removed by annealing to finally produce a 3D perovskite structure [43]. The structures and morphologies of the intermediate phases were significantly influenced by the type of solvent used.

Among the polar solvents, DMF, NMP and DMSO can bind strongly to Pb ions, while GBL can form the clusters in the solution as GBL exhibits weak interactions with Pb ions. Many studies have demonstrated that DMF, NMP, and DMSO can form an intermediate phase for effectively controlling the morphology of perovskite. However, there are some reports that indicate that DMF solvents produce inconsistencies in perovskite morphology which is attributed to uncontrolled nucleation and crystal growth of the  $\text{PbI}_2 \cdot \text{DMF}$  intermediate phase. Therefore, we developed forcefield parameters that describe  $\text{PbI}_2 \cdot \text{DMF}$  intermediate crystal structure, and studied the thermodynamically stable nuclei form of  $\text{PbI}_2 \cdot \text{DMF}$  crystal. DMF solvent forms one dimensional (1D)  $\text{PbI}_2 \cdot \text{DMF}$  intermediate phase due to coordination between Pb of  $\text{PbI}_2$  and O of DMF molecule [44].

In the case of the perovskite film, the morphology of the film can be controlled according to the supersaturation level and duration period based on the solution/substrate heterointerface during the crystallization (**Figure 1.8**) [45]. During the evaporation of the solvent under isothermal condition, the solute concentration is increased to form nuclei. When the evaporation of the solvent is accelerated, the time to reach the supersaturation concentration becomes shorter, resulting in a relatively longer nucleation period, and a relatively shorter crystal growth period. Therefore, the overall crystal size is small (red line) due to the formation of many nuclei. On the other hand, after the nuclei are formed, the nuclei will grow rapidly (purple line) under the condition where the evaporation of the solvent is reduced. It is come from the competitive relationship between nucleation and crystal growth as it consumes solute. Therefore, under slow solvent evaporation condition, a large crystalline domain can be obtained instead of monocrystalline domains. The competition between the kinetics of nucleation and crystal growth can be represented as a function of the degree of supersaturation, resulting in the size of crystalline region. Therefore, to effectively control the morphology of perovskite materials, we investigated how the kinetics and thermodynamics of each crystallization method influence the morphology, using DMF, which is a strong coordination solvent, and GBL, a relatively weak coordination solvent. We also studied the  $\text{PbI}_2 \cdot \text{DMF}$  intermediate crystal structure, nucleation formation and crystal growth using the theoretical approach in Chapter 3.

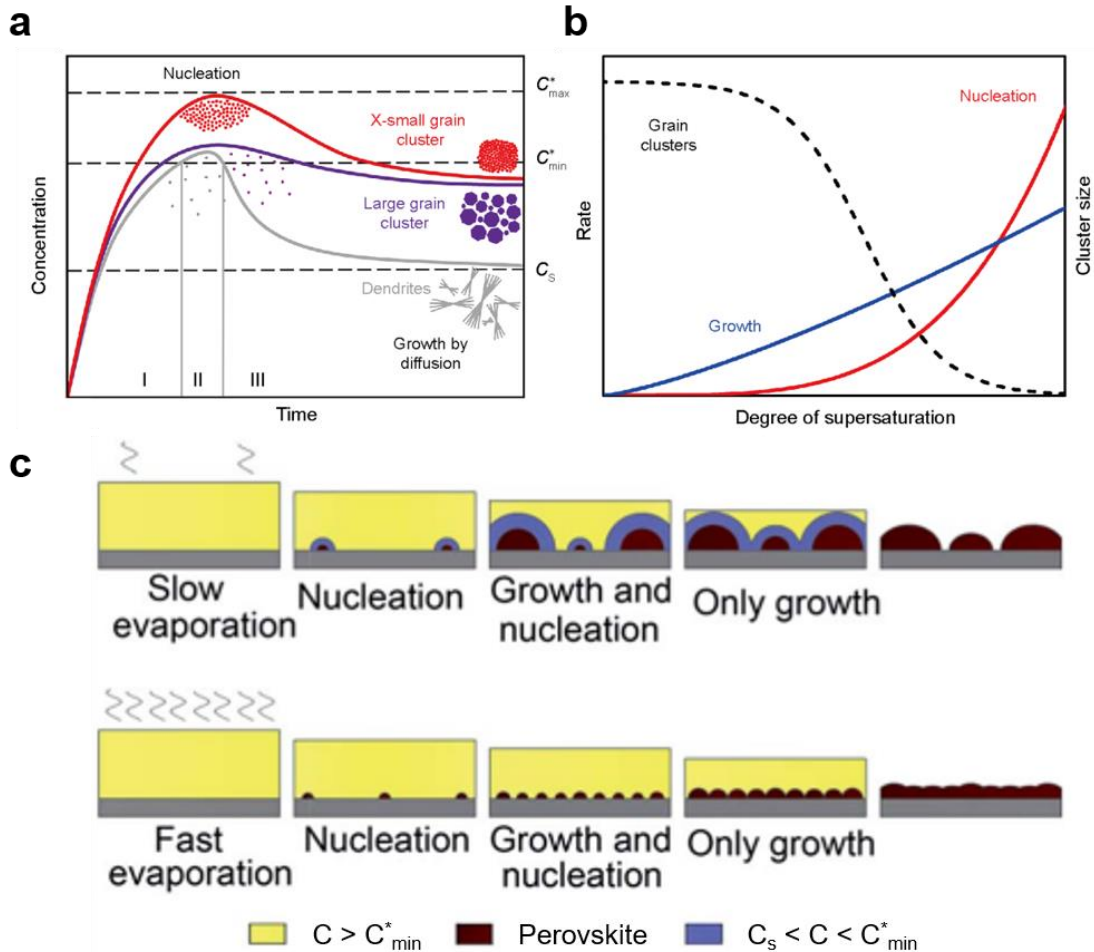


**Figure 1.8** (a) Different LaMer diagrams according to crystallization method, (b) nucleation and growth rate as a function of degree of supersaturation (left) and resulting cluster size (right). Reprinted with permission from ref 45. Copyright © 2017 Science China Press and Springer-Verlag GmbH Germany. (c) Schematic illustration of different intermediate structures with morphologies depending on the polar solvents; DMF, GBL, NMP, and DMSO. Reprinted with permission from ref 46. Copyright © The Royal Society of Chemistry 2017.

### 1.2.3 Ligand interaction

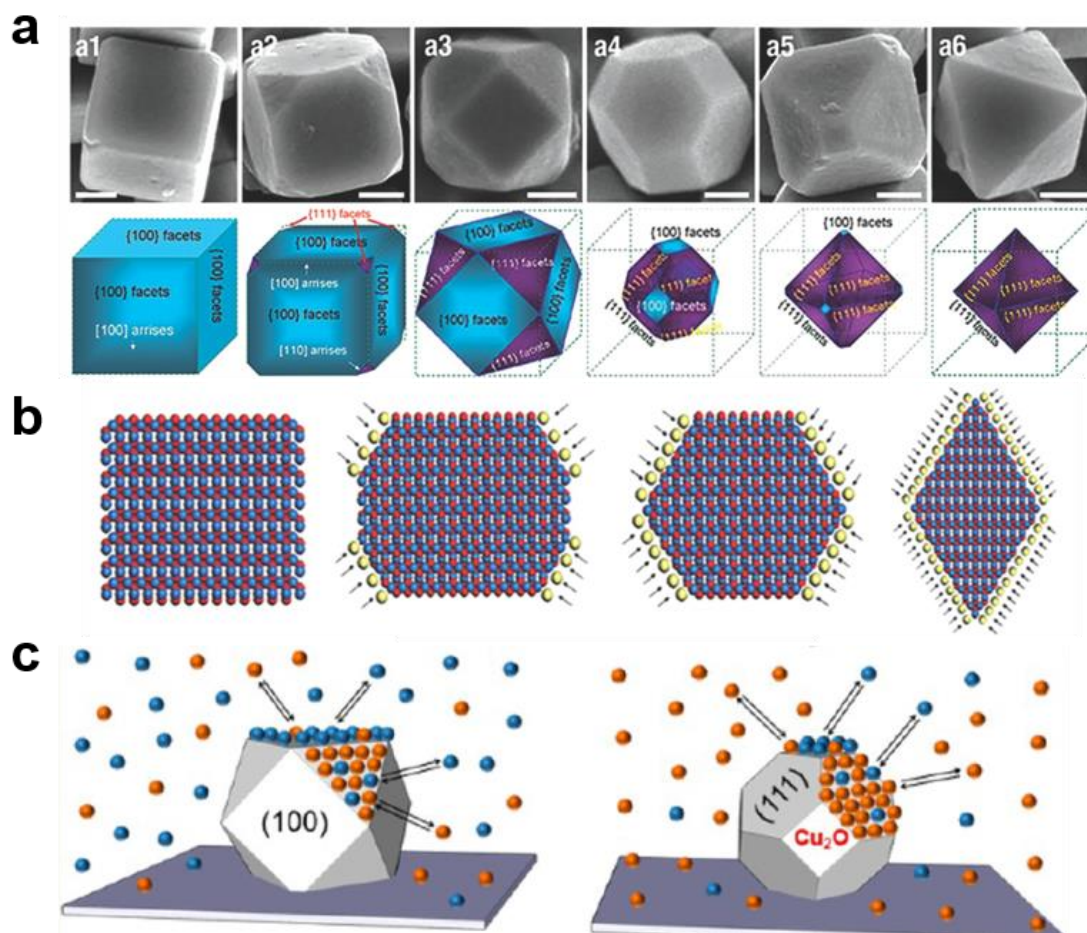


**Figure 1.9** (a) Different morphologies of  $\text{Cu}_2\text{O}$  NCs depending on the ratio of growth rate along  $\langle 100 \rangle$  and  $\langle 111 \rangle$  directions. (b) Shape evolution of  $\text{Cu}_2\text{O}$  NCs depending on ligand coverage. Reprinted with permission from ref 47. Copyright © The Royal Society of Chemistry 2009. (c) Schematic representation of modulation of catalytic properties with precise morphology control. Reprinted with permission from ref 48. Copyright © 2014 American Chemical Society.

In nanocrystals, the ligand and surface energy play a critical role in determining the morphology. The ligand can provide stability to surface, allowing it to be exposed to morphology surface because its growth rate is lower than that of other surfaces (**Figure 1.9**) [47,48]. The growth rate of each surface can be controlled according to the coverage of the ligand of exposed surface, and the morphology can be changed accordingly as shown in **Figure 1.10** [49]. In general, nanocrystals are capped with organic ligands such as oleylamine or oleic acid. The organic ligands are classified into three categories according to the electron donor-acceptor properties: X-type, L-type, and Z-type (**Figure 1.11**) [50]. X-type ligands have an odd number of electrons which are one-electron donors, and coordinate with metal atom which can accept one electron. Thus, it is generally used in termination of nanocrystals. Examples

of X-type ligands are the carboxylates, thiolates, and phosphonates, etc. L-type ligands have a lone pair of electrons which are neutral, two-electron donor, and coordinate with a metal atom on the surface. Examples of L-type ligands are the amines, phosphines, and phosphine oxides. Z-type ligands are neutral electron acceptor compared to X- and L-type ligands. The ligands are composed of metal atom that can accept two electrons, and coordinate with electron-rich sites such as oxide and chalcogenides.

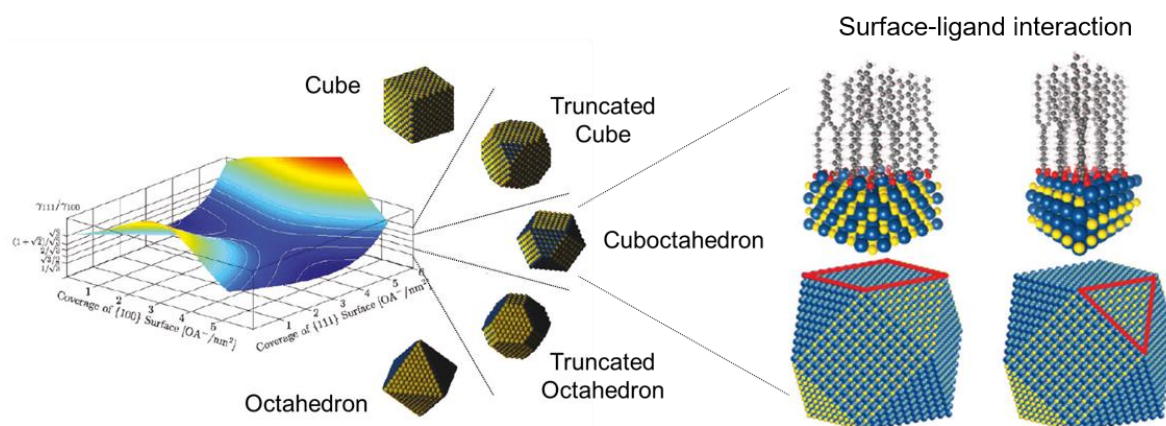


**Figure 1.10** Surface energies and equilibrium shape of PbSe NCs as a function of surface coverage. Reprinted with permission from ref 49. Copyright © 2012 American Chemical Society.

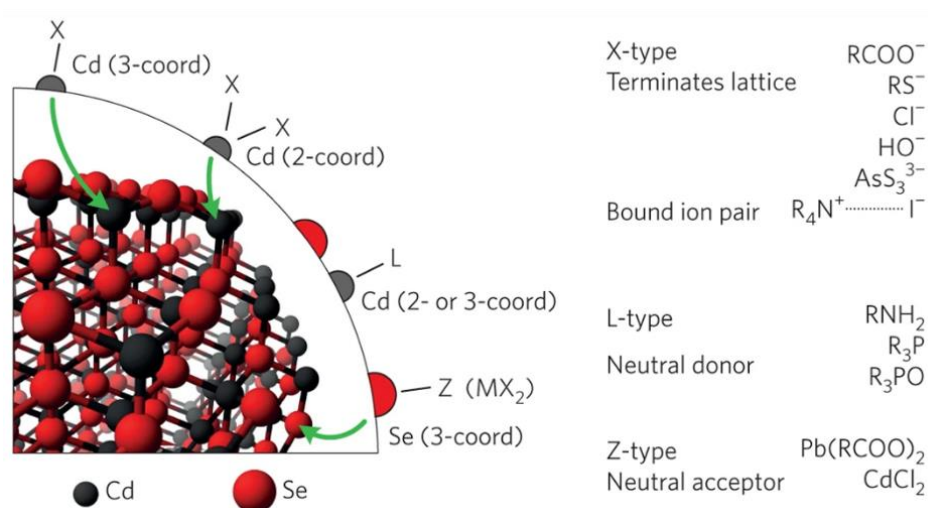


**Figure 1.11** Classification of ligands according to covalent bonding to the surface of CdSe NCs. Reprinted with permission from ref 50. Copyright © 2016 Nature Publishing Group, a division of Macmillan Publishers Limited.

The reactions of colloidal nanocrystals, such as PbSe, PbS and ZnSe, are terminated with X-type oleate ions. By varying the reaction temperature, these nanocrystals can be synthesized to obtain various morphologies (**Figure 1.12**). We have focused on how temperature affects the capping capability of the ligands. In the case of CdSe colloidal nanocrystals [51], the morphologies vary with temperature due to surface energy modulated by the oleate ligand. At 260 °C, a spherical CdSe NCs is shown (Figure 1.12a and b). This spherical shape is thermodynamically dominant growth regime to be shown as the first shape since a spherical shape has the lowest surface area about given volume. Longer reaction time at 260 °C can turn into truncated octahedron by ligand effect. When the temperature is raised to 275 °C, cubic NCs surrounded by a (100) surface appeared due to the weakened adsorption energy of ligand (Figure 1.12c and d). Thus, based on the intrinsic surface stability, the (100) surface is exposed to morphology since the surface energy of (100) surface is the lower than that of (111) surface. As the reaction temperature decreases, capping ligands are adsorbed to the (111) surface, allowing for modulating surface stability due to interactions with exposable surfaces. Therefore, at 250 °C, due to the strong adsorption energy of ligand on the (111) surface, a tetrahedron shape surrounded by the (111) surface is formed as shown in Figure 1.12e and f. When the reaction temperature continues to decrease at 240 °C, the branch-shaped CdSe NCs are obtained as shown in Figure 1.12g and h. This anisotropic shaped structure can be obtained through kinetically controlled growth. After nucleation of zinc-blende core, the arms of wurtzite phase, which is a metastable phase [52], are grown on the zinc-blende core. Based on previous studies, the morphology is dependent on the reaction temperature due to the difference in ligand interaction. In order to technically control the size and morphology of quantum dot materials, we studied the oleate adsorption tendency of the shell material of quantum dot as a function of temperature. We also investigated the morphological change inferred by the relaxed surface energy by oleate ligand adsorption with temperature change in Chapter 4.



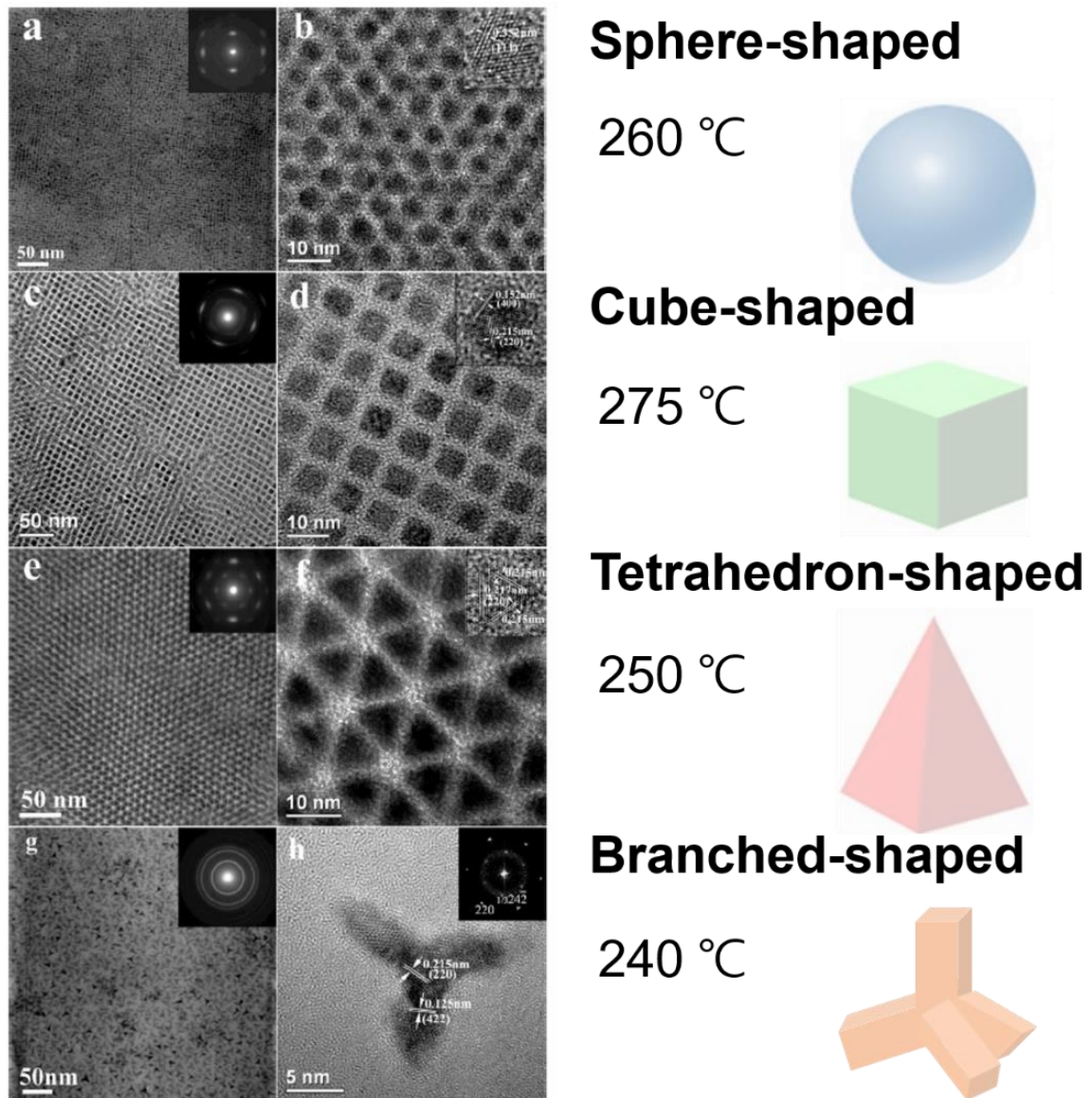


**Figure 1.12** Different shapes of CdSe NCs depending on the temperature. (a, b) sphere, (c, d) cubic, (e, f) tetrahedron, (g, h) branched shapes. Reprinted with permission from ref 51. Copyright © 2009 American Chemical Society.

## 1.3 Simulation Methods

### 1.3.1 Multiscale simulation

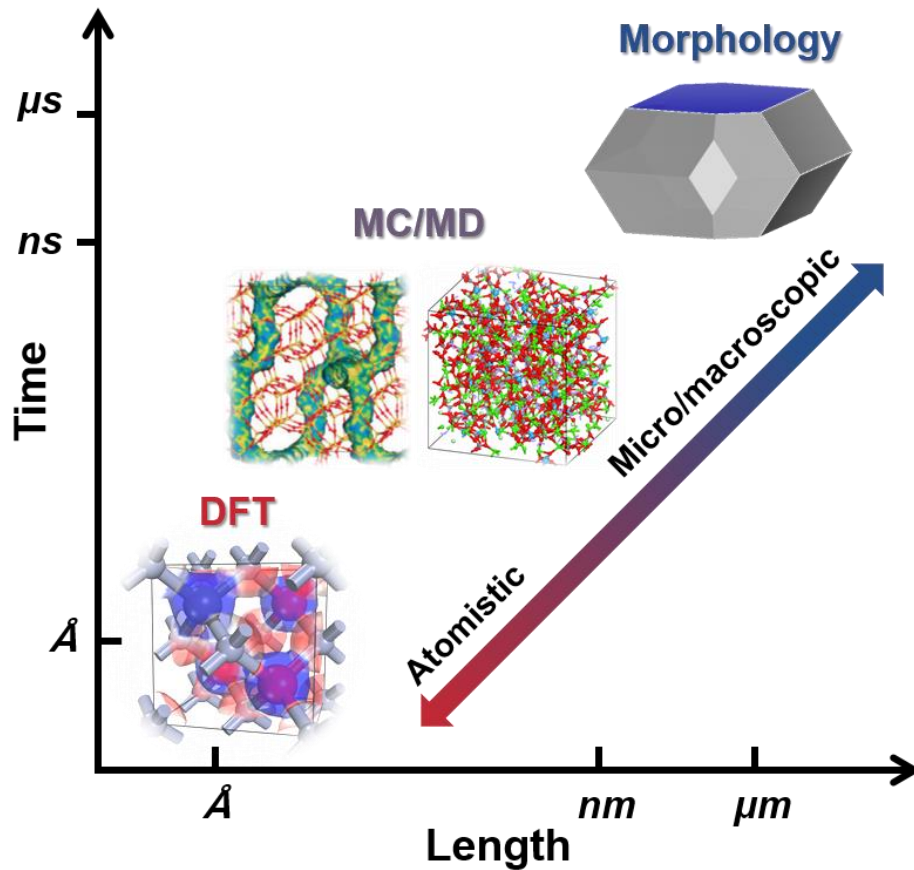


**Figure 1.13** Multiscale computational approach according to time and length scales which covers density functional theory (DFT) calculation, Monte Carlo (MC) simulation and molecular dynamics (MD) simulation, and morphology model.

The multiscale simulation methods are effective to elucidate and describe the realistic phenomena. From the atomistic level to micro or macroscopic level, there are various simulation methods to describe phenomena on each level (**Figure 1.13**). In this dissertation, density functional theory (DFT) calculation, Monte Carlo (MC) simulation, molecular dynamics (MD) simulation, and morphology model are used for theoretical study.

DFT calculation is a quantum mechanical method to investigate the electronic structure of the many-body system. Through the electronic structure analysis such as band structures, density of states, atomic orbitals, we could understand the physic-chemical properties of materials and predict the reaction mechanism. However, due to its high computational cost, the simulation scale and time are limited (i.e., maximum nanoscale and ps) compared to other simulation methods. We have used DFT calculation to

investigate the ion storage mechanism and derive thermodynamic properties such as Gibbs free adsorption energy for stable adsorption structures.

MC and MD simulations describe the physical phenomena based on the interatomic potentials (i.e., forcefield) of each atom. In the case of MC simulations, it is based on the statistical approach that repeats random sampling. The positions and orientations of the sorbate molecules can be found through the trial of the insertion and deletion of adsorbate molecules. Especially, for the MC simulated annealing [53], a number of adsorbate molecules are loaded under variable temperature conditions. As the temperature is slowly decreased from the high temperature through a few cycles, the lowest energy sites for the adsorbate molecules in the system are identified by repeatedly searching the various configuration of adsorbate-adsorbent system. We have used MC simulation to locate where ions can be stored primarily and to seek a stable packing structure for a given molecule. In the case of MD simulation, it is based on Newton's equation that describes the physical movements of atoms under the given temperature and pressure. It is also calculated using forcefield parameters, which requires accurate parameterization to accurately describe the phenomena we want to observe. In these methods, relatively large simulation scale and time length can be applied (i.e., maximum microscale and ns~ $\mu$ s). We have used MD simulation to compare the surface energies of each exposed surfaces and binding energies of interfaces at a given temperature.

### 1.3.2 Morphology model

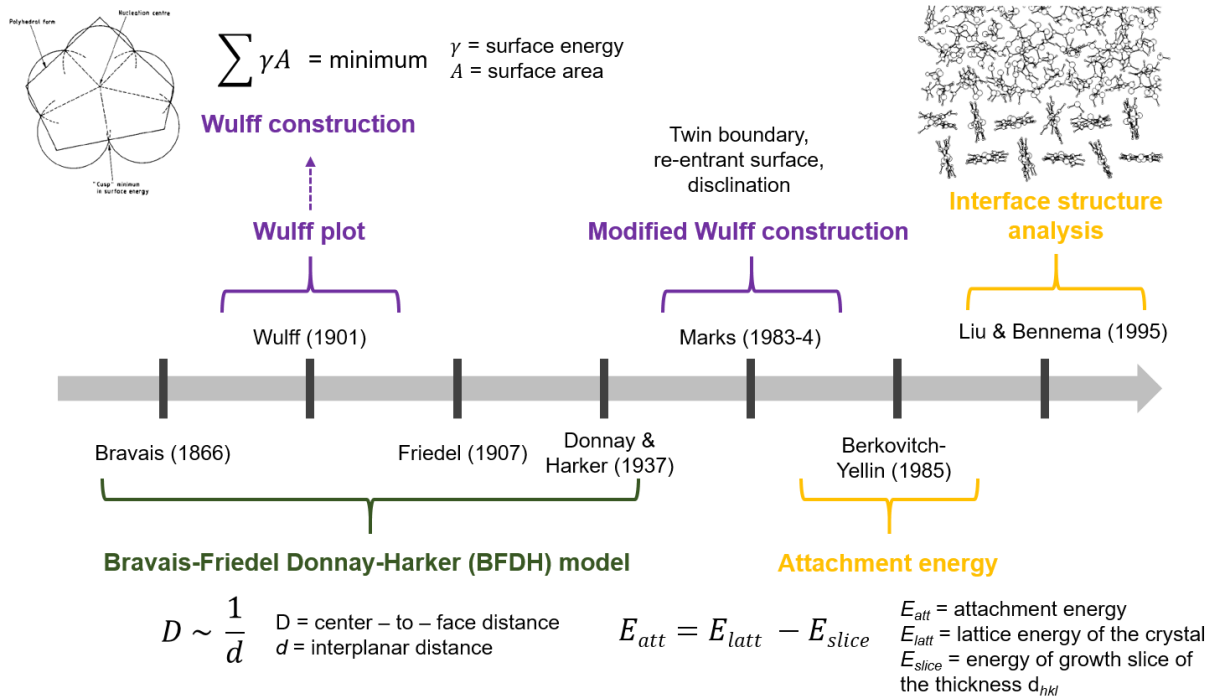


**Figure 1.14** Progress on morphology modelling and theory.

Various morphology models have been developed from morphology model derived from geometric calculations using crystal lattice and symmetry to morphology that considers the external factors such as solvent and additives (**Figure 1.14**).

#### 1.3.2.1 Bravais-Friedel-Donnay-Harker (BFDH) Model [54-56]

The BFDH method is a geometrical calculation using the crystal lattice and symmetry to predict the growth rate based on the crystal structure. The crystal growth rate ( $G_{hkl}$ ) is inversely proportional to the interplanar spacing ( $d_{hkl}$ ) of specific Miller index ( $hkl$ ) as shown below.

$$G_{hkl} \propto \frac{1}{d_{hkl}}$$

In general, the low index surface can be found dominantly which has large interplanar distance. As the larger interplanar distance, the growth rate of ( $hkl$ ) surface is slower, resulting in dominant surface.

### 1.3.2.2 Equilibrium Morphology Model [57]

The equilibrium morphology was predicted based on the relative surface energies of possible surfaces. For a given temperature and volume, the equilibrium morphology is determined by minimizing the total surface free energy.

$$G_{hkl} = \sum_j \gamma_j S_j$$

$\gamma$  and  $S$  is the associated surface energy per unit area and exposed surface area, respectively. The distance from the origin  $H_j$  has the following relation. The distance of the associated surface from the origin is proportional to the specific surface free energy of the surface in the equilibrium shape.

$$\frac{\gamma_1}{H_1} = \frac{\gamma_2}{H_2} = \dots = \frac{\gamma_j}{H_j}$$

Consideration of exposable surface, the lower surface energies, the larger surface area in general. It has an assumption that the surface energy of  $(h k l)$  is the average value of  $(h k l)$  and  $(-h -k -l)$ .

### 1.3.2.3. Crystal Growth Model [58,59]

Based on the periodic bond chain (PBC) theory [60], the attachment energy controls the crystal growth rate, which defined as released energy per mole when an additional layer is deposited on a crystal  $(h k l)$  surface.

$$G_{hkl} \propto |E_{hkl}^{att}|$$

$E_{hkl}^{att}$  is the attachment energy which means the interaction energy between bulk surface and an additional layer. As the attachment energy is higher, growth rate of its surface is faster, resulting in disappearance of its surface. The lattice energy ( $E^{latt}$ ) is defined as the total intermolecular interaction energy per mol, which is related to the sublimation enthalpy ( $E^{latt} = -\Delta H^{sub} - 2RT$ ).  $E^{latt}$  is a constant depending on the given crystal system, which is composed of slice energy ( $E_{hkl}^{slice}$ ) and attachment energy ( $E_{hkl}^{att}$ ).

$$E^{latt} = E_{hkl}^{slice} + E_{hkl}^{att}$$

$E_{hkl}^{slice}$  represents the interaction within the slice of an interplanar distance and  $E_{hkl}^{att}$  represents the interaction of the molecules in the slice. As the attachment energy is lower, the larger exposed surface area.

## 1.4 References

1. S. Park, B. L. Clark, D. A. Keszler, J. P. Bender, J. F. Wager, T. A. Reynolds, and G. S. Herman, *Science* **2002**, *297*, 65.
2. Y. Stehle, Y., H. M. Meyer, R. R. Unocic, M. Kidder, G. Polizos, P. G. Datskos, R. Jackson, S. N. Smirnovm, and I. V. Vlasiouk, *Chem, Mater.* **2015**, *27*, 8041–8047.
3. J. B. Goodenough, and K. S. Park, *J. Am. Chem. Soc.* **2013**, *135*, 1167–1176.
4. K. Chen, Y. Dong Noh, K. Li, S. Komarneni, and D. Xue, *J. Phys. Chem. C* **2013**, *117*, 10770–10779.
5. Y. Zhang, C. Sun, P. Lu, K. Li, S. Song, and D. Xue, *CrystEngComm* **2012**, *14*, 5892–5897.
6. M. A. Neumann, J. Van De Streek, F. P. A. Fabbiani, P. Hidber, and O. Grassmann, *Nat. Commun.* **2015**, *6*, 7793.
7. S. L. Morissette, Ö. Almarsson, M. L. Peterson, J. F. Remenar, M. J. Read, A. V. Lemmo, S. Ellis, M. J. Cima and C. R. Gardner, *Adv. Drug Deliv. Rev.* **2004**, *56*, 275–300.
8. L. Ma, C. Abney, and W. Lin, *Chem. Soc. Rev.* **2009**, *38*, 1248–1256.
9. P. Dandekar, Z. B. Kuvadia, and M. F. Doherty, *Annu. Rev. Mater. Res.* **2013**, *43*, 359–386.
10. J. W. Mullin, *Crystallization*, Butterworth-Heinemann, Oxford, **2001**.
11. R. Strey, P. E. Wagner and Y. Viisanen, *J. Phys. Chem.* **1994**, *98*, 7748–7758.
12. K. S. Gu, and H. Taeghwan, *Small*, **2011**, *7*, 2685–2702.
13. S. Myerson, and B. L. Trout, *Science* **2013**, *341*, 855–856.
14. D. Gebauer, and H. Colfen, *Nano Today* **2011**, *6*, 564–584.
15. S. Karthika, T. K. Radhakrishnan, and P. Kalaichelvi, *Cryt. Growth Des.* **2016**, *16*, 6663–6681.
16. P. J. M. Smeets, A. R. Finney, W. J. E. M. Habraken, F. Nudelman, H. Friedrich, J. Laven, J. De Yoreo, P. M. Rodger, and N. A. J. M., Sommerdijk, *Proc. Natl. Acad. Sci. U.S.A* **2017**, *114*, E7882–E7890.
17. D. Zahn, *ChemPhysChem* **2015**, *16*, 2069–2075.
18. J. Polte, *CrystEngComm* **2015**, *17*, 6809–6830.
19. V. K. LaMer and R. H. Dinegar, *J. Am. Chem. Soc.* **1950**, *72*, 4847–4854.
20. V. K. L. Mer, *Ind. Eng. Chem.* **1952**, *44*, 1270–1277.
21. M. Jung, S. G. Ji, G. Kim, and S. I. Seok, *Chem. Soc. Rev.* **2019**, *48*, 2011–2038.
22. M. A. Neumann, F. J. Leusen, and J. Kendrick, *Angew. Chem.* **2008**, *120*, 2461–2464.
23. J. Cruz-Cabeza, N. Feeder, and R. J. Davey, *Commun. Chem.* **2020**, *3*, 1–4.
24. M. Hiszpanski, R. M. Baur, B. Kim, N. J. Tremblay, C. Nuckolls, A. R. Woll, and Y. -L. Loo, *J. Am. Chem. Soc.* **2014**, *136*, 15749–15756.
25. A. M. Hiszpanski, A. R. Woll, B. Kim, C. Nuckolls, and Y.-L. Loo, *Chem. Mater.* **2017**, *29*, 4311–4316.

26. A. M. Hiszpanski, J. D. Saathoff, L. Shaw, H. Wang, L. Kraya, F. Lüttich, M. A. Brady, M. L. Chabinyk, A. Kahn, P. Clancy, and Y.-L. Loo, *Chem. Mater.* **2015**, *27*, 1892–1900.
27. M. M. Lee, J. Teuscher, T. Miyasaka, T. N. Murakami and H. J. Snaith, *Science* **2012**, *338*, 643–647.
28. J. Burschka, N. Pellet, S.-J. Moon, R. Humphry-Baker, P. Gao, M. K. Nazeeruddin and M. Graätzel, *Nature* **2013**, *499*, 316.
29. F. Hao, C. C. Stoumpos, R. P. H. Chang and M. G. Kanatzidis, *J. Am. Chem. Soc.* **2014**, *136*, 8094–8099.
30. Q. Chen, H. Zhou, T.-B. Song, S. Luo, Z. Hong, H.-S. Duan, L. Dou, Y. Liu and Y. Yang, *Nano Lett.* **2014**, *14*, 4158–4163.
31. E. Eperon, S. D. Stranks, C. Menelaou, M. B. Johnston, L. M. Herz and H. J. Snaith, *Energy Environ. Sci.* **2014**, *7*, 982–988.
32. A. Wakamiya, M. Endo, T. Sasamori, N. Tokitoh, Y. Ogomi, S. Hayase and Y. Murata, *Chem. Lett.* **2014**, *43*, 711–713.
33. X. Guo, C. McCleese, C. Kolodziej, A. C. S. Samia, Y. Zhao and C. Burda, *Dalton Trans.* **2016**, *45*, 3806–3813.
34. J. H. Heo, S. H. Im, J. H. Noh, T. N. Mandal, C.-S. Lim, J. A. Chang, Y. H. Lee, H.-J. Kim, A. Sarkar, M. K. Nazeeruddin, M. Graätzel and S. I. Seok, *Nat. Photonics* **2013**, *7*, 486.
35. W. A. Laban and L. Etgar, *Energy Environ. Sci.* **2013**, *6*, 3249–3253.
36. N. J. Jeon, J. Lee, J. H. Noh, M. K. Nazeeruddin, M. Graätzel and S. I. Seok, *J. Am. Chem. Soc.* **2013**, *135*, 19087–19090.
37. Y. Zhao, A. M. Nardes and K. Zhu, *J. Phys. Chem. Lett.* **2014**, *5*, 490–494.
38. S. A. Fateev, A. A. Petrov, V. N. Khrustalev, P. V. Dorovatovskii, Y. V. Zubavichus, E. A. Goodilin, and A. B. Tarasov, *Chem. Mater.* **2018**, *30*, 5237–5244.
39. Y. Wu, A. Islam, X. Yang, C. Qin, J. Liu, K. Zhang, W. Peng and L. Han, *Energy Environ. Sci.* **2014**, *7*, 2934–2938.
40. Y. Jo, K. S. Oh, M. Kim, K. H. Kim, H. Lee, C. W. Lee and D. S. Kim, *Adv. Mater. Interfaces* **2016**, *3*, 1500768.
41. J.-W. Lee, Z. Dai, C. Lee, H. M. Lee, T.-H. Han, N. De Marco, O. Lin, C. S. Choi, B. Dunn, J. Koh, D. Di Carlo, J. H. Ko, H. D. Maynard and Y. Yang, *J. Am. Chem. Soc.* **2018**, *140*, 6317–6324.
42. Y.-H. Seo, E.-C. Kim, S.-P. Cho, S.-S. Kim, and S.-I. Na, *Appl. Mater. Today* **2017**, *9*, 598–604.
43. Y. Rong, Z. Tang, Y. Zhao, X. Zhong, S. Venkatesan, H. Graham, M. Patton, Y. Jing, A. M. Guloy and Y. Yao, *Nanoscale* **2015**, *7*, 10595–10599.

44. J. Cao, X. Jing, J. Yan, C. Hu, R. Chen, J. Yin, J. Li, and N. Zheng, *J. Am. Chem. Soc.* **2016**, *138*, 9919–9926.
45. A. R. Pascoe, Q. Gu, M. U. Rothmann, W. Li, Y. Zhang, A. D. Scully, X. Lin, L. Spiccia, U. Bach and Y.-B. Cheng, *Sci. China Mater.* **2017**, *60*, 617–628.
46. B. Ding, Y. Li, S.Y. Huang, Q.Q. Chu, C.X. Li, C.J. Li, and G.J. Yang, *J. Mater. Chem. A*, **2017**, *5*, 6840–6848.
47. D. F. Zhang, H. Zhang, L. Guo, K. Zheng, X. D. Han and Z. Zhang, *J. Mater. Chem.*, **2009**, *19*, 5220–5225.
48. M. D. Susman, Y. Feldman, A. Vaskevich and I. Rubinstein, *ACS Nano*, **2014**, *8*, 162–174.
49. C. R. Bealing, W. J. Baumgardner, J. J. Choi, T. Hanrath, and R. G. Hennig, *ACS nano* **2012**, *6*, 2118–2127.
50. M. A. Boles, D. Ling, T. Hyeon, and D. V. Talapin, *Nat. Mater.* **2016**, *15*, 141–153.
51. L. Liu, Z. Zhuang, T. Xie, Y. G. Wang, J. Li, Q. Peng, and Y. Li, *J. Am. Chem. Soc.* **2009**, *131*, 16423–16429.
52. S. Kirkpatrick, C. D. Gelatt, and M. P. Vecchi, *Science* **1983**, *220*, 671–680.
53. U. Soni, V. Arora, and S. Sapra, *CrystEngComm* **2013**, *15*, 5458–5463.
54. A. Bravais, *Etudes Crystallographiques*, Academie des Sciences: Paris **1913**.
55. J. D. H. Donnay and D. Harker, *Am. Mineral* **1937**, *22*, 446–467.
56. G. Friedel, *Bull. Soc. Fr. Mineral.* **1907**, *30*, 326–455.
57. G. Wulff, *Z. Krystallogr.* **1901**, *34*, 449–530.
58. R. Docherty, G. Clydesdale, K. J. Roberts, and P. Bennema, *J. Phys. D: Appl. Phys.* **1991**, *24*, 89–99.
59. Z. Berkovitch-Yellin, *J. Am. Chem. Soc.* **1985**, *107*, 8239–8253.
60. P. Hartman and W.G. Perdok, *Acta. Cryst.* **1955**, *8*, 49–52.



## Chapter 2. Crystal Engineering of Hexabenzocoronene Derivatives and C<sub>60</sub> with Ion Storage Mechanisms for Organic Anode Materials

*This chapter includes the published contents:*

1. Jaehyun Park<sup>†</sup>, Cheol Woo Lee<sup>†</sup>, Se Hun Joo<sup>†</sup>, Ju Hyun Park, Chihyun Hwang, Hyun-Kon Song, Young Seok Park, Sang Kyu Kwak<sup>\*</sup>, Seokhoon Ahn<sup>\*</sup>, and Seok Ju Kang<sup>\*</sup>, “Contorted polycyclic aromatic hydrocarbon: promising Li insertion organic anode” *Journal of Materials Chemistry A*, 6(26), 12589–12597, **2018**  
Reprinted with permission. Copyright © The Royal Society of Chemistry 2018.
2. Jaehyun Park<sup>†</sup>, Cheol Woo Lee<sup>†</sup>, Ju Hyun Park<sup>†</sup>, Se Hun Joo, Sang Kyu Kwak<sup>\*</sup>, Seokhoon Ahn<sup>\*</sup>, and Seok Ju Kang<sup>\*</sup>, “Capacitive Organic Anode Based on Fluorinated-Contorted Hexabenzocoronene: Applicable to Lithium-Ion and Sodium-Ion Storage Cells” *Advanced Science*, 5(12), 1801365, **2018** (†: **equally contributed**)  
Reprinted with permission. Copyright © 2018 The Authors.
3. Jaehyun Park<sup>†</sup>, Se Hun Joo<sup>†</sup>, Yoon-Jeong Kim<sup>†</sup>, Ju Hyun Park, Sang Kyu Kwak<sup>\*</sup>, Seokhoon Ahn<sup>\*</sup>, and Seok Ju Kang<sup>\*</sup>, “Organic Semiconductor Cocrystal for Highly Conductive Lithium Host Electrode” *Advanced Functional Materials*, 29(32), 1902888, **2019**  
Reprinted with permission. Copyright © 2019 WILEY-VCH Verlag GmbH & Co. KGaA, Weinheim.
4. Jaehyun Park<sup>†</sup>, Ju Hyun Park<sup>†</sup>, Minseok Yang<sup>†</sup>, Se Hun Joo, Sang Kyu Kwak<sup>\*</sup>, Seokhoon Ahn<sup>\*</sup>, and Seok Ju Kang<sup>\*</sup>, “Solid Solution of Semiconducting Contorted Small Molecules for High-Performance Li/Na-Ion Host Electrodes” *Energy Storage Materials*, 36, 123–131, **2021** (†: **equally contributed**)  
Reprinted with permission. Copyright © 2020 Elsevier B.V.

### 2.1 Introduction

Graphite is generally considered as an anode material due to their highly reversible discharge–charge performance based on intercalation and de-intercalation processes and compatibility with conventional carbonate aprotic electrolytes [1-3]. However, since the theoretical capacity of 372 mA h g<sup>-1</sup> of graphite is limited to the anode material, considerable efforts have been tried to find alternatives (i.e., alkali-metal-based rechargeable batteries) which satisfy the demands of high-capacity [4-7]. As a next-generation Li-ion battery electrode material other than graphite, many studies have been conducted on potential anode materials, but there are several problems such as large potential hysteresis, phase transformation, and huge volume expansion to exhibit ideal electrochemical performance [8,9]. Therefore, various new carbon-based anode materials such as low-dimensional carbon allotropes

(graphene, CNT, and fullerenes) have been considered candidates for next-generation anodes [10-12]. Several important features of such materials, including a large surface area, short diffusion length of alkali ions, and reversible discharge–charge process, offer a unique surface storage mechanism that can enhance capacity to  $740 \text{ mA h g}^{-1}$  which could be increased further by dopant materials [13-17].

Organic anode materials have been expected and developed to solve the problems in inorganic and carbon-based electrodes. Considering eco-friendly chemical compositions such as carbon, oxygen, nitrogen, and hydrogen, simple redox processes and facile mass production, organic anode materials such as organic salts, conjugated polymers and compounds with carbonyl groups have been extensively studied. Especially, for hexabenzocoronene, which is called HBC, this material also can be flexible tuned by functional groups and control the variable degrees of contortion. Thus, in case of contorted HBC (cHBC), it is known to form molecular wires through  $\pi$ – $\pi$  interaction providing sufficient charge transport in various electronic devices [18-21]. This molecular wire structure from the doubly concave cHBC is expected to provide more sufficient conductivity and a large d-spacing with nanopore channels which enable to easily access Li-ions compared to graphite anode. In addition, the conjugated aromatic structure serves to render it insoluble in electrolytes.

Furthermore, cHBC can be modified by electron-withdrawing group through fluorination to improve the conductivity of semiconducting organic materials [21-25]. Fluorine shifted the energy levels downward with the lowest unoccupied molecular orbital (LUMO) energy level down, which is shifted more than the highest occupied molecular orbital (HOMO) energy level [24]. By tuning the bandgap, it is expected that fluorinated cHBC (F-cHBC) accelerate the charge transfer. Beyond using dopant, we systemically designed the solid solution and cocrystal. In case of the solid solution, it is one of the effective and promising approach for enhancing the physical and chemical characteristics of pure materials. Owing to the strong interrelationship between two individual components, a continuum quasi-isostructural compound with novel properties could be formed [26-31]. In particular, through forming the solid solution from transition metal-based inorganic materials, significant enhancements have been reported in the properties of energy storage and harvesting devices as a result of efficient bandgap engineering of semiconducting materials. Thus, we designed highly conductive organic solid solution battery anodes using double concaved both cHBC and F-cHBC for high-performance Li-ion hosting electrode with conducting agent-free. Their molecular and crystal structure similarity, which improves the charge transport property, enables them to form a homogeneous solid solution with the desired material properties.

Moreover, by smartly selecting the *n*-type material of fullerene ( $C_{60}$ ), we developed the conducting agent-free  $C_{60}$ /cHBC cocrystal anode. We have considered electron conductivity of organic materials, which can form *p*–*n* junctions at molecular level. The cHBC molecule which has negative curvature can make molecular shape complementarity with a  $C_{60}$  single molecule. Thus, the unique shape of

contorted semiconducting cHBC material enables it to form a cocrystal with the ball-shaped C<sub>60</sub> molecule at the optimum stoichiometry, effectively enhancing the electron transport. It can enhance the electron transfer but also facilitates vacant sites for Li-ion storage with an excellent reversible capacity and a stable, long cycle life.

The important characteristics of these materials are the flexible structure modification and decent electrochemical performance. These studies present the new types of organic anode materials designed to achieve stable cycling performance, superior electrochemical performance, and reversible Li insertion/de-insertion by large d-spacing and storage space of anode materials at molecular level. Following the fundamental crystalline phase and Li insertion studies based on the electrochemical performance, we finally validate that the contorted aromatic molecules provide the optimized crystalline structure for Li-ion access and storage, potentially providing a new design concept for organic anode materials in Li-ion batteries.

## 2.2 Computational details

### 2.2.1 Crystal structure prediction

The computational polymorphism study was carried out using the Polymorph module of the Materials Studio 2019 [32]. Using the optimized structure of component molecules as input, the *ab initio* prediction of polymorphs was performed sequentially in six steps (i.e., packing, clustering, geometry optimization, clustering, geometry optimization, and clustering). In the packing step, the crystal structures belonging to a specific space group were sampled using Monte Carlo simulated annealing. The packing procedure was performed for 10 different space groups:  $P2_1/c$ ,  $P\bar{1}$ ,  $P2_12_12_1$ ,  $C2/c$ ,  $P2_1$ ,  $Pbca$ ,  $Pna2_1$ ,  $Cc$ ,  $Pbcn$ , and  $C2$ . To achieve sufficiently wide sampling, we set the maximum temperature to  $1.5 \times 10^5$  K, the minimum temperature to 300 K, the maximum number of steps to 500,000, the number of steps to accept before cooling to 100, the minimum move factor to  $1.0 \times 10^{-50}$ , and the heating factor to 0.025. In the geometry optimization step, the lattice parameters and atomic positions were relaxed under crystallographic symmetry. Each component molecule was treated rigid body in the first geometry optimization step, while it was fully relaxed in the second geometry optimization step. The maximum number of steps was set to 10,000 and the convergence criteria were set to  $2.0 \times 10^{-5}$  kcal mol<sup>-1</sup> for the maximum energy change, 0.001 kcal mol<sup>-1</sup> Å<sup>-1</sup> for the maximum force, 0.001 GPa for the maximum stress, and  $1.0 \times 10^{-5}$  Å for the maximum displacement. In the clustering step, many similar structures were grouped into clusters, and the lowest energy structure representing each cluster was filtered. The criterion of crystal similarity measure was set to 0.11, which was calculated based on a comparison of radial distribution functions with a cutoff distance of 7 Å and 140 bins. After the final clustering step, the space group symmetry of the predicted crystal structures was re-analyzed, and the *in-silico* screening was carried out on the basis of XRD comparison. The interatomic interactions were described by COMPASS II force field [33] and calculated using the Ewald summation method [34,35].

### 2.2.2 Monte Carlo (MC) simulation

To figure out the specific adsorption sites of Li-ions in the crystal structure, Monte Carlo simulated annealing was performed using the Sorption module of Materials Studio 2019 [32]. Based on the metropolis algorithm, the Monte Carlo simulated annealing was carried out with the maximum number of loading steps of  $1.0 \times 10^5$ , the maximum number of production steps of  $1.0 \times 10^8$ , and 40 annealing cycles. All simulations were repeated 5 times independently. The interatomic interactions were described by COMPASS II force field [33] with Mulliken [36] charges obtained by DFT calculations.

### 2.2.3 Density functional theory (DFT) calculation

DFT calculations were performed using the CASTEP program [37]. The generalized gradient approximation with the Perdew–Burke–Ernzerhof (GGA-PBE) functional [38] was used to describe the exchange correlation potential of the electrons. The interactions between ions and electrons were described by on-the-fly generated norm-conserving pseudopotentials. The plane-wave basis set with a cutoff energy of 840 eV was employed to expand the wave functions. The van der Waals interactions were corrected using Grimme’s method [39]. The convergence criterion for self-consistent field calculation was set to  $5.0 \times 10^{-7}$  eV atom<sup>-1</sup>. Lattice parameters and atomic positions were fully relaxed. The convergence criteria for geometry optimization were set to  $5.0 \times 10^{-6}$  eV atom<sup>-1</sup> for energy, 0.01 eV Å<sup>-1</sup> for force, 0.02 GPa for stress, and  $5.0 \times 10^{-4}$  Å for displacement. All calculated systems were sampled with Monkhorst–Pack *k*-point meshes of actual spacing of about 0.04/ Å. [40]. The formation energy ( $E_f$ ) of the inserted structure as a function of Li-ion content was calculated as follows:

$$E_f = E_{\text{Li}_n\text{-cryst}} - E_{\text{cryst}} - nE_{\text{Li}}$$

where  $E_{\text{Li}_n\text{-cryst}}$  is the total energy of each crystal system with adsorbed Li-ions,  $n$  is the number of adsorbed Li-ions,  $E_{\text{cryst}}$  is the total energy of each crystal system, and  $E_{\text{Li}}$  is the total energy per atom of bcc bulk Li. The voltage profile as a function of Li-ion content was calculated as follows:

$$V(n) = - \frac{E_{\text{Li}_{n_2}\text{-cryst}} - E_{\text{Li}_{n_1}\text{-cryst}} - (n_2 - n_1)E_{\text{Li}}}{q(n_2 - n_1)}$$

where  $E_{\text{Li}_{n_1}\text{-cryst}}$  and  $E_{\text{Li}_{n_2}\text{-cryst}}$  represent the total energy of each crystal system with inserted Li-ions,  $n_1$  and  $n_2$  are the numbers of adsorbed Li-ions ( $n_2 > n_1$ ), and  $q$  is the net charge of Li-ions ( $q = +1e$ ).

### 2.2.4 HOMO and LUMO energy levels

To estimate the HOMO and the LUMO energy levels of cHBC and F-cHBC molecules, spin-polarized DFT calculations were conducted using the DMol3 program [41,42]. The Becke’s three-parameter hybrid exchange functional combined with the Lee-Yang-Parr correlation functional (B3LYP) [43,44] was employed for describing the exchange-correlation potential of electrons. The DNP 4.4 basis set was used with a global orbital cutoff of 3.7 Å. The core electrons were explicitly treated as all electrons with relativistic effect. The long-range van der Waals interactions were corrected using the Grimme’s method [39]. The self-consistent field calculation was performed with the fixed orbital occupancy, until

the convergence criterion of  $1.0 \times 10^{-6}$  was satisfied. The convergence criteria for geometry optimization were set to  $1.0 \times 10^{-5}$  Ha for the maximum energy change,  $0.002 \text{ Ha } \text{\AA}^{-1}$  for the maximum force, and  $0.005 \text{ \AA}$  for the maximum displacement, respectively.

## 2.3 Results and Discussion

### 2.3.1 Contorted hexabenzocoronene (cHBC)

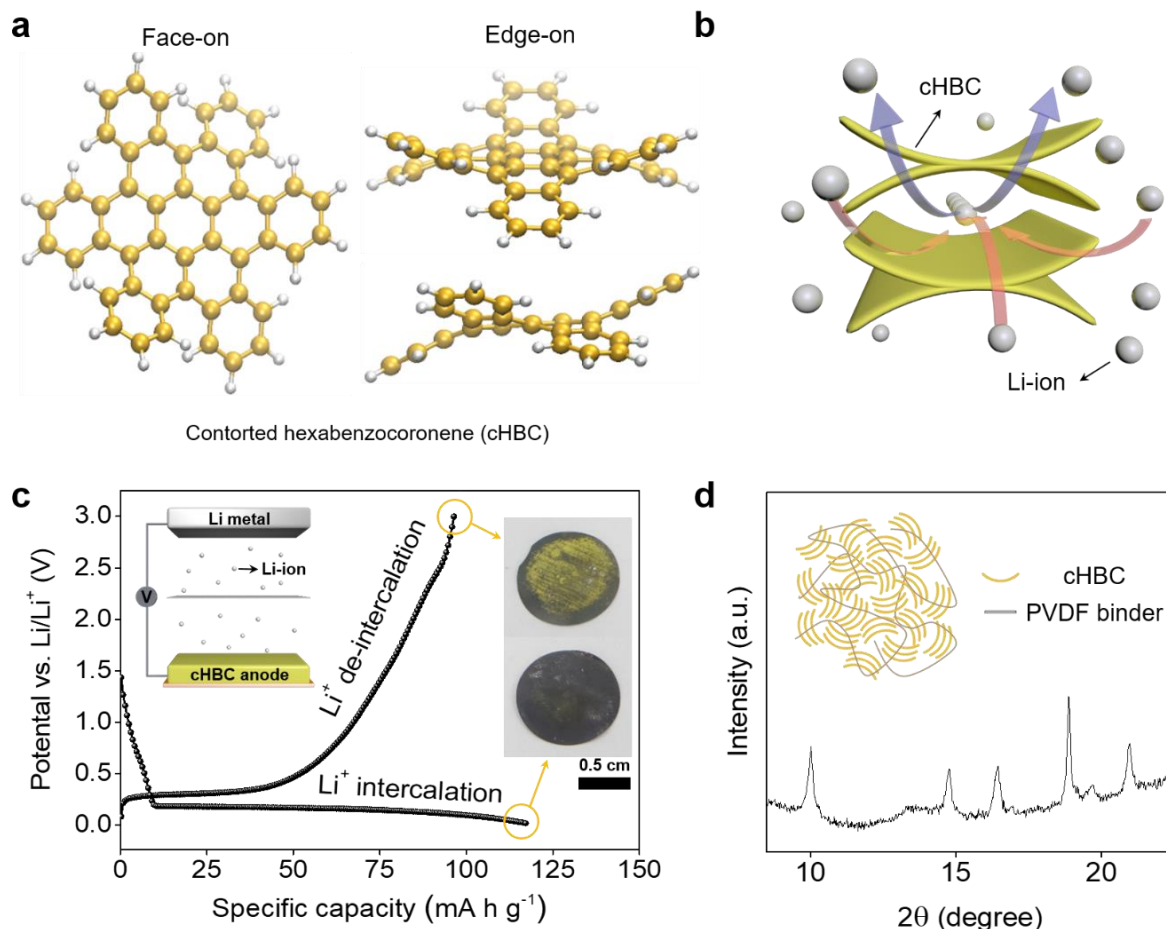


**Figure 2.1** (a) Face-on (left) and edge-on (right) molecular structure of cHBC. The crystal structure of cHBC exhibits two concave surfaces. (b) Schematic of proposed Li-ion intercalation mechanism in cHBC. (c) Galvanostatic discharge–charge voltage profile of a Li metal/separator/cHBC anode half-cell at a current density of  $0.1 \text{ A g}^{-1}$ . The inset figures show digital photographs of cHBC anode after Li<sup>+</sup> de-intercalation and after Li-intercalation. (d) XRD pattern of as-synthesized cHBC. The inset figure represents schematic of cHBC slurry, which consists of cHBC and a poly(vinylidene fluoride) binder.

A cHBC molecule, which consists of 13 aromatic rings, has a doubly concave molecular structure with a distorted pentacene core. It produced hierarchical structure due to its unique molecular structure (**Figure 2.1a**). We adopted cHBC crystal as the Li host material in a Li-ion battery. This structure potentially benefits Li-ion intercalation and lead to the improved performance of Li-ion battery. The schematic presented in **Figure 2.1b** shows the proposed Li-ion intercalation mechanism in the cHBC crystal. We hypothesize that the relatively small aromatic molecules of the cHBC crystal lower the

energy barrier of Li-ion intercalation at the edge of the cHBC crystal as well as reduce diffusion in the crystal interspace. **Figure 2.1c** represents galvanostatic discharge–charge profiles of the cHBC anode with a Li metal electrode. The discharge capacity of approximately  $120 \text{ mA h g}^{-1}$ , which is relatively smaller than a conventional carbon-based graphite electrode despite it having a similar aromatic ring structure. One of the expected reasons for relatively lower capacity is the uncontrolled crystal phase of cHBC and its crystallinity, which can be eroded cell performance. The structure of as-prepared cHBC anode was analyzed by X-ray diffraction (XRD) measurement (**Figure 2.1d**). It represented the polymorph II crystal phase of cHBC material [19]. Therefore, additional processing conditions such as solvent and thermal annealing would be required to enhance the capacity of the cHBC material.

Through additional processing such as tetrahydrofuran (THF) solvent and high-temperature ( $\sim 170 \text{ }^\circ\text{C}$ ) thermal annealing [19], the polymorphic change in cHBC material was developed to transform to polymorph II and polymorph II'. As shown in **Figure 2.2a**, the final structure of cHBC anode is polymorph II' which verified by high-flux synchrotron grazing incidence X-ray diffraction (GIXD). The results clearly indicated that an annealing temperature  $>260 \text{ }^\circ\text{C}$  significantly enhanced both the crystallinity of the cHBC anode and the development of the polymorph II' phase. To investigate the crystal phase of polymorph II', we performed an in-depth computational polymorphism study using Monte Carlo simulated annealing combined with clustering and geometry optimization. As a result of *in silico* polymorph screening, the XRD pattern of the polymorph II' phase of cHBC exactly matched that of the  $R\bar{3}$  space group (**Figure 2.2b**). The main diffraction peaks of the experimental powder XRD pattern, located at  $10.14^\circ$ ,  $13.40^\circ$ ,  $19.08^\circ$ ,  $21.28^\circ$ ,  $23.24^\circ$ ,  $23.98^\circ$ , and  $26.54^\circ$ , corresponding to a scattering vector  $q$  of  $0.72$ ,  $0.95$ ,  $1.35$ ,  $1.51$ ,  $1.64$ ,  $1.69$ , and  $1.87 \text{ \AA}^{-1}$ , were assigned to the (101), (110), (003), (211),  $(11\bar{3})$ ,  $(21\bar{2})$ , and (104) planes, respectively. The Rietveld refinement result (red line) was found in good agreement with the experimental XRD pattern (black line), as evidenced by their negligible difference (green line) and the low final residual factors (i.e., 4.20% for  $R_p$  and 6.74% for  $R_{wp}$ ). The Rietveld refinement suggests a trigonal crystal system with lattice parameters of  $a = 13.24 \text{ \AA}$ ,  $b = 13.24 \text{ \AA}$ , and  $c = 13.93 \text{ \AA}$  and  $\alpha = 90^\circ$ ,  $\beta = 90^\circ$ , and  $\gamma = 120^\circ$  for the unit cell with the  $R\bar{3}$  space group. The resulting GIXD and computational investigation allowed us to conclude that the polymorph II' phase of the cHBC anode belongs to the trigonal  $R\bar{3}$  space group, where cHBC molecules have ABC stacking configuration, an interlayer distance of  $4.64 \text{ \AA}$ , and consistent molecular orientation, as shown in **Figure 2.2c**.



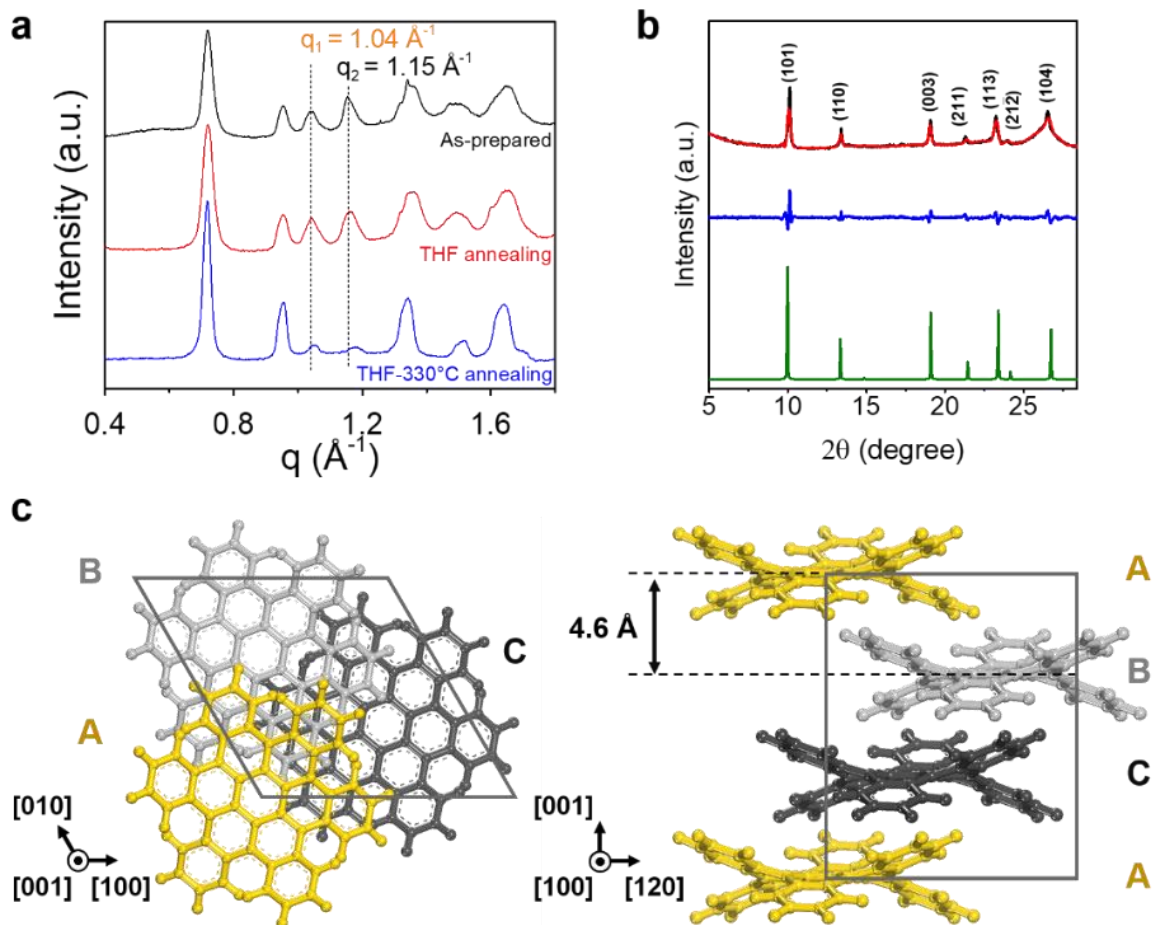


**Figure 2.2** (a) 1D diffraction traces for the sample series with as-prepared (black line), THF-annealed (red line), and THF-330 °C annealed (blue line) cHBC films. Significantly decreased peaks at both  $q_1 = 1.04$  and  $q_2 = 1.15 \text{ \AA}^{-1}$  indicate the phase transformation of cHBC from polymorph II to polymorph II'. (b) XRD patterns of cHBC: experimental (black line), Rietveld refined (red line), their difference (green line), and the  $R\bar{3}$  crystal phase (blue line). (c) Projection views of the  $R\bar{3}$  crystal phase along [001] and [100] directions, respectively. For clarity, the cHBC molecules in different layers are represented by yellow, light gray, and dark gray colors.

To investigate the cell performance of well-developed  $R\bar{3}$  crystal phase of cHBC through the THF solvent and subsequent thermal annealing treatment, we performed galvanostatic discharge–charge measurements at a fixed current density of  $0.2 \text{ A g}^{-1}$  within the cutoff range of 0.02–3.00 V (**Figure 2.3a**). We employed Super P as a conducting agent (ratio: 8.0/1.0/1.0 wt.%) to enhance the conductivity of the sample, which was subsequently dried at  $120 \text{ }^\circ\text{C}$  in a vacuum oven for 2 hours to eliminate solvent residue. The resulting electrochemical characteristics of discharge–charge trajectories of the half-cell structure show that the specific capacity of cHBC anodes is strongly dependent on the processing conditions of subsequent treatments. The THF– $330 \text{ }^\circ\text{C}$  annealed cHBC anode shows the highest specific capacity of approximately  $250 \text{ mA h g}^{-1}$ , i.e., approximately 1.8 times higher than the THF solvent annealed sample.

Interestingly, and contrary to conventional graphite, cHBC anode exhibits a single anodic peak at 0.21 V in the  $dQ \text{ dV}^{-1}$  plot for the THF– $330 \text{ }^\circ\text{C}$  annealed sample, suggesting that lithiation occurs in a single-step process (**Figure 2.3b**). This behavior is strikingly different from that of the typical multiple-staging effects of graphite anodes. Our conjecture is that the single-stage lithiation process originates from the contorted structure of the cHBC molecules. The doubly concave molecular structure with bent edge aromatic rings in the stacked cHBC molecules generates empty pores between the molecules, resulting in the 3D ordering of the pores in the crystal structure (**Figure 2.3c**). The free volume of the  $R\bar{3}$  crystal phase of cHBC, estimated by the Connolly surface using a Li-ion as a probe (i.e., radius =  $0.76 \text{ \AA}$ ), was  $0.088 \text{ cm}^3 \text{ g}^{-1}$ , whereas the free volume of graphite was estimated as zero (**Figure 2.3d**). In addition, the 3D ordered pores of cHBC enable 3D diffusion of Li-ions, contrary to the 2D diffusion channel of graphite. We hypothesize that the large free volume together with the 3D diffusion channel in cHBC facilitates the accommodation of Li-ions during lithiation.

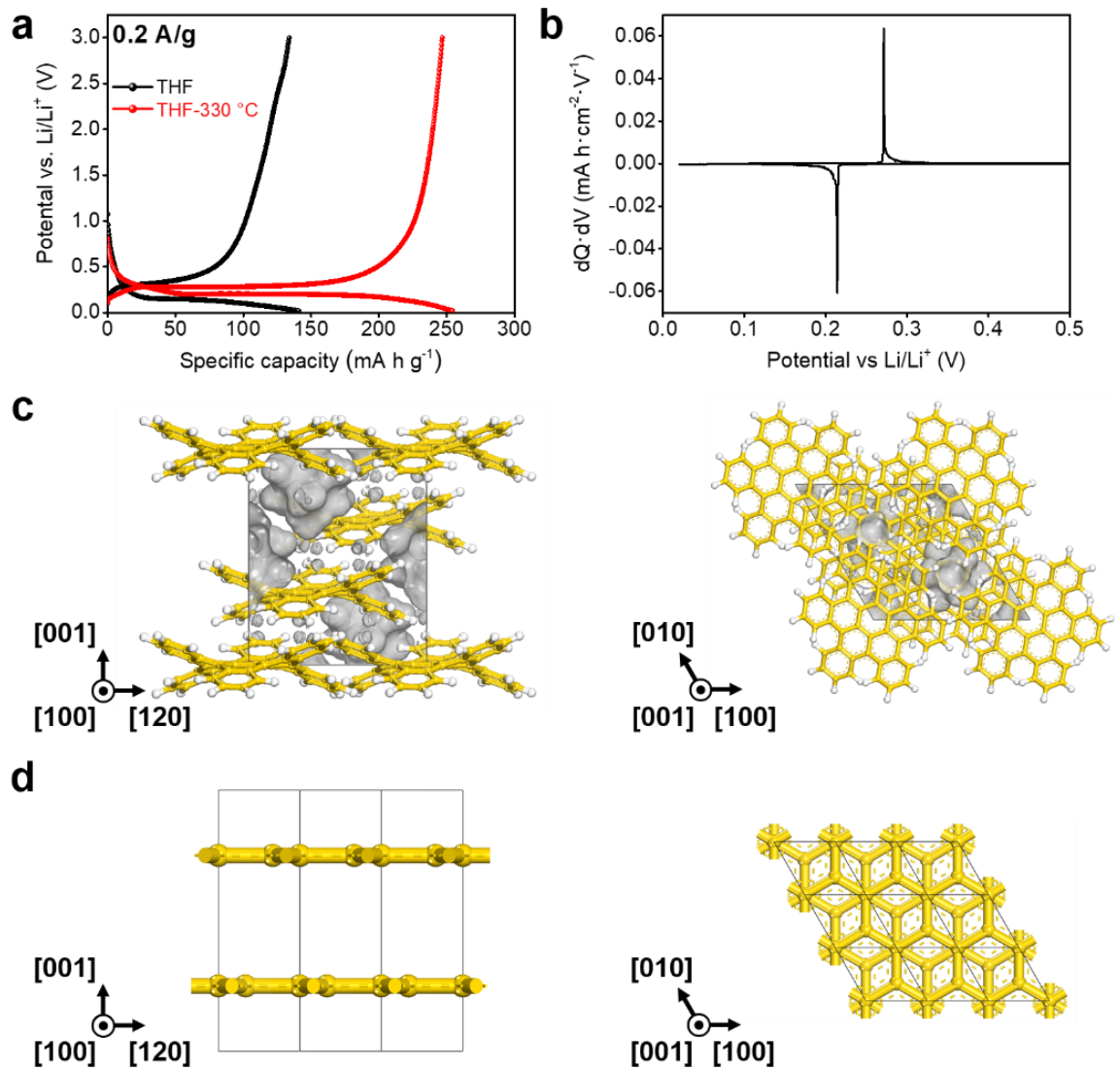


**Figure 2.3** (a) Galvanostatic discharge–charge profiles of THF-annealed (black dotted line) and THF–330 °C annealed (red dotted line) cHBC anodes at fixed current density of 0.2 A g<sup>-1</sup>. (b) The differential capacity curve of the THF–330 °C annealed cHBC anode. (c) R $\bar{3}$  crystal phase and (d) graphite projection views with Connolly surface. Carbon and hydrogen are colored yellow and white, respectively.

To explore the Li-ion intercalation sites of cHBC, we performed grand canonical Monte Carlo simulations in combination with DFT calculations. The energetically favorable intercalation sites of Li-ions in the  $R\bar{3}$  cHBC crystal phase were found to be the empty pores of the surface. In particular, the Li-intercalated cHBC was found to have the highest stability with the lowest formation energy of  $-5.8$  eV, when a Li-ion was intercalated into a pore with a negative electrostatic potential between the bent edge aromatic rings of the cHBC molecules, as shown in **Figure 2.4**. In addition, we calculated the formation energy of Li-intercalated cHBC and the voltage profile as a function of Li-ion content. Here, Li-ions were inserted into the unit cell of the  $R\bar{3}$  crystal phase in multiples of three (i.e., 3, 6, 9, and 18 Li-ions), considering the most energetically favorable intercalation sites and crystallographic symmetry, as shown in **Figure 2.5a**. Formation energies of Li-intercalated cHBC as a function of Li-ion content, where the lowest formation energies for each of the contents of Li-ion form an energy convex hull (red line), as shown in **Figure 2.5b**. The energy convex hull shows that the Li-intercalated cHBC starts to become unstable when more than 18 Li ions are inserted, indicating that the  $R\bar{3}$  crystal structure of cHBC could store up to 6 Li ions per molecule. This result is in good agreement with the experimental capacity (i.e.,  $267 \text{ mA h g}^{-1}$ ). Furthermore, the calculated voltage profile with an average value of  $0.27 \text{ V}$  matches that observed experimentally in terms of both the single plateau and the energy involved in the lithiation process, as shown in **Figure 2.5c**. These results suggest that the single-stage intercalation process is mainly due to Li-ion intercalation into 3D ordered empty pores, which is attributed to the contorted molecular structure of cHBC.

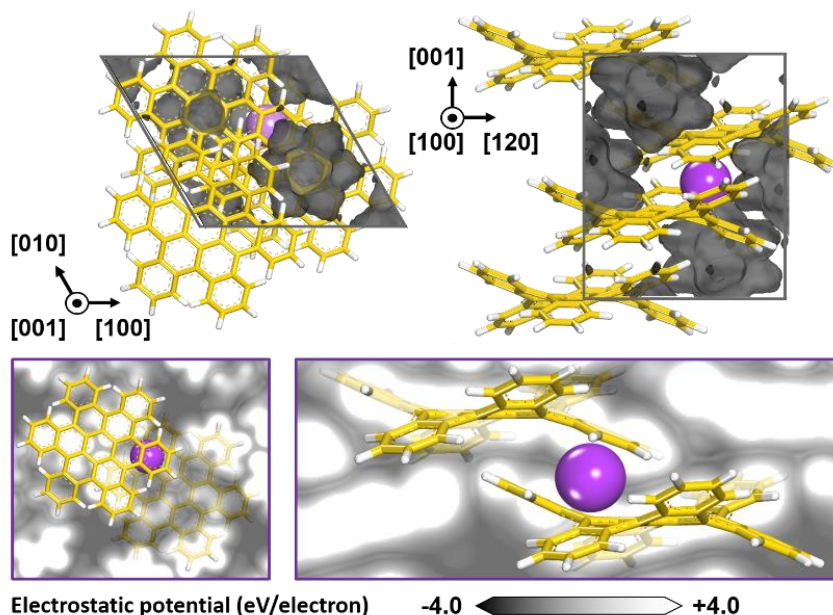


**Figure 2.4** The optimized structure of Li-intercalated cHBC and the electrostatic potential maps of cHBC without Li-ion. The electrostatic potential is mapped onto the Connolly surface (top) and (001) and (010) planes across the center of Li-ion (bottom left and right). Carbon, hydrogen, and lithium are colored yellow, white, and purple, respectively.

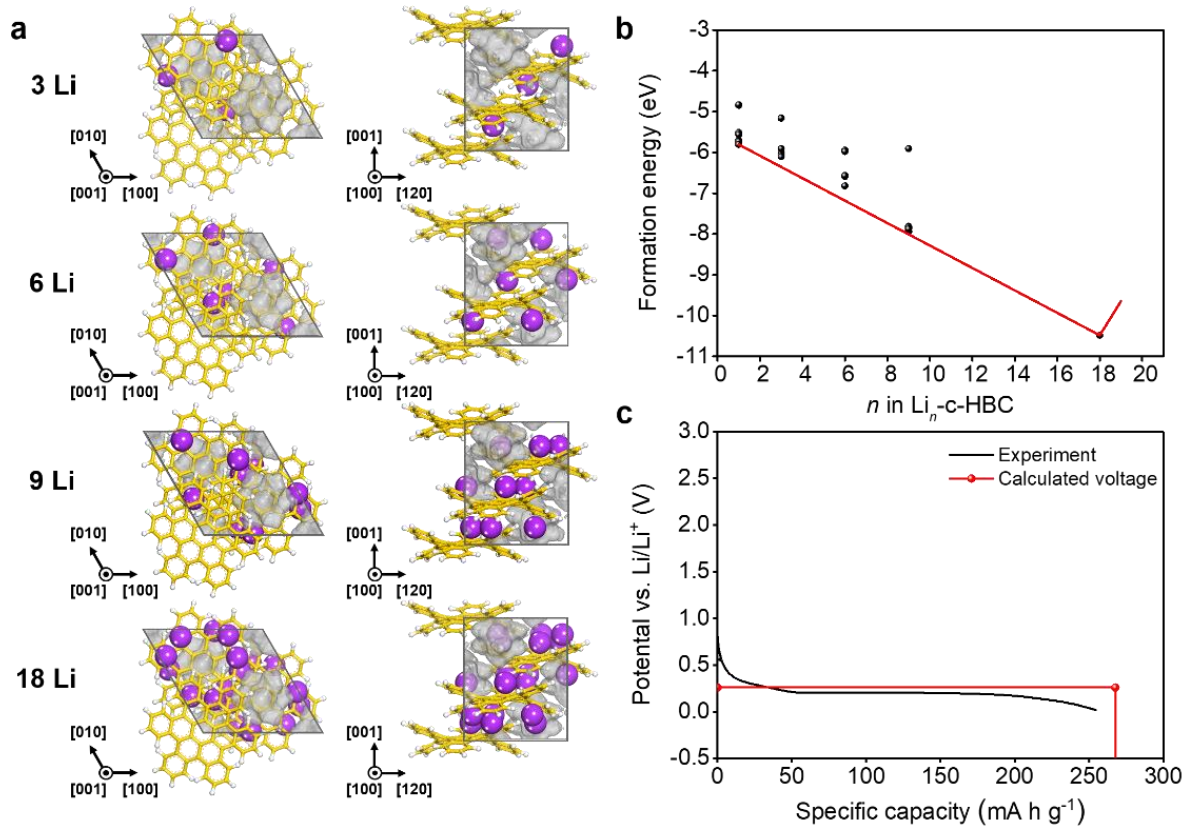


**Figure 2.5** (a) Projection views of the optimized stable structures of 3, 6, 9, and 18 Li-intercalated  $R\bar{3}$  crystal phase. Carbon, hydrogen, and lithium are colored yellow, white, and purple, respectively. (b) Formation energies of Li-intercalated cHBC as a function of the number of Li ions. The convex hull is shown as a red line. (c) The experimental (black line) and calculated (red line) voltage profiles.

### 2.3.2 Fluorinated contorted hexabenzocoronene (F-cHBC)

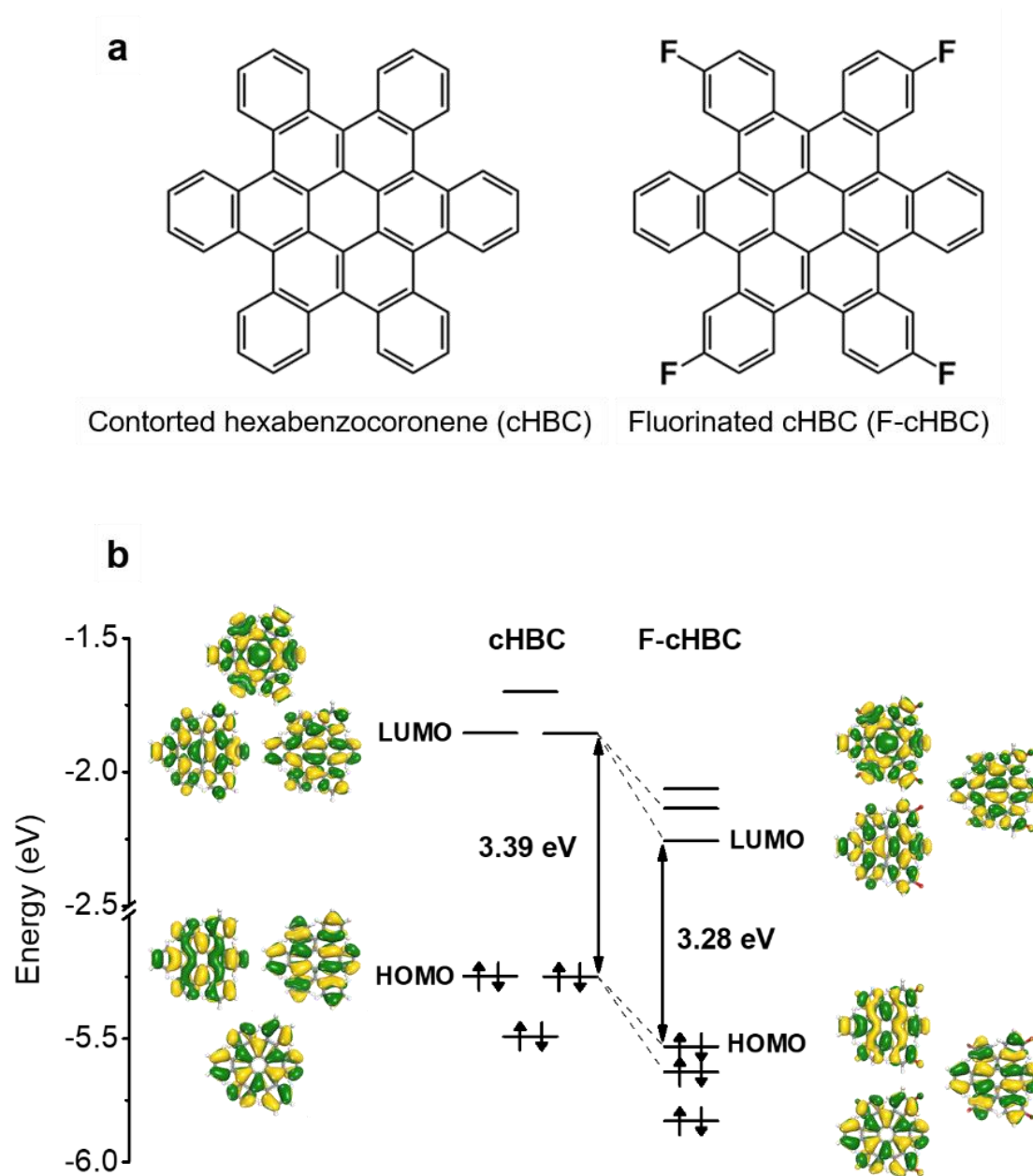


**Figure 2.6** (a) Chemical structures and (b) energy diagrams of the molecular orbitals of contorted hexabenzocoronene (cHBC) and fluorinated cHBC (F-cHBC).

The comparison of chemical structure of cHBC and F-cHBC molecules is represented in **Figure 2.6a**. F-cHBC contains four fluorine atoms at the ends of cHBC that is thought to change the bandgap of the cHBC molecule [19,45]. The HOMO and LUMO energy levels of F-cHBC were estimated by DFT calculation. The fluorine substitution causes two degenerate HOMO and LUMO energy levels to split and to decrease from  $-5.247$  to  $-5.533$  eV for HOMO, and  $-1.856$  to  $-2.257$  eV for LUMO (**Figure 2.6b**). The decreased HOMO-LUMO energy levels of F-cHBC can facilitate the charge transfer. The

detailed crystal structure (polymorph I) of F-cHBC sample was characterized by XRD pattern. The *in-silico* polymorph screening revealed that the experimental XRD pattern of polymorph I phase of F-cHBC matched well with the XRD pattern of the  $P2_1/c$  crystal phase (**Figure 2.7a**). Prominent peaks at  $7.04^\circ$ ,  $12.68^\circ$ ,  $14.06^\circ$ ,  $14.50^\circ$ ,  $16.66^\circ$ ,  $18.08^\circ$ ,  $18.86^\circ$ ,  $21.84^\circ$ ,  $22.18^\circ$ ,  $23.24^\circ$ , and  $24.10^\circ$  were assigned to the (100), (011), (200), (111), (012), (112), (211), (212), (020), (120), and (121) planes, respectively. Rietveld refinement result suggested the presence of a  $P2_1/c$  crystal phase with lattice parameters of  $a = 12.62 \text{ \AA}$ ,  $b = 8.04 \text{ \AA}$ ,  $c = 14.22 \text{ \AA}$ ,  $\alpha = 90.00^\circ$ ,  $\beta = 89.89^\circ$ , and  $\gamma = 90.00^\circ$  (**Figure 2.7b**).

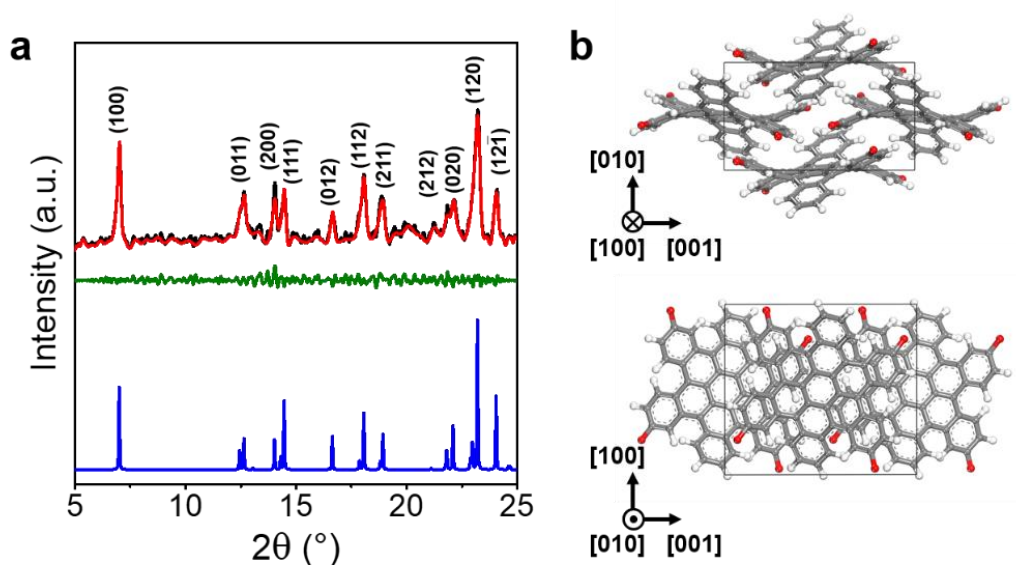


**Figure 2.7** (a) XRD patterns of F-cHBC: experimental (black line), Rietveld refined (red line), their difference (green line), and the  $P2_1/c$  crystal phase (blue line). ( $R_{wp} = 13.21\%$ ,  $R_p = 9.74\%$ ), (b) Projection views of the  $P2_1/c$  crystal structure along [100] and [010] directions, respectively. Carbon, hydrogen, and fluorine are grey, white, and red, respectively.

As previously mentioned by cHBC anode, to investigate the electrochemical performance, we carefully characterized galvanostatic discharge–charge behavior of the F-cHBC  $P2_1/c$  crystal phase at various current density ( $100\text{--}7000 \text{ mA g}^{-1}$ ) and voltage ranging ( $0.02\text{--}3.00 \text{ V}$  versus  $\text{Li/Li}^+$ ). As shown in the **Figure 2.8a**, the voltage profile of F-cHBC anode dropped continuously until the cutoff potential of  $0.02 \text{ V}$  and provided a reversible specific capacity of  $\sim 160 \text{ mA h g}^{-1}$  at current density of  $0.1 \text{ A g}^{-1}$ . This voltage trajectory was consistent regardless of applied current, and the recorded cyclic voltammetry (CV) profiles (**Figure 2.8b**) show broad anodic and cathodic peaks, which indicate that the mechanisms of Li-ion uptake and release differ in the F-cHBC anode [46]. To evaluate the difference, we estimated the kinetics of the F-cHBC anode by using the equation of  $i_p = av^b$ , where  $i_p$  is the peak current,  $v$  is the sweep rate, and  $a$  and  $b$  are fitted parameters [46,47]. The informative  $b$  parameter can

be determined from the slope of the plots of  $\log(i_p)$  versus  $\log(v)$ . When  $b$  value is 1, we can expect that the capacitive behavior is the dominant process in the cell. On the contrary, the  $b$  value of 0.5 reveals diffusion-controlled intercalation process (i.e., battery characteristic). However, in case of ours, the calculated  $b$  value exhibits 0.87 from the CV curves at scan rate from 0.1 to 1.0  $\text{mV s}^{-1}$ . Although the  $b$  value is close to 1, this intermediate value suggests that the characteristic of F-CHBC anode is transitional between capacitive and battery characteristics (**Figure 2.8c**). The quantitative contribution of capacitive and battery processes can be further quantified by the equation of  $i(V) = k_1v + k_2v^{1/2}$ , where  $k_1v$  represents the contribution of capacitive process, and  $k_2v^{1/2}$  is the contribution of diffusion-controlled intercalation [46,48]. The resulting integrated area of stored charge (i.e., capacitance) was 74 % of the total integral and reflected the main reaction of F-CHBC anode is capacitance dominated pseudocapacitive process (**Figure 2.8d**).

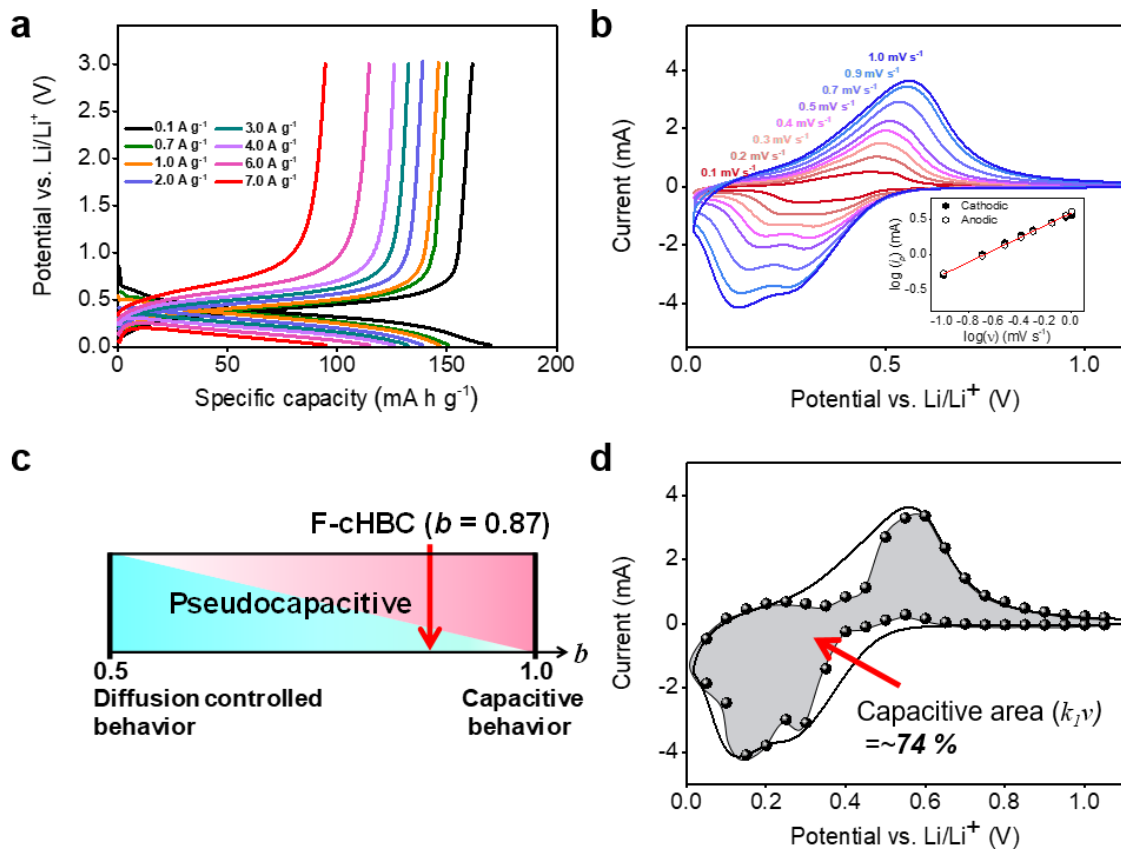


**Figure 2.8** (a) Galvanostatic discharge–charge profiles of F-CHBC anode. (b) Cyclic voltammograms of cell containing F-CHBC at scan rates from 0.1 to 1.0  $\text{mV s}^{-1}$ . The inset figure represents log–log plot of scan rate ( $v$ ) versus peak current ( $i_p$ ) and regression to estimate  $b$ . (c) Change in contributions of pseudocapacitive behavior. F-CHBC is located in the pseudocapacitive area. (d) CV curve at 1.0  $\text{mV s}^{-1}$ . Shaded region represented the capacitive contribution ( $k_1v$ ) to total charge storage.



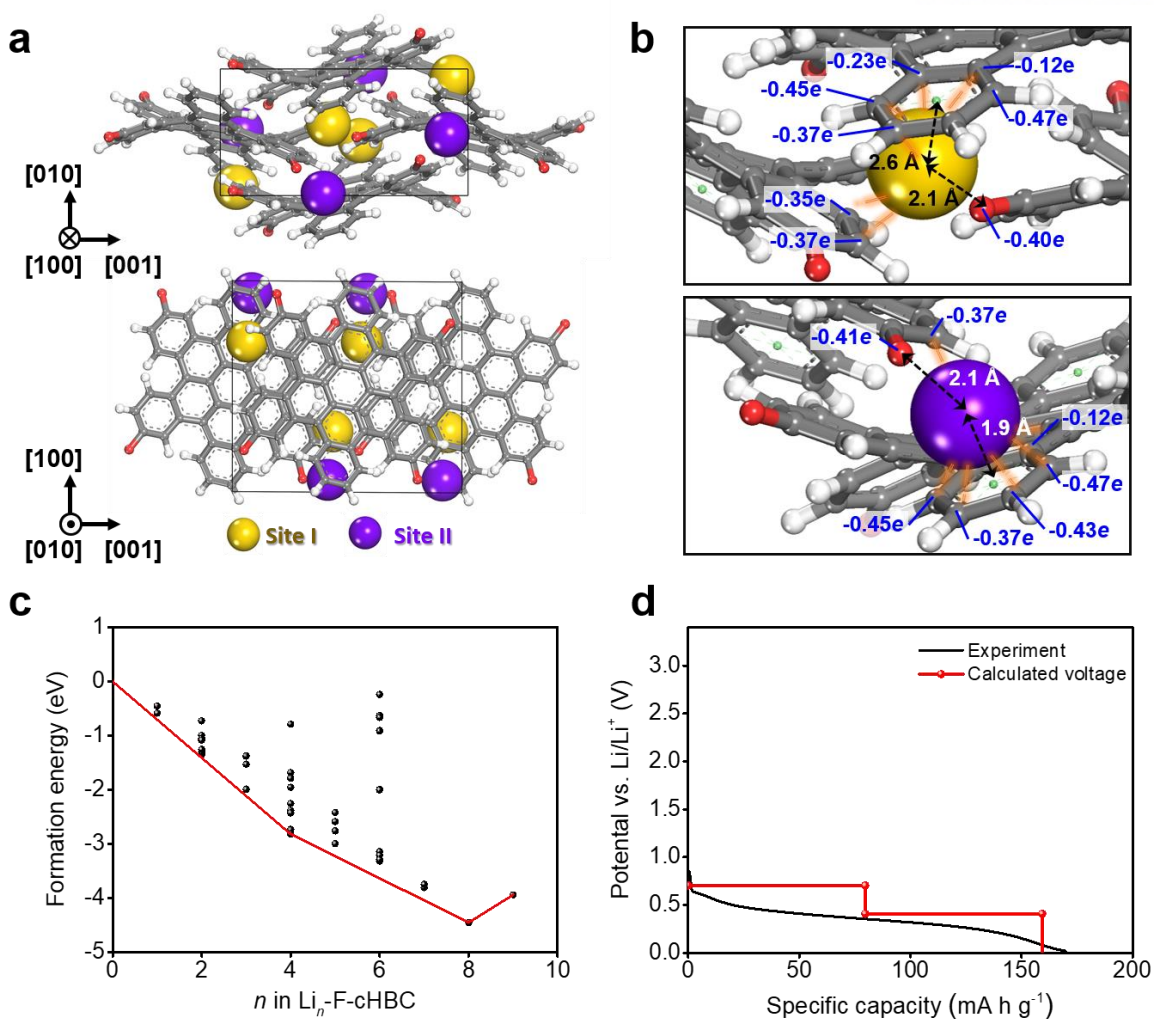


**Figure 2.9** (a) Projection views of optimized  $P2_1/c$  crystal structure of Li-adsorbed F-cHBC along [100] (top) and [010] (bottom) directions. Grey: Carbon, red: fluorine, white: hydrogen yellow: lithium in site I, purple: lithium in site II. (b) Magnified view of Li-ion at site I (top) and site II (bottom). Black dotted arrow: distance between Li-ion and fluorine or between Li-ion and the centroid of the bent edge aromatic ring. Orange line: interaction of adsorbed Li-ion with negatively-charged atoms. (c) Formation energies of Li-adsorbed F-cHBC as a function of Li-ion content. Red line: convex hull. (d) Experimental (black line) and the calculated (red line) voltage profiles.

To identify the adsorption sites of Li-ions in the  $P2_1/c$  crystal phase of F-cHBC, we examined three-dimensional space within the crystal structure by using a probe with a radius of  $0.76 \text{ \AA}$  (i.e., the radius of Li-ion) to construct the Connolly surface. Almost empty spaces are located near the fluorine atoms; these spaces may be capable of accommodating and storing Li-ions. To determine whether the empty spaces are active sites that provide the energy-storage capacity, we combined Monte Carlo simulations and DFT calculations. The empty spaces have two distinct sites, denoted as site I and site II (**Figure 2.9a**). Crystallographic symmetry yields four identical sites for each of sites I and II in the unit cell of

the  $P2_1/c$  crystal phase. All sites I and II are surrounded by electronegative fluorine atoms and the negatively-charged bent edge aromatic ring of the F-cHBC molecule (**Figure 2.9b**); the distances between Li-ion and fluorine atom are 2.1 Å in site I, and 1.9 Å in site II. The distances between Li-ion and the centroid of the bent edge aromatic ring are 2.6 Å in site I, and 2.1 Å in site II. For the total of eight identified sites in the unit cell, we calculated the formation energies of F-cHBC with  $n$  adsorbed Li-ions ( $\text{Li}_n\text{-F-cHBC}$ ) as a function of  $n$  (**Figure 2.9c**). Formation energy of 4 Li-ions was lowest (i.e., -2.82 eV) when all of the Li-ions are located in site I. Then, additional 4 Li-ions were located at site II. When sites I and site II were fully occupied by eight Li-ions (i.e.,  $\text{Li}_8\text{-F-cHBC}$ ), the lithiated F-cHBC crystal phase was most thermodynamically stable (i.e., -4.45 eV). This result suggests that the Li-ions are preferentially located in site I rather than site II since Li-ions are further from each other at site I than at site II. When the number of adsorbed Li-ions is greater than nine, it become unstable; each F-cHBC molecule with four fluorine atoms can store up to four Li-ions. This result is in good agreement with the experimental capacity (i.e.,  $\sim 160 \text{ mA h g}^{-1}$  at current density of  $100 \text{ mA g}^{-1}$ ). Furthermore, the calculated voltage profile is consistent with observed continuous voltage drop during Li-ion storage experiment (**Figure 2.9d**); this similarity supports hypothesis that Li-ions are adsorbed at site I and site II near fluorine atoms.

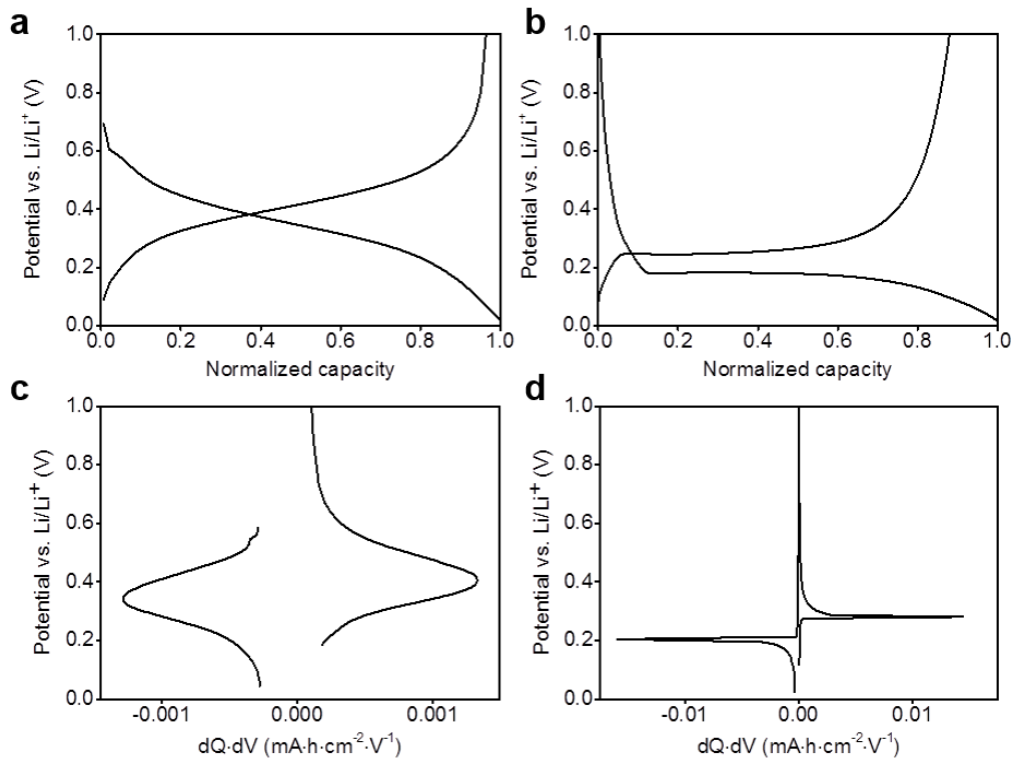


**Figure 2.10** (a) Galvanostatic discharge–charge profiles of (a) F-cHBC and (b) cHBC anodes contained in Li-ion cells. Corresponding differential capacity curves of (c) F-cHBC and (d) cHBC anodes.

We compared the electrochemical performances of cHBC and F-cHBC as shown in **Figure 2.10**. The voltage trajectory and its  $dQ \, dV^{-1}$  plots clearly contrasted. cHBC anode exhibited conventional Li-ion intercalation such as redox reactions of carbonyl group-based organic electrodes [49-51]. The conventional battery-like behavior exhibits distinct reduction and oxidation peaks. Thus, these differences between F-cHBC and cHBC can be originated from the adsorption sites of Li-ions.

### 2.3.3 cHBC/F-cHBC solid solution

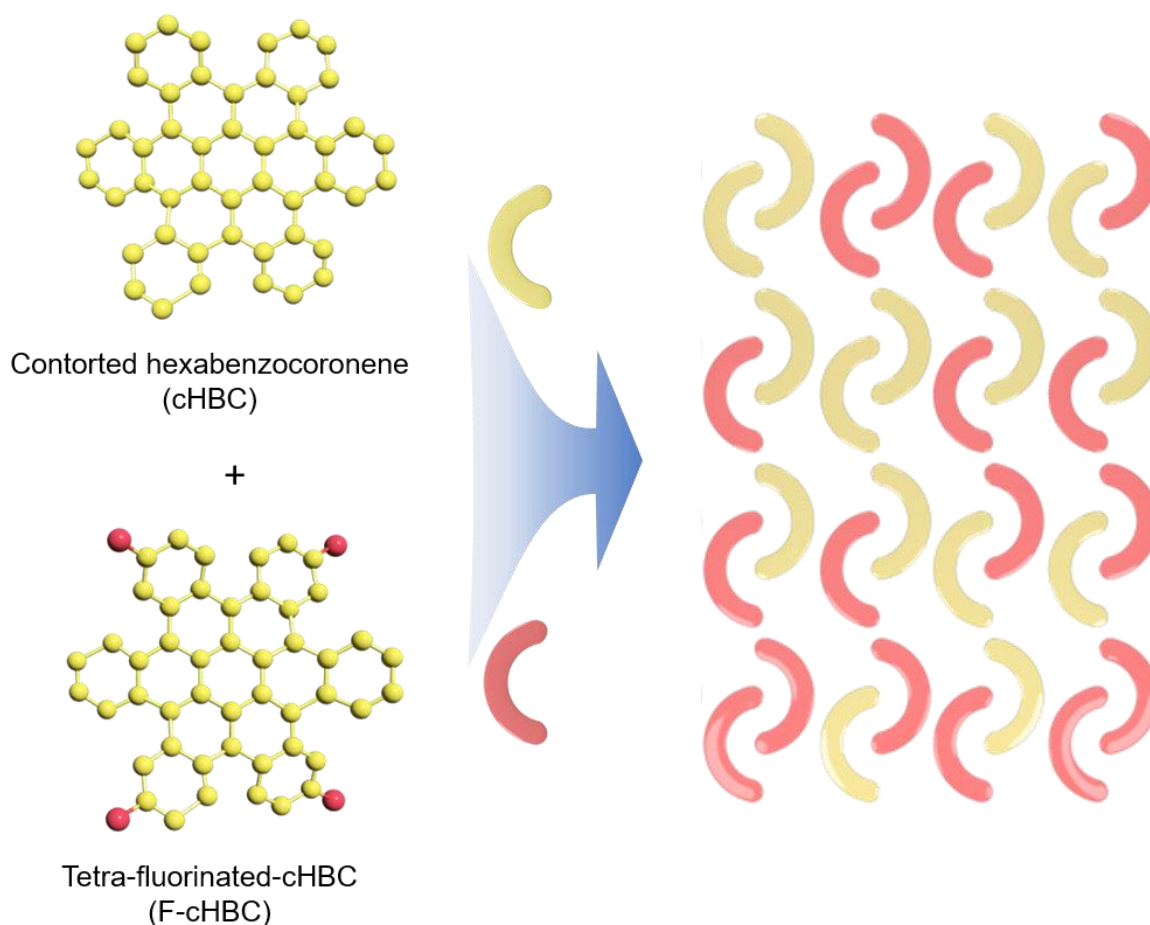


**Figure 2.11** Schematic of solid solution formation using cHBC and F-cHBC molecules. Carbon and fluorine atoms are colored by yellow and red, respectively.

Through mixed cHBC and F-cHBC for a high energy density electrode, we systemically synthesized a cHBC/F-cHBC compound (**Figure 2.11**). Depending on the blend ratio of cHBC and F-cHBC, the different morphologies appeared (not shown). For understanding these crystal solid phases, 1D diffraction traces for cHBC, F-cHBC, and blended films were shown in **Figure 2.12a**. Compared with pristine materials, the blended films with various ratios showed both the two distinct peaks of pure cHBC ( $q \approx 0.69 \text{ \AA}^{-1}$ ) and F-cHBC ( $q \approx 0.49 \text{ \AA}^{-1}$ ). These peaks were shifted progressively without evolving the new diffractions. The linearly shifted 1D diffraction from the crystalline blend films reveals the correlation between original crystal lattices from the pristine cHBC and F-cHBC components; these are the fingerprints of the solid solution according to Vagard's law [52]. We further conducted electrochemical performance of cHBC, F-cHBC, solid solution electrode at ratios of 3:7 and 5:5. Interestingly, the lithiated solid solution electrode was transformed from mixed as shown in **Figure 2.12b**. We found the shifted first-order peak at  $q \approx 0.51 \text{ \AA}^{-1}$  and the diffraction at  $q \approx 0.69 \text{ \AA}^{-1}$  disappeared. Regardless of blending ratio (i.e., 3:7 and 5:5 solid solution electrodes), the crystal phase

of solid solution film was fully transformed during the initial lithiation. XRD patterns of cHBC/F-cHBC electrodes from the first lithiation process are shown in **Figure 2.12c**. The transformed crystal phase is not notably changed by further cycling, which implies that the irreversible phase transition occurs at the first cycle and is maintained during battery cycling (**Figure 2.12d**). This irreversible phase transition at the first cycle has been observed in the ketone-type disodium rhodizonate ( $\text{Na}_2\text{C}_6\text{O}_6$ ) organic cathode material used in Na-ion batteries [53,54]. Previous studies claimed that additional electrons supplied during the sodiation process increased the instability of the initial structure, which consequently changed into the energetically favorable structure after the full sodiation of the anode material. Although a cHBC/F-cHBC solid solution electrode is different from the previously proposed disodium rhodizonate, the experimental results suggest that the cHBC/F-cHBC solid solution electrode also stabilizes the molecular structure during the first lithiation process.

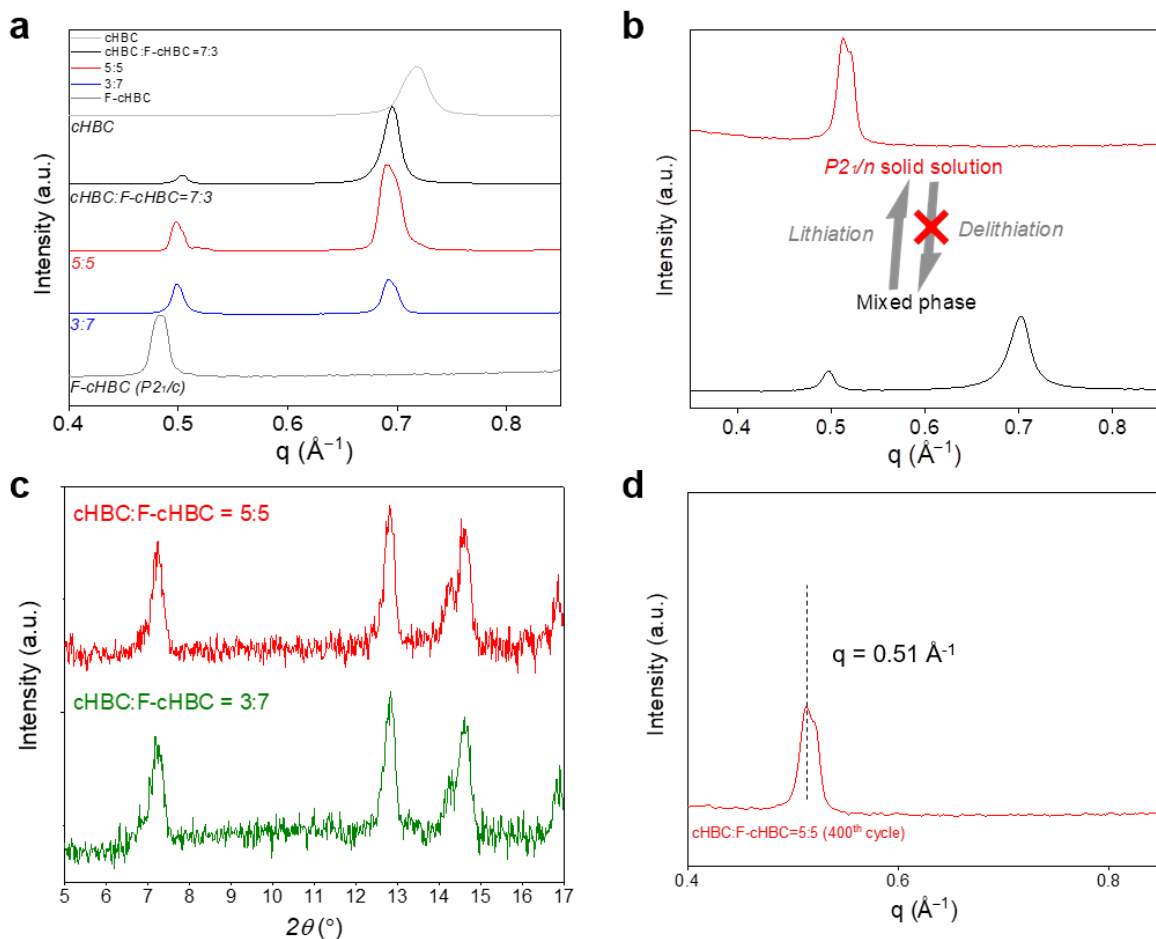


**Figure 2.12** (a) 1D diffraction traces of 2D GIWAXS results of cHBC, cHBC/F-cHBC blend ratios of 7:3, 5:5, 3:7, and F-cHBC electrode. (b) 1D diffraction traces of the pristine and fully lithiated cHBC/F-cHBC electrodes. (c) Postmortem X-ray diffraction patterns of solid solution electrodes (5:5 and 3:7) after fully lithiation. (d) 1D diffraction trace of 2D GIWAXS of lithiated cHBC/F-cHBC 5:5 electrode after 400 cycles in cell.

The evolved crystal structure of cHBC/F-cHBC solid solution after the lithiation process was further determined by computational screening of various solid solution structures sampled through the Monte Carlo simulated annealing process. The simulated XRD pattern of cHBC/F-cHBC solid solution structure was well matched with  $P2_1/n$  crystal phase (**Figure 2.13a**), indicating that the most uniformly mixed state of cHBC and F-cHBC at the molecular level is energetically stable as shown in **Figure 2.13b**. This implies that the formation of a cHBC/F-cHBC solid solution is thermodynamically preferred over the phase separation of cHBC and F-cHBC. When cHBC and F-cHBC are fully mixed, a well-defined molecular junction is formed between cHBC and F-cHBC molecules with different HOMO/LUMO energy levels; each cHBC (F-cHBC) molecule is surrounded by eight F-cHBC (cHBC) molecules. This molecular junction in the solid solution is likely to have contributed to the enhancement of charge transport reported in the semiconducting organic cocrystal.

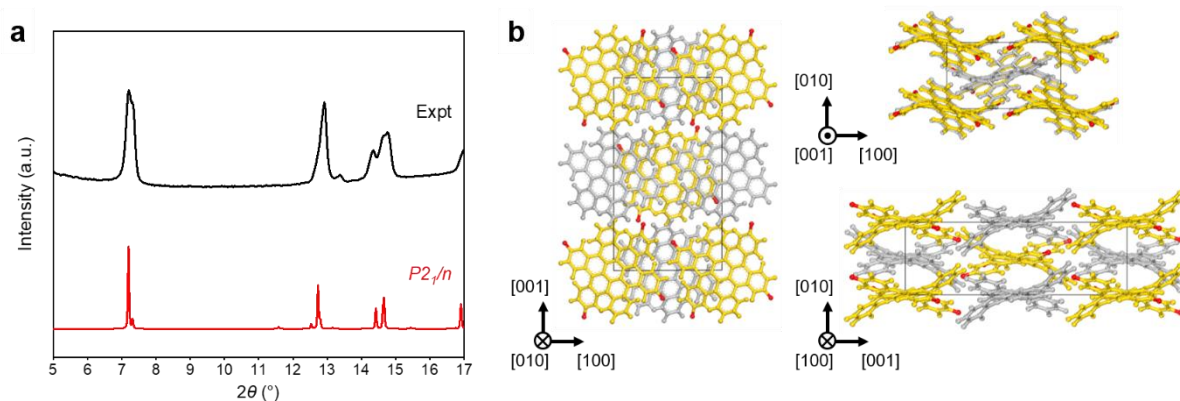


**Figure 2.13** (a) Comparison of the 1D diffraction trace of the lithiated cHBC/F-cHBC (5:5) electrode and the simulated XRD pattern of  $P2_1/n$  crystal phase of cHBC/F-cHBC solid solution. (b) Projection views of  $P2_1/n$  crystal phase of cHBC/F-cHBC solid solution along [010], [001], and [100] directions. cHBC and F-cHBC molecules are shown in gray and yellow, respectively. Note that fluorine is shown in red.

As shown in the charge-discharge voltage curves at the fixed current density of  $0.1 \text{ A g}^{-1}$  in **Figure 2.14a**, the solid solution electrode with a blend ratio of 5:5 delivers the highest reversible capacity of  $350 \text{ mA h g}^{-1}$ , which is approximately four times higher than that of the pristine cHBC anode ( $80 \text{ mA h g}^{-1}$ ). These results indicate that the formation of a solid solution at certain blend ratios enhances the reversible specific capacity. The reason for these high capacities at high current rates is the unique crystal structure of the cHBC/F-cHBC solid solution. Well-developed molecular level assembly between semiconducting cHBC and F-cHBC molecules enhances the electron transfer in the blend film due to the relatively lower LUMO level of F-cHBC molecule. Also, these provide sufficient charge transport for low voltage hysteresis due to the formation of a molecular junction between cHBC and F-cHBC, which generates effective vacant sites for Li-ion accessibility with excellent reversibility. We

also compared the anodic and cathodic peaks as a function of scan rates using the equation  $i_p = av^b$ —where  $i_p$  is peak current from cyclic voltammetry (CV) measurement. As a result, the observed  $b$  values of 0.69 and 0.64 for the anodic and cathodic peaks, respectively, indicate that the dominant contribution of 5:5 solid solution electrode is battery behavior. The capacitive contribution was further calculated using the equation  $i(V) = k_1v + k_2v^{0.5}$ , where  $k_1v$  and  $k_2v^{0.5}$  are attributed to the capacitive and diffusion-limited processes, respectively. As shown in **Figure 2.14b**, the blend ratios of 5:5 film exhibited  $\approx 30\%$  of the capacitive region in the CV profile at scan rate of  $0.4 \text{ mV s}^{-1}$ , which matches well with the  $b$ -values calculated inset figure. This capacitive portion may originate from the F-cHBC molecules in the solid solution films. The strong negative electrostatic potential of fluorine atoms ultimately increases the Li-ion accessibility, as previously reported for the single component of F-cHBC anode. To elucidate the Li-ion storage mechanism of the  $P2_1/n$  crystal phase of cHBC/F-cHBC solid solution, Monte Carlo simulations and DFT calculations were performed. Considering various Li-ion storage sites, we calculated the formation energies of the crystal phase of the cHBC/F-cHBC solid solution with Li-ions (**Figure 2.14c**). The energy convex hull, defined by the lowest formation energies for each concentration of Li-ion, shows that the crystal phase of the cHBC/F-cHBC solid solution becomes unstable when more than 36 Li-ions are stored; the theoretical capacity is  $379 \text{ mA h g}^{-1}$ , which is consistent with the experimental capacity of  $350 \text{ mA h g}^{-1}$ . The configurations of the crystal phase of the cHBC/F-cHBC solid solution with Li-ions and the voltage profile calculated along the convex hull are shown in **Figure 2.14d**. Each detailed lithiation mechanism was shown in **Figure 2.15**.

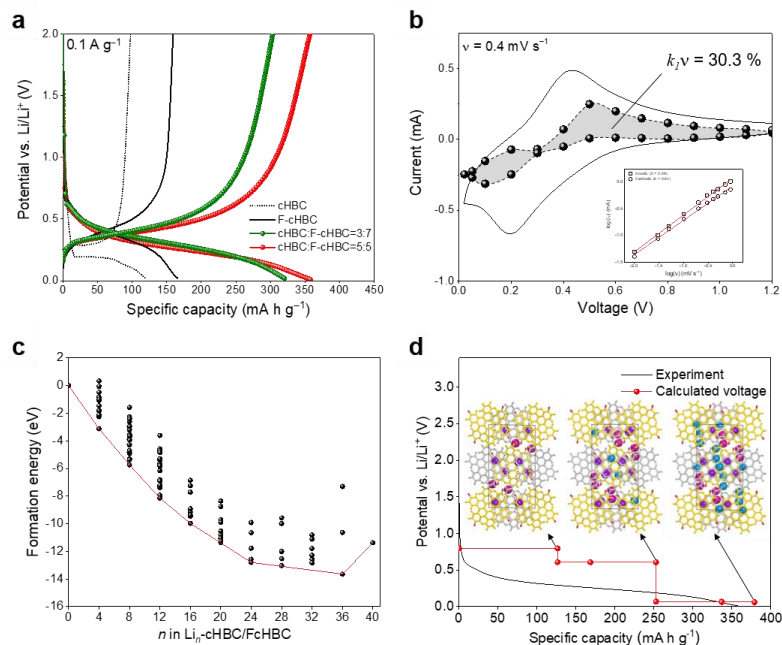


**Figure 2.14** (a) Galvanostatic charge-discharge profiles of cHBC, F-cHBC, and cHBC/F-cHBC blend solid solution electrodes with ratio of 3:7 and 5:5. (b) CV profiles at sweep speed of  $0.4 \text{ mV s}^{-1}$ . Shaded region represented the capacitive contribution ( $k_1v$ ) to total charge storage.

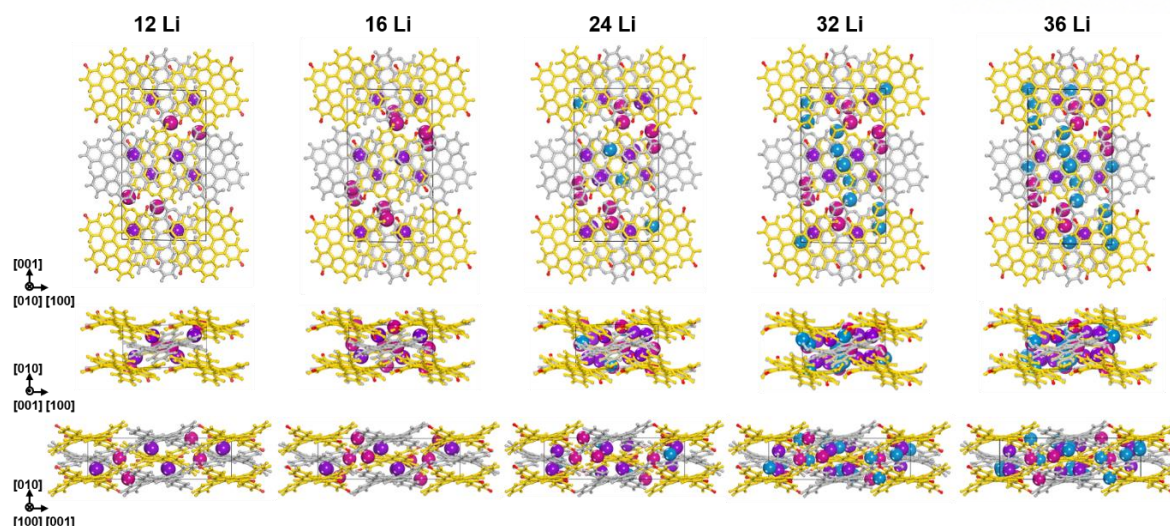


**Figure 2.15** Projection views of  $P2_1/n$  crystal phase of cHBC/F-cHBC solid solution with Li-ions along [010], [001], and [100] directions. cHBC molecules, F-cHBC molecules, Li-ions sandwiched between aromatic rings of cHBC and F-cHBC molecules, Li-ions between the aromatic rings of cHBC molecule and fluorine of F-cHBC molecule, and Li-ions on aromatic rings of cHBC and F-cHBC molecules are shown in gray, yellow, purple, magenta, and blue, respectively. Note that fluorine atoms are colored in red.

Li-ions are intercalated into the vacant sites between the edge aromatic rings of cHBC and F-cHBC molecules denoted as site I (**Figure 2.16a**). These are the most thermodynamically stable sites due to cation- $\pi$  interactions with the sandwiched structure. Next, additional Li-ions are adsorbed on the vacant sites between the edge aromatic ring in the cHBC molecule and fluorine of the F-cHBC molecule, which denoted as site II; due to interactions with the  $\pi$  electrons of aromatic carbon and electronegative fluorine atoms (**Figure 2.16b**). Finally, additional Li-ions are located on the other aromatic rings of cHBC and F-cHBC molecules with relatively large spaces and form cation- $\pi$  interactions denoted as site III (**Figure 2.16c**). Consequently, all 36 Li-ions are adsorbed on the sites that favor cation- $\pi$  interactions, in which 8 Li-ions (22%) are located around the fluorine of F-cHBC molecules (site II). The negative electrostatic potential of fluorine atom can accelerate ion diffusion, which promote fast redox reaction. Thus, we speculate that the contribution ratio of adsorption site II may be the reason for the experimentally observed 30% capacitive behavior (Figure 2.14b). Thus, it is reasonable to suggest that the cHBC/F-cHBC solid solution not only enhances the reversible specific capacity of  $350 \text{ mA h g}^{-1}$ , but also mitigates the specific capacity drop at high current rates.



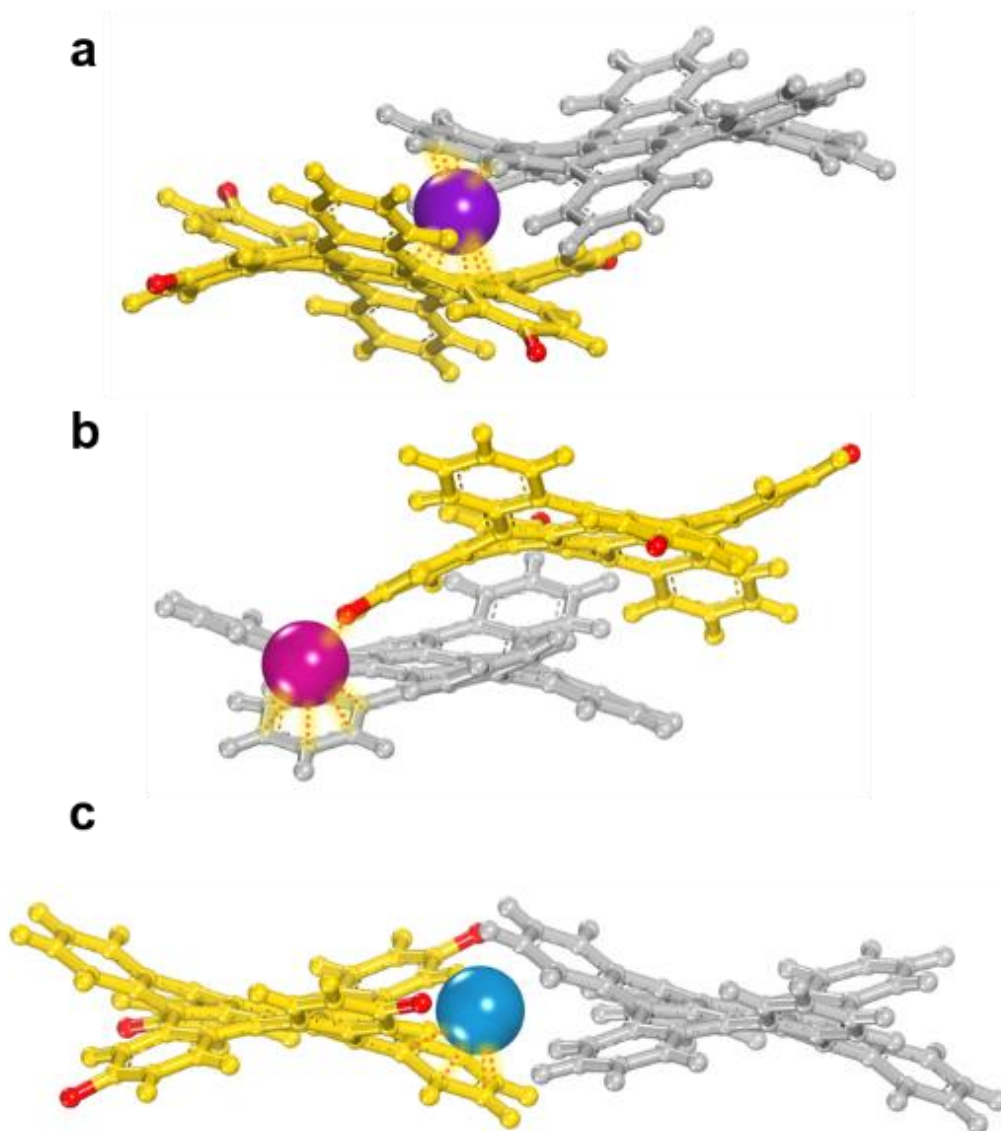


**Figure 2.16** Magnified views of adsorption site of Li-ions in optimized structure of  $P2_1/n$  crystal phase of cHBC/F-cHBC solid solution with Li-ions; (a) Li-ion sandwiched between aromatic rings of cHBC and F-cHBC molecules (site I, purple), (b) Li-ion between the aromatic ring of cHBC and fluorine of F-cHBC (site II, magenta), (c) Li-ion on aromatic ring of F-cHBC molecule (site III, blue). cHBC and F-cHBC molecules are shown in gray and yellow, respectively. Note that fluorine atoms are colored in red. The close contact of Li-ions are represented by orange dotted line.

### 2.3.4 C<sub>60</sub>/cHBC cocrystal

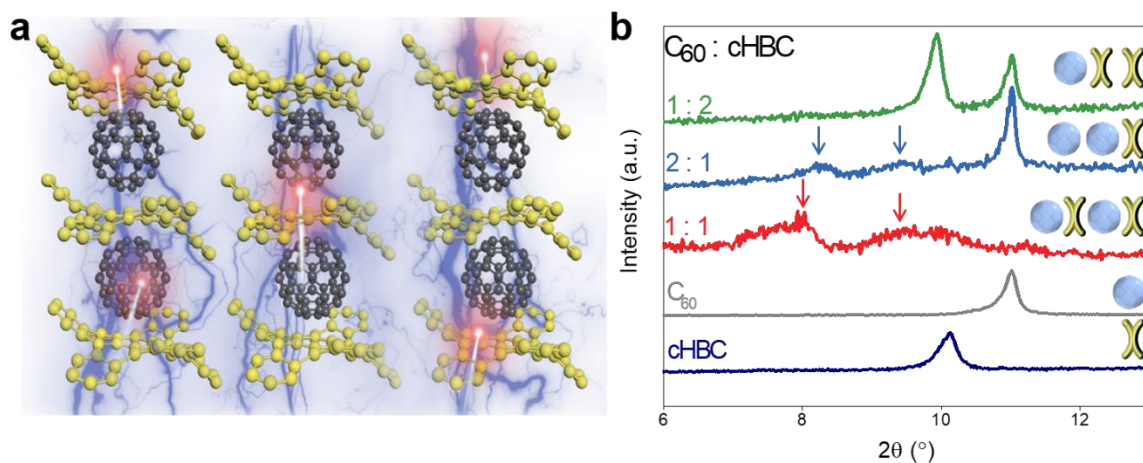


**Figure 2.17** (a) Schematic of electron transfer mechanism in C<sub>60</sub>/cHBC blend electrode, (b) XRD patterns of pristine cHBC, pristine C<sub>60</sub>, C<sub>60</sub>/cHBC = 1:1, 2:1, and 1:2 electrodes.

We hypothesized that cHBC with a concave surface and ball-shaped C<sub>60</sub> molecule form a supramolecular complex (**Figure 2.17a**), leading to the evolution of the molecular level *p-n* junction, which promotes the electron transport [21]. The strong molecular interaction between contorted aromatic compounds and C<sub>60</sub> forms a supramolecular structure in certain blend regions (not shown). The crystalline structures of different electrodes were investigated using the X-ray diffraction (XRD) technique (**Figure 2.17b**). The C<sub>60</sub>/cHBC electrode with a ratio of 1:2 exhibits two distinct diffraction peaks at  $2\theta = 10^\circ$  and  $11^\circ$ , which are the diffraction peaks of pristine cHBC and C<sub>60</sub>, respectively. This result suggests that there is no formation of the C<sub>60</sub>/cHBC cocrystal at this ratio. In contrast, with the blend ratios of 2:1 and 1:1, two broad and weak diffraction peaks at  $2\theta = 8^\circ$  and  $9^\circ$  are observed. These peaks do not correspond to pristine cHBC or pristine C<sub>60</sub> crystals, indicating the formation of the cocrystalline structure. In particular, a very weak diffraction peak at  $2\theta = 11^\circ$  is observed for the C<sub>60</sub>/cHBC electrode with the ratio of 1:1; when the ratio is 2:1, this peak becomes significantly stronger, which is presumably due to the extra C<sub>60</sub> crystals after C<sub>60</sub>/cHBC cocrystal formation. Thus, we conclude that the 1:1 ratio is the optimum stoichiometry for C<sub>60</sub>/cHBC cocrystal formation. Although blend ratio of 1:1 is the optimum stoichiometry for C<sub>60</sub>/cHBC cocrystal formation, the exact crystal structure of C<sub>60</sub>/cHBC complex is still elusive.

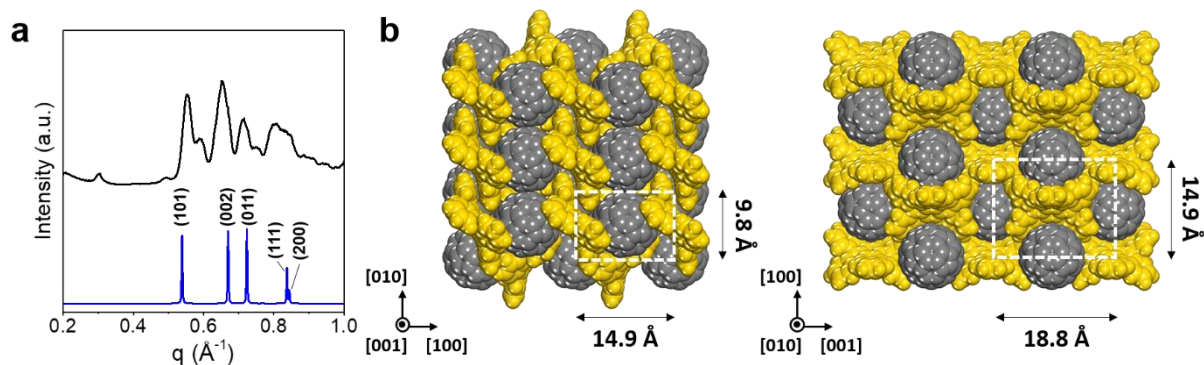


**Figure 2.18** (a) Experimental *in situ* 1D-GIWAXS pattern of  $C_{60}/cHBC=1:1$  film annealed at  $330\text{ }^{\circ}\text{C}$  (black line) and simulated XRD pattern of the orthorhombic Pnnm phase of  $C_{60}/cHBC$  cocrystal (blue line). (b) Projection views of the orthorhombic Pnnm phase of  $C_{60}/cHBC$  cocrystal along [001] and [010] directions. White dashed line represents the lattice of the unit cell.

To reveal the  $C_{60}/cHBC$  cocrystal structure and the arrangement of  $C_{60}$  and cHBC molecules, we performed a computational study by sampling a variety of cocrystal structures using Monte Carlo simulated annealing. The XRD analysis and in-silico screening of the predicted cocrystal structures shows that the experimental grazing-incidence wide-angle X-ray scattering (GIWAXS) pattern is in good agreement with the simulated XRD pattern of the orthorhombic Pnnm phase of  $C_{60}/cHBC$  cocrystal (**Figure 2.18a**). Prominent peaks at  $q \approx 0.539, 0.670, 0.723, 0.837,$  and  $0.844\text{ }\text{\AA}^{-1}$  are assigned to the (101), (002), (011), (111), and (200) planes, respectively. The calculated lattice parameters of the unit cell are  $a = 14.9\text{ }\text{\AA}, b = 9.8\text{ }\text{\AA}, c = 18.8\text{ }\text{\AA}, \alpha = 90.0^{\circ}, \beta = 90.0^{\circ},$  and  $\gamma = 90.0^{\circ}$  (**Figures 2.18b**). In the Pnnm phase of  $C_{60}/cHBC$  cocrystal, each  $C_{60}$  molecule is surrounded by two  $C_{60}$  molecules and six cHBC molecules (**Figure 2.19**). The centroid-to-centroid distances between  $C_{60}$  molecule and cHBC molecule and between two adjacent  $C_{60}$  molecules are  $7.4\text{ }\text{\AA}$  and  $9.8\text{ }\text{\AA}$ , respectively. More interestingly,  $C_{60}$  and cHBC molecules are stacked along the [010] direction to form columnar structures, which are alternatively arranged along the [100] and [001] directions (**Figure 2.20**). This unique arrangement of  $C_{60}$  and cHBC molecules in the  $C_{60}/cHBC$  cocrystal forms molecular level  $p-n$  junctions, which are expected to enhance the charge transport to realize the conducting agent-free Li-ion battery electrode.

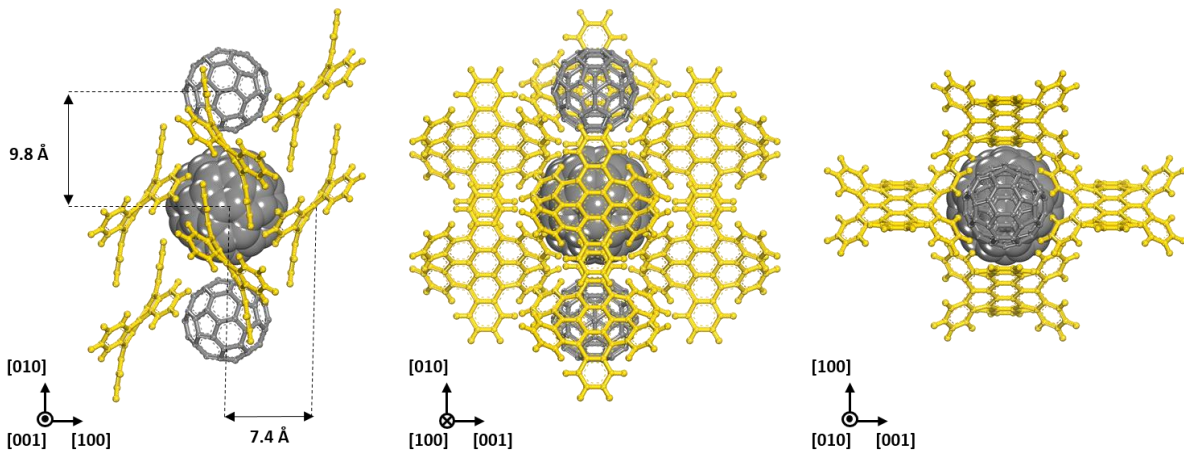


**Figure 2.19** Magnified projection views of the orthorhombic Pnnm phase of C<sub>60</sub>/cHBC cocrystal along [001], [100] and [010] directions. Central single C<sub>60</sub> molecule (space-filling model) and its surrounding molecules (ball and stick model) are only visualized for clarity. C<sub>60</sub> molecules and cHBC molecules are gray and yellow, respectively.

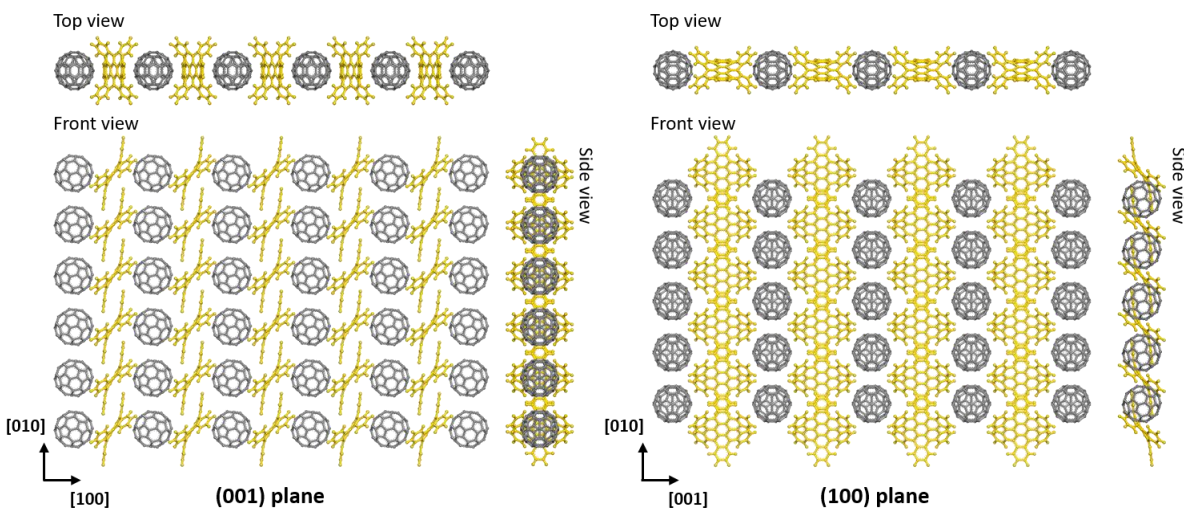


**Figure 2.20** Front, top, and side views of a single sheet of (001) and (100) planes of orthorhombic Pnnm phase of C<sub>60</sub>/cHBC cocrystal. C<sub>60</sub> and cHBC molecules are colored by gray and yellow, respectively.

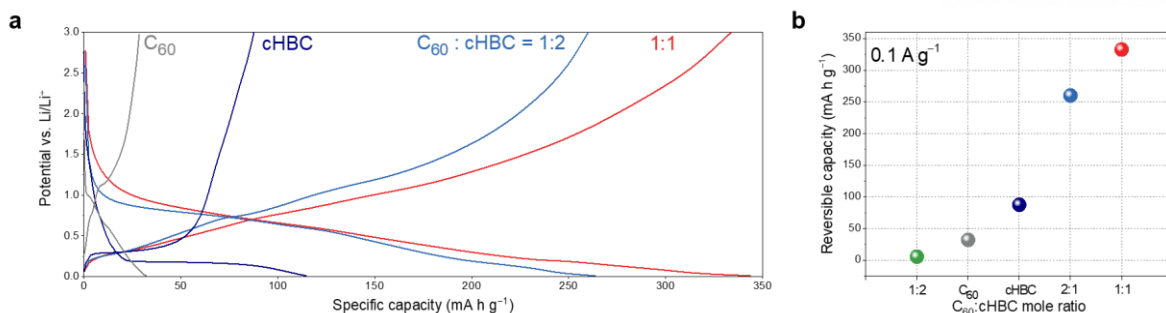


**Figure 2.21** (a) Galvanostatic charge-discharge profiles and (b) corresponding reversible capacity values of pristine C<sub>60</sub>, pristine cHBC, C<sub>60</sub>/cHBC = 1:2, 2:1, and 1:1.

With the well-developed Pnm crystal structure of C<sub>60</sub>/cHBC cocrystal, we performed electrochemical analysis for C<sub>60</sub>/cHBC films with blend ratios of 2:1 and 1:1 in the absence of the conducting agent. A fixed current density of 0.1 A g<sup>-1</sup> was applied with a voltage window of 3.00 – 0.01 V vs. Li/Li<sup>+</sup>. As shown in **Figures 2.21a**, each pristine C<sub>60</sub> and cHBC electrodes without a conducting agent exhibit poor reversible capacity of  $\approx 25$  and 80 mA h g<sup>-1</sup>, respectively. It is noted that the reversible capacity of cHBC was found to be as high as approximately 250 mA h g<sup>-1</sup> when it was mixed with a super P conducting agent (Figure 2.3a). Therefore, the low capacity of 80 mA h g<sup>-1</sup> for pristine cHBC anode can be explained by the limited conductivity of organic semiconducting cHBC molecules. In contrast, the formation of C<sub>60</sub>/cHBC cocrystal without conducting agents significantly increased the reversible capacity: 260 and 330 mA h g<sup>-1</sup> for C<sub>60</sub>/cHBC ratios of 2:1 and 1:1, respectively (**Figure 2.21b**). It reveals that the cocrystal structure efficiently generates more vacant sites for Li-ion storage. Particularly, the specific 1:1 blend ratio is attributed to the molecular level *p-n* junction in the C<sub>60</sub>/cHBC cocrystal to form the columnar structure of C<sub>60</sub>/cHBC to make lower charge transfer resistance during the discharge and charge processes.

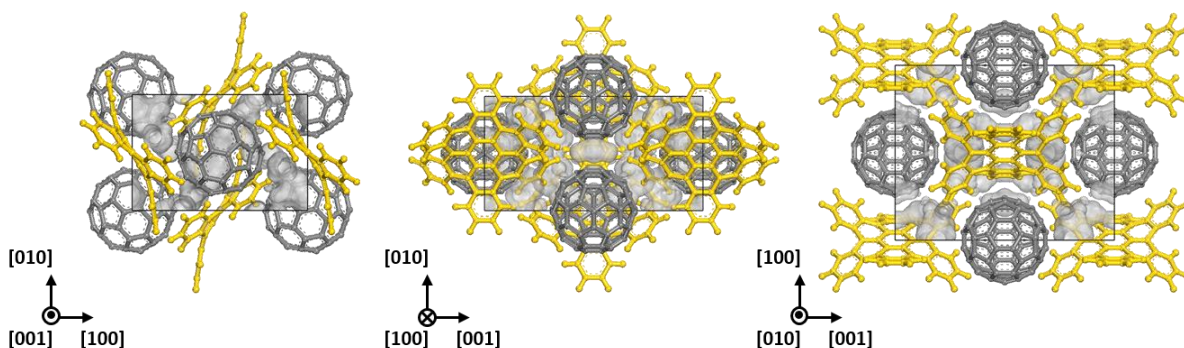


**Figure 2.22** Projection views of Pnm phase of C<sub>60</sub>/cHBC cocrystal with Connolly surface (light gray) along [001], [100] and [010] directions. The space enclosed by the Connolly surface represents the vacant space. C<sub>60</sub> molecules and cHBC molecules are gray and yellow, respectively.

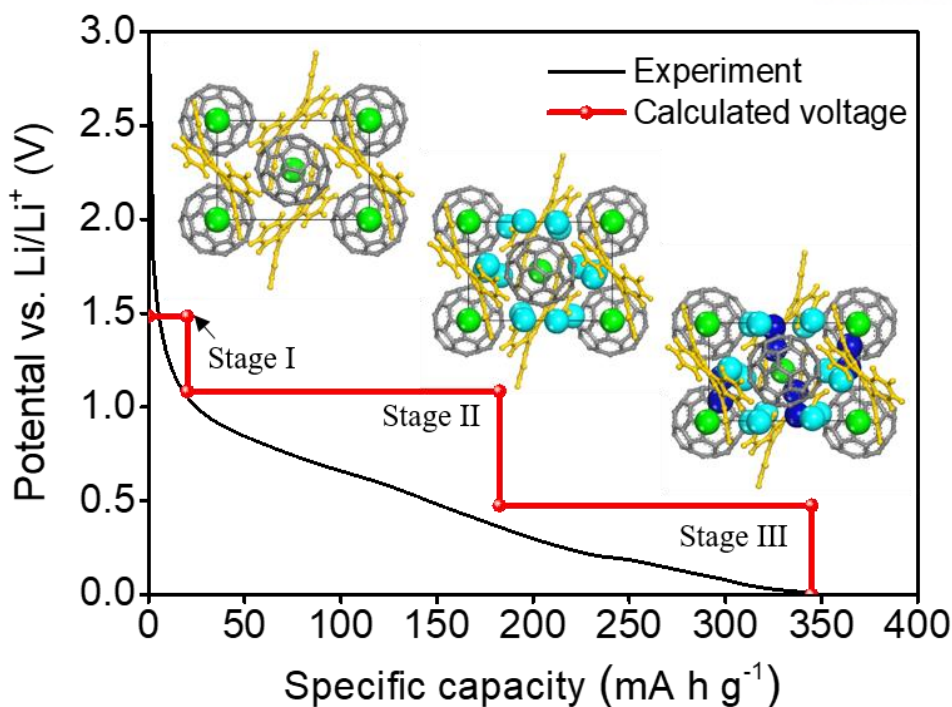


**Figure 2.23** Experimental (black line) and the calculated (red line) voltage profiles. Inset figures represent projection views of the optimized Pnm phase of Li-ion inserted  $C_{60}$ /cHBC cocrystal along [001] direction.

In order to further reveal Li-ion insertion and extraction mechanism of  $C_{60}$ /cHBC cocrystal, we performed Monte Carlo simulations and DFT calculations. Within the unit cell of the Pnm phase of  $C_{60}$ /cHBC cocrystal, the vacant sites for Li-ion insertion are estimated by the Connolly surface method using a probe with a radius of 0.76 Å (**Figure 2.22**). It was found to be the sites between cHBC molecules, the sites between  $C_{60}$  molecules, and the sites between cHBC and  $C_{60}$  molecules. For the identified insertion sites of Li-ion, the calculated voltage profile exhibits three voltage plateaus, representing stages I, II and III, respectively (**Figure 2.23**). The configurations of Li-ion in the Pnm phase of  $C_{60}$ /cHBC cocrystal at each stage are shown in **Figure 2.24**. At stage I, Li-ion preferentially locate at the site between the negatively charged bent edge aromatic rings of two adjacent cHBC molecules as shown **Figure 2.25a**. The average distance between Li-ion and the centroid of the hexagonal aromatic ring is 1.92 Å. The inserted Li-ion interacts with  $\pi$ -electrons of the aromatic carbon (i.e., cation- $\pi$  interaction), which is the strongest noncovalent binding force [48,55]. At stage II, additional Li-ion insert into the sites between pentagonal and hexagonal aromatic rings of adjacent  $C_{60}$  molecules (i.e., sites between  $C_{60}$  molecules) and the sites between the hexagonal aromatic ring of cHBC molecule and the pentagonal or hexagonal aromatic ring of  $C_{60}$  molecule (i.e., sites between  $C_{60}$  and cHBC molecules) (**Figure 2.25b**). Li-ion locate at average distances of 1.95, 1.97, and 2.07 Å from the centroid of hexagonal aromatic ring of cHBC molecule, hexagonal and pentagonal aromatic rings of  $C_{60}$  molecule, respectively. The curvatures of doubly concave cHBC molecules and sphere-like  $C_{60}$

molecules provided spaces, where Li-ion could be intercalated between aromatic rings of  $C_{60}$  and cHBC molecules via cation- $\pi$  interaction. At stage III, the additional Li-ion locate on the top of hexagonal rings of cHBC or  $C_{60}$  molecules (**Figure 2.25c**). Total 34 Li-ion insert into the unit cell of the Pnmn phase of  $C_{60}$ /cHBC cocrystal over the three stages. This result is in good agreement with the experimental capacity (i.e.,  $\approx 344.81 \text{ mA h g}^{-1}$  at the current density of  $0.1 \text{ A g}^{-1}$ ).

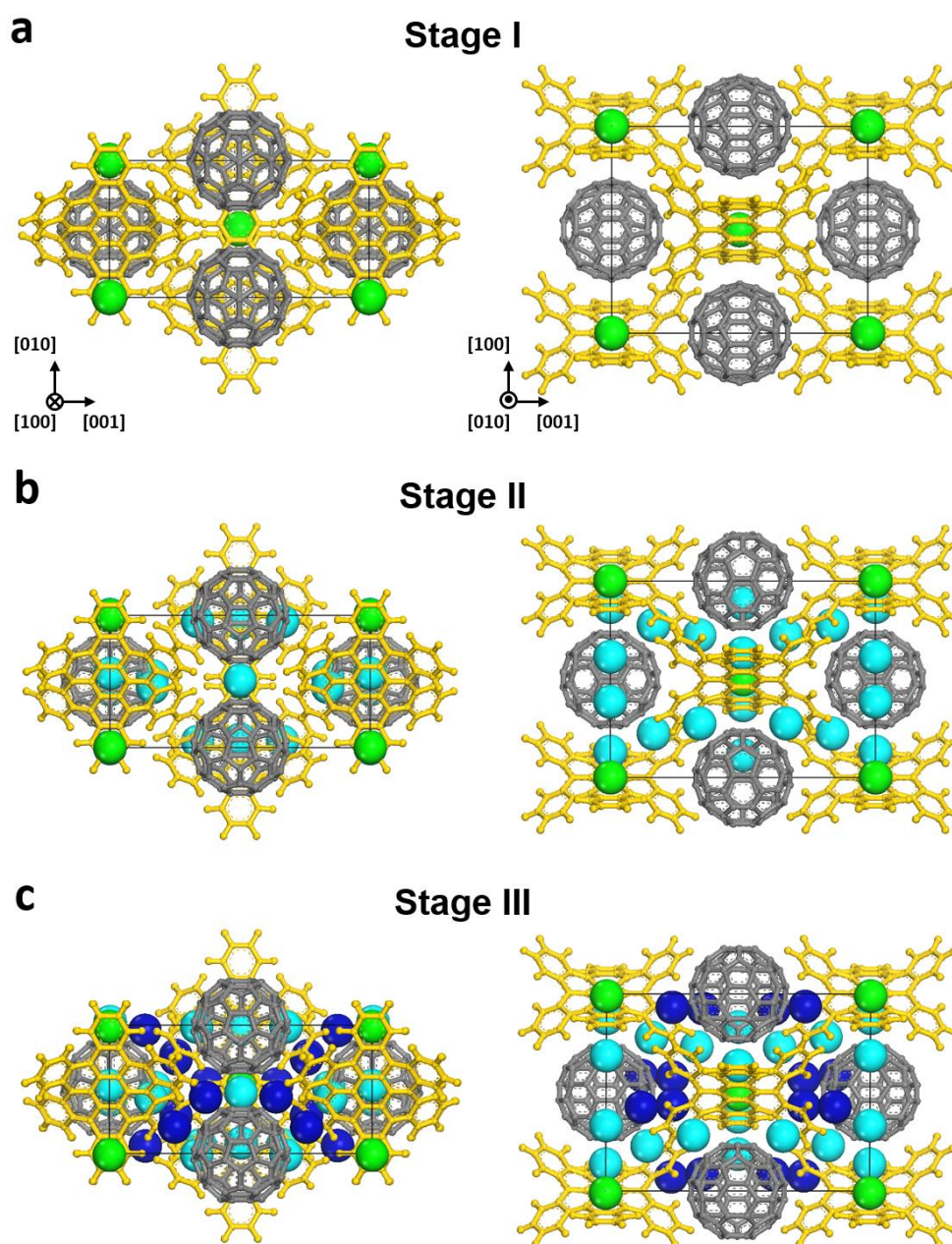


**Figure 2.24** Projection views of Pnmn phase of Li-ion inserted  $C_{60}$ /cHBC cocrystal along [100] and [010] directions; a) stage I, b) stage II, c) stage III.  $C_{60}$  molecules, cHBC molecules, inserted Li-ion at stage I, additionally inserted Li-ion at stage II, and additionally inserted Li-ion at stage III are gray, yellow, green, cyan, and blue, respectively.

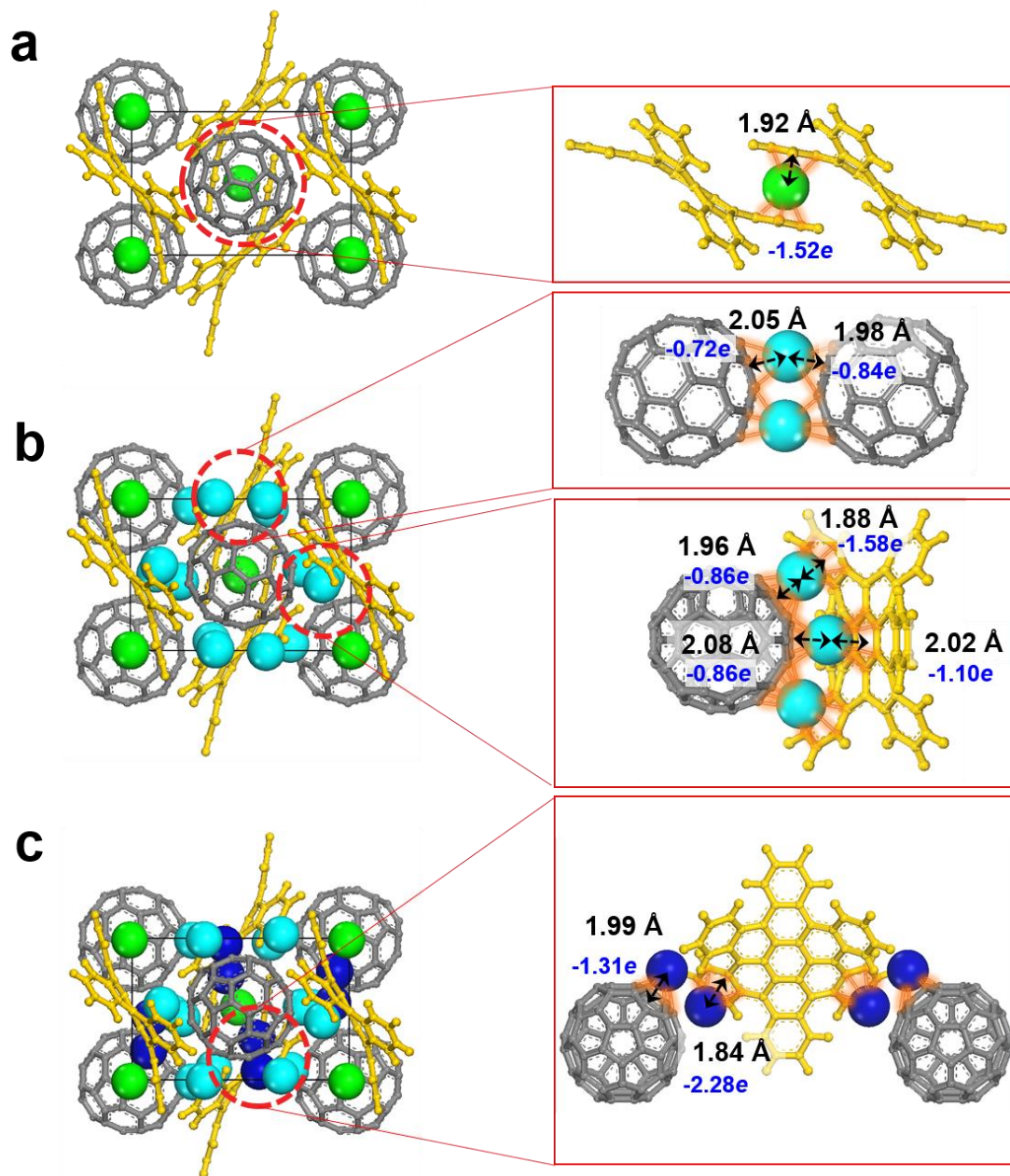


**Figure 2.25** The optimized structure of Pnm phase of Li-ion inserted  $C_{60}$ /cHBC cocrystal at each stage and magnified views of Li-ion insertion site; a) stage I, b) stage II, c) stage III.  $C_{60}$  molecules, cHBC molecules, inserted Li-ion at stage I, additionally inserted Li-ion at stage II, and additionally inserted Li-ion at stage III are gray, yellow, green, cyan, and blue, respectively. The distances between Li-ion and centroid of hexagonal or pentagonal aromatic ring of  $C_{60}$  or cHBC molecules and close contact of Li-ion are black dotted arrow and orange line, respectively. The total charges of carbon of aromatic rings are represented by blue color.



## 2.4 Conclusion

These works demonstrated that a new type of carbon-based contorted molecule could find application as an emerging anode material for use in Li-ion battery systems. The highly crystalline trigonal  $R\bar{3}$  phase of cHBC allowed us to characterize the electrochemical performance using a half-cell structure with Super P as a conducting agent. The reliable performance with long cycle life clearly implies that the contorted molecule provides excellent battery performance without significant alteration. In particular, due to its contorted small molecular shape forming 3D ordering of the pores in the crystal structure, cHBC anode exhibited single-step Li-ion intercalation behavior.

By fluorination of cHBC molecule (F-cHBC), its electrochemical performance is differed as a capacitive behavior. The adsorption of Li-ions is energetically favorable in the empty space between the fluorine atom of the F-cHBC molecule and the negatively charged bent aromatic ring. Owing to the fluorine atoms at the end of each peripheral aromatic ring, the HOMO–LUMO energy levels of cHBC decreased and split, resulting in pseudo-capacitor characteristics. Also, the highly crystalline  $P2_1/c$  phase has the large  $d$  spacing. Based on these properties, F-cHBC anode has the high-rate performance with satisfactory storage capacities of Li-ion.

Through fabricating organic solid solution electrodes, the high-performance Li-ion storage cells can be produced combining with cHBC and F-cHBC molecules. Their molecular and crystal structure similarity enables them to form a homogeneous solid solution with the desired material properties. The resulting crystal phase of the cHBC/F-cHBC solid solution is  $P2_1/n$  symmetry. Combination of the battery behavior of cHBC and capacitive behavior of F-cHBC can be improved the Li-ion storage performance rather than individual pure materials. This approach can offer new opportunities in the field of next-generation carbon-based anodes.

At last, the unique donor-acceptor crystalline structure of semiconducting  $C_{60}$  and cHBC has been developed as a cocrystal that efficiently enhances the electron transfer during discharge and charge processes due to the formation of molecular level  $p$ – $n$  junctions. The orthorhombic  $Pnmm$  phase of  $C_{60}$ /cHBC formed a repeating columnar structure that not only enhances the electron transfer but also produces vacant sites for Li-ion insertion. These results further suggest the new viewpoint of organic semiconducting cocrystal materials for high-performance LIBs anodes.

## 2.5 References

1. J. M. Tarascon and M. Armand, *Nature* **2001**, *414*, 359.
2. V. Etacheri, R. Marom, R. Elazari, G. Salitra, and D. Aurbach, *Energy Environ. Sci.* **2011**, *4*, 3243–3262.
3. J. Billaud, F. Bouville, T. Magrini, C. Villevieille, and A. R. Studart, *Nat. Energy*, **2016**, *1*, 16097.
4. M. S. Whittingham, *Chem. Rev.* **2004**, *104*, 4271–4302.
5. N. Nitta, F. Wu, J. T. Lee and G. Yushin, *Mater. Today* **2015**, *18*, 252–264.
6. P. G. Bruce, S. A. Freunberger, L. J. Hardwick and J.-M. Tarascon, *Nat. Mater.* **2011**, *11*, 19–29.
7. P. Hartmann, C. L. Bender, M. Vračar, A. K. Durr, A. Garsuch, J. Janek and P. Adelhelm, *Nat. Mater.* **2012**, *12*, 228–232.
8. Y. Idota, T. Kubota, A. Matsufuji, Y. Maekawa and T. Miyasaka, *Science* **1997**, *276*, 1395–1397.
9. H. Li, P. Balaya and J. Maier, *J. Electrochem. Soc.* **2004**, *151*, A1878–A1885.
10. N. A. Kaskhedikar and J. Maier, *Adv. Mater.* **2009**, *21*, 2664–2680.
11. E. Yoo, J. Kim, E. Hosono, H.-s. Zhou, T. Kudo and I. Honma, *Nano Lett.*, **2008**, *8*, 2277–2282.
12. C. Masarapu, V. Subramanian, H. Zhu and B. Wei, *Adv. Funct. Mater.* **2009**, *19*, 1008–1014.
13. J. R. Dahn, T. Zheng, Y. Liu and J. S. Xue, *Science* **1995**, *270*, 590–593.
14. Z.-S. Wu, W. Ren, L. Xu, F. Li and H.-M. Cheng, *ACS Nano* **2011**, *5*, 5463–5471.
15. X. Zhou, L.-J. Wan and Y.-G. Guo, *Adv. Mater.* **2013**, *25*, 2152–2157.
16. C. Zhang, N. Mahmood, H. Yin, F. Liu and Y. Hou, *Adv. Mater.* **2013**, *25*, 4932–4937.
17. I.-Y. Jeon, M. J. Ju, J. Xu, H.-J. Choi, J.-M. Seo, M.-J. Kim, I. T. Choi, H. M. Kim, J. C. Kim, J.-J. Lee, H. K. Liu, H. K. Kim, S. Dou, L. Dai and J.-B. Baek, *Adv. Funct. Mater.* **2015**, *25*, 1170–1179.
18. S. Xiao, M. Myers, Q. Miao, S. Sanaur, K. Pang, M. L. Steigerwald and C. Nuckolls, *Angew. Chem., Int. Ed.* **2005**, *44*, 7390–7394.
19. A. M. Hiszpanski, R. M. Baur, B. Kim, N. J. Tremblay, C. Nuckolls, A. R. Woll and Y.-L. Loo, *J. Am. Chem. Soc.* **2014**, *136*, 15749–15756.
20. M. Ball, Y. Zhong, Y. Wu, C. Schenck, F. Ng, M. Steigerwald, S. Xiao and C. Nuckolls, *Acc. Chem. Res.* **2015**, *48*, 267–276.
21. N. J. Tremblay, A. A. Gorodetsky, M. P. Cox, T. Schiros, B. Kim, R. Steiner, Z. Bullard, A. Sattler, W.-Y. So, Y. Itoh, M. F. Toney, H. Ogasawara, A. P. Ramirez, I. Kymissis, M. L. Steigerwald and C. Nuckolls, *ChemPhysChem* **2010**, *11*, 799–803.

22. S. Xiao, S. J. Kang, Y. Zhong, S. Zhang, A. M. Scott, A. Moscatelli, N. J. Turro, M. L. Steigerwald, H. Li, and C. Nuckolls, *Angew. Chem. Int. Ed.* **2013**, *52*, 4558–4562.
23. S. Xiao, S. J. Kang, Y. Wu, S. Ahn, J. B. Kim, Y.-L. Loo, T. Siegrist, M. L. Steigerwald, H. Li, and C. Nuckolls, *Chem. Sci.* **2013**, *4*, 2018–2023.
24. A. M. Hiszpanski, J. D. Saathoff, L. Shaw, H. Wang, L. Kraya, F. Lüttich, M. A. Brady, M. L. Chabinyk, A. Kahn, P. Clancy, and Y.-L. Loo, *Chem. Mater.* **2015**, *27*, 1892–1900.
25. J. Zhang, W. Xu, P. Sheng, G. Zhao, and D. Zhu, *Acc. Chem. Res.* **2017**, *50*, 1654–1662.
26. T. Nokami, T. Matsuo, Y. Inatomi, N. Hojo, T. Tsukagoshi, H. Yoshizawa, A. Shimizu, H. Kuramoto, K. Komae, H. Tsuyama, and J.-i Yoshida, *J. Am. Chem. Soc.* **2012**, *134*, 19694–19700.
27. X. Han, C. Chang, L. Yuan, T. Sun, and J. Sun, *Adv. Mater.* **2007**, *19*, 1616–1621.
28. C. Luo, R. Huang, R. Kevorkyants, M. Pavanello, H. He, and C. Wang, *Nano Lett.* **2014**, *14*, 1596–1602.
29. W. Walker, S. Grugeon, O. Mentre, S. Laruelle, J.-M. Tarascon, and F. Wudi, *J. Am. Chem. Soc.* **2010**, *132*, 6517–6523.
30. M. Armand, S. Grugeon, H. Vezin, S. Laruelle, P. Ribière, P. Poizot, and J.-M. Tarascon, *Nat. Mater.* **2009**, *8*, 120–125.
31. H. H. Lee, Y. Park, S. H. Kim, S.-H. Yeon, S. K. Kwak, K. T. Lee, and S. Y. Hong, *Adv. Mater.* **2015**, *25*, 4859–4866.
32. BIOVIA, Dassault Systèmes, Materials Studio 2019. San Diego: Dassault Systèmes, **2019**.
33. H. Sun, Z. Jin, C. Yang, R. L. Akkermans, S. H. Robertson, N. A. Spenley, S. Miller, and S. M. Todd, *J. Mol. Model* **2016**, *22*, 47.
34. P. P. Ewald, *Annalen der Physik*, **1921**, *369*, 253–287.
35. M. P. Tosi, in *Solid State Physics*, eds. F. Seitz and D. Turnbull, Academic Press, **1964**, *16*, 1–120.
36. R. S. Mulliken, *J. Chem. Phys.* **1955**, *23*, 1833–1840.
37. S. J. Clark, M. D. Segall, C. J. Pickard, P. J. Hasnip, M. I. Probert, K. Refson, and M. C. Payne, *Z.Kristallogr.* **2004**, *220*, 567–570.
38. J. P. Perdew, K. Burke, and M. Ernzerhof, *Phys. Rev. Lett.* **1996**, *77*, 3865–3868.
39. S. Grimme, *J. Comput. Chem.* **2006**, *27*, 1787–1799.
40. Monkhorst, H. J. and Pack, J. D. *Phys. Rev. B* **1976**, *13*, 5188–5192.
41. B. Delley, *J. Chem. Phys.* **2000**, *113*, 7756–7764.
42. B. Delley, *J. Chem. Phys.* **1990**, *92*, 508–517.
43. A. D. Becke, *J. Chem. Phys.* **1993**, *98*, 5648–5652.
44. P. J. Stephens, F. J. Devlin, C. F. Chabalowski and M. J. Frisch, *J. Phys. Chem.* **1994**, *98*, 11623–11627.

45. A. M. Hiszpanski, A. R. Woll, B. Kim, C. Nuckolls, and Y.-L. Loo, *Chem. Mater.* **2017**, *29*, 4311–4316.
46. V. Augustyn, P. Simon, and B. Dunn, *Energy Environ. Sci.* **2014**, *7*, 1597–1614.
47. H. Lindström, S. Södergren, A. Solbrand, H. Rensmo, J. Hjelm, A. Hagfeldt, S.-E. and Lindquist, *J. Phys. Chem. B* **1997**, *101*, 7717–7722.
48. P. Yu, C. Li, and X. Guo, *J. Phys. Chem. C* **2014**, *118*, 10616–10624.
49. M. Winter, J. O. Besenhard, M. E. Spahr, and P. Novák, *Adv. Mater.* **1998**, *10*, 725–763.
50. J. Xie, and Q. Zhang, *J. Mater. Chem. A* **2016**, *4*, 7091–7106.
51. Z. Song, and H. Zhou, *Energy Environ. Sci.* **2013**, *6*, 2280–2301.
52. M. Lusi, *Cryst. Growth Des.* **2018**, *18*, 3704–3712.
53. T. Yamashita, H. Momida and T. Oguchi, *J. Phys. Soc. Jpn.* **2015**, *84*, 074703.
54. M. Lee, J. Hong, J. Lopez, Y. Sun, D. Feng, K. Lim, W. C. Chueh, M. F. Toney, Y. Cui and Z. Bao, *Nat. Energy* **2017**, *2*, 861–868.
55. J. C. Ma, and D. A. Dougherty, *Chem. Rev.* **1997**, *97*, 1303–1324.

## Chapter 3. Solvent Engineering of Perovskite Granular Wire with High Photodetectivity

*This chapter includes the published contents:*

Yoon Ho Lee†, Inho Song†, Su Hwan Kim, Ju Hyun Park, Sung O Park, Jeong Hun Lee, Yousang Won, Kilwon Cho, Sang Kyu Kwak\*, and Joon Hak Oh\*, “Perovskite Granular Wire Photodetectors with Ultrahigh Photodetectivity” *Advanced Materials*, 32(32), 2002357, **2020**.

Reprinted with permission. Copyright © 2020 WILEY-VCH Verlag GmbH & Co. KGaA, Weinheim

---

### 3.1 Introduction

Methylammonium lead halide ( $\text{CH}_3\text{NH}_3\text{PbX}_3$ , X = halogen) perovskite materials have attracted a great deal of interest for their diverse optoelectronic applications, including solar cells [1,2], photosensors [3], lasers [4], and light-emitting diodes [5], because of their suitable direct bandgap with large absorption coefficients and minimal of trapping states, and their excellent transport properties. Nevertheless, the majority of studies on perovskite have focused on increase crystallinity and grain size, which can minimize the trap states from defect sites [6,7]. In terms of the energy bands, conduction and valance band edges are flat along the axial direction, thus providing a fast track for carrier transport when an external electric field is applied. This tends to yield high photocurrents, but inevitably results in high dark current due to the intrinsic carrier concentration, which often limits device performances, such as noise equivalent power (NEP), specific detectivity ( $D^*$ ), and linear dynamic range (LDR). Therefore, one grand challenge for perovskite photosensor is to develop high-performance perovskite photosensors with high photocurrent and low dark current by inducing appropriately optimized trap states through control over morphology and crystallinity of perovskite materials. The elucidation of the morphology-dependent photoconductive performance may have consequences for the development of more efficient devices.

To finetuning the morphology of perovskite materials, solvent engineering is effectively applied. Depending on solvent types, crystallization pathway including nucleation and growth can be controlled. Under consideration of solvent effects, crystal phase, morphology, surface characteristics, grain size, and crystallinity can be different. Wakamiya et al. reported that the crystal structure obtained after cooling supersaturated  $\text{PbI}_2$  solution in dimethylformamide (DMF) solvent was proved to be  $\text{PbI}_2\cdot\text{DMF}$  intermediate phase based on XRD analysis [8]. Since  $\text{PbI}_2\cdot\text{DMF}$  intermediate structure is coordinated along the 1D direction, we can predict the wire shape of  $\text{PbI}_2\cdot\text{DMF}$  crystal was formed. Thus, the

pathway from precursor to perovskite formation in solution environment is important to identify the structure of the intermediate phase. Especially, the granular wires formed by 1D arrangement of nanoparticles have great potential for achieving high  $D^*$  due to the highly suppressed dark current originating from the unique band-edge modulation due to their morphological factors [9]. However, only few studies of granular wires have been reported, and most of these studies are related to template synthesis [10-12] and direct ink-jet printing synthesis [9], due to the difficulty of aggregating nanoparticles predominantly in the 1D direction for the formation of granular wires.

Here, we report the synthesis of  $\text{CH}_3\text{NH}_3\text{PbI}_3$  based perovskite granular wires (PGWs) via a simple and cost-effective template-free solution process for the first time and their use in flexible high-performance photosensor arrays. These PGWs exhibited a  $D^*$  of  $3.17 \times 10^{15}$  Jones, which is the highest reported value among perovskite materials to date. This high performance is resulting from the granular wire morphology with grain boundaries, which are highly beneficial to a largely suppressed dark current by modulating energy band edge along the axial direction of the PGWs. These observations will facilitate the rational design of high-performance photosensors. Our results clearly show that solution processed PGWs are highly promising materials for the construction of high-performance photosensors, which can also be extended for use in other optoelectronic applications.

## 3.2 Computational details

### 3.2.1 Growth morphology

The growth morphology of our  $\text{PbI}_2\cdot\text{DMF}$  granular wires (PDGWs) was evaluated using the attachment energy model [13], which can predict the crystal shape calculating the relative growth rates of its various faces. Attachment energy ( $\Delta E_{\text{att}}$ ) is defined as the energy released per growth unit when a surface layer of one interplanar thickness ( $d_{hkl}$ ) is added on the corresponding crystal surface and can be defined as follows:

$$\Delta E_{\text{att}} = E_{\text{latt}} - E_{\text{slice}}$$

where  $E_{\text{latt}}$  is the lattice energy of the crystal, and  $E_{\text{slice}}$  is the energy of a growth slice of  $d_{hkl}$ . The relative growth rate of a crystal surface ( $R_{hkl}$ ) is proportional to the absolute value of the attachment energy as:

$$R_{hkl} \propto |E_{\text{att}}|$$

This method implies that when the attachment energy of an ( $hkl$ ) crystal surface is relatively weak (strong), growth rate and exposed area become slower (faster) and larger (smaller), respectively.

### 3.2.2 Forcefield parameterization

For molecular dynamics (MD) simulations, we developed forcefield parameters to describe the structural and elastic properties of  $\text{PbI}_2\cdot\text{DMF}$  crystal.  $\text{PbI}_2\cdot\text{DMF}$  crystal consist of an organic (i.e., DMF) and inorganic (i.e.,  $\text{PbI}_2$ ) framework. The parameters and partial charges of DMF molecules were acquired from the General AMBER Forcefield,[14] which is widely used for organic molecules.[15] We used parameters developed by Handley and Freeman [16] to describe the chemical potential of  $\text{PbI}_2$ . It is noted that the partial charges of Pb and I atoms were 1.263  $e$  and -0.6315  $e$ , respectively. Lennard-Jones (12–6) potentials were fitted to describe the interactions between DMF molecules and  $\text{PbI}_2$  in the  $\text{PbI}_2\cdot\text{DMF}$  crystal. In particular, potentials were parameterized until the structural and elastic properties, i.e., the lattice parameters and Young's modulus, of the  $\text{PbI}_2\cdot\text{DMF}$  crystal were optimized to be comparable to those determined by DFT calculations (see Young's modulus calculations below). The obtained forcefield parameters of the  $\text{PbI}_2\cdot\text{DMF}$  crystal are shown in **Table 3.1**. The lattice parameters and Young's modulus of  $\text{PbI}_2\cdot\text{DMF}$  crystal, optimized by fitted forcefield parameters and DFT calculations, are compared in **Table 3.2**. In addition, we confirmed that our simulated XRD data were comparable to experimental one (**Figure 3.1**).

**Table 3.1** Potential parameters for PbI<sub>2</sub>·DMF crystal. C3 and C indicate the carbon atom of alkyl group and amide group, respectively, while H1 and H5 indicate hydrogen atom of alkyl group and amide group, respectively.

Buckingham potentials ( $E = A \exp(-bR) - C_6/R^6$ )				
		A (kcal/mol)	C <sub>6</sub> (kcal/mol/Å <sup>2</sup> )	b (kcal/mol)
Pb	Pb	39279.1	25371.48	3.508
Pb	I	158572.0	25371.48	3.0895
I	I	41320.93	10838.67	2.158475
Lennard-Jones 12-6 potential ( $E = D_0[(R_0/R)^{12} - 2(R_0/R)^6]$ )				
		D <sub>0</sub> (kcal/mol)	R <sub>0</sub> (Å)	
Pb		0.975	3.95	
I		0.71	4.54	
C		0.085998296	3.81442974	
C3		0.109397928	3.81442974	
H1		0.015699689	2.7728547	
H5		0.014999703	2.71687812	
N		0.169996631	3.6465	
O		0.209995839	3.32103024	

**Table 3.2** Comparison of lattice parameters and Young's modulus obtained by DFT and fitted forcefield based calculations. Data are provided for the  $x$ (Y<sub>x</sub>),  $y$ (Y<sub>y</sub>), and  $z$ (Y<sub>z</sub>) directions of PbI<sub>2</sub>·DMF crystal optimized by DFT and fitted forcefield calculations.

	Density (g/cm <sup>3</sup> )	a (Å)	b (Å)	c (Å)	β (°)	Y <sub>x</sub> (GPa)	Y <sub>y</sub> (GPa)	Y <sub>z</sub> (GPa)
DFT	3.641	4.557	18.519	11.550	91.872	15.851	13.645	10.570
Forcefield	3.688	4.509	18.837	11.328	91.415	16.218	14.654	9.726
Error (%)	1.282	1.056	1.721	1.924	0.497	2.318	7.398	7.991



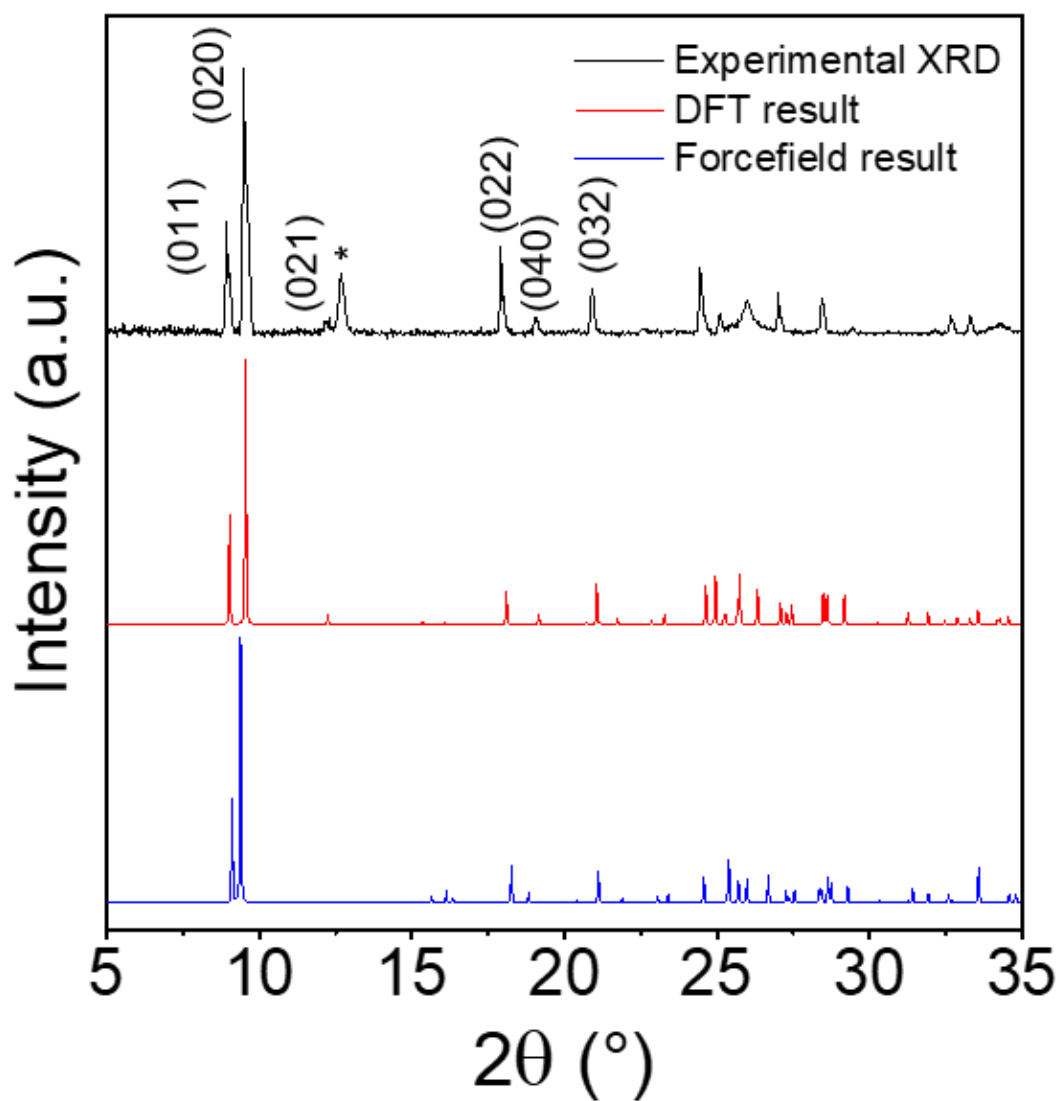


**Figure 3.1** XRD data from experiment, DFT and MD simulations. XRD data are shown for  $\text{PbI}_2 \cdot \text{DMF}$  crystal: experimental (black), DFT calculations (red), and fitted forcefield based optimization (blue).

### 3.2.3 Molecular dynamics (MD) simulation

All MD simulations were carried out within the canonical ( $NVT$ ) ensemble, where  $N$  is the number of molecules,  $V$  is the volume, and  $T$  is the temperature. A Nosé-Hoover-Langevin thermostat [17] was used to maintain the temperature constant at 298 K. The cut off distance of van der Waals interaction was set to 12.5 Å, and the electrostatic interactions were calculated by the Ewald summation method [18,19] with an accuracy of  $10^{-3}$  kcal/mol. The time step was set to be 1 fs and each  $NVT$  MD simulation was performed at least 500 ps to equilibrate the total energy of the system. Additional 500 ps of simulation were performed to calculate the binding energy. The binding energy ( $E_{\text{binding}}$ ) per unit area was calculated as follows:

$$E_{\text{binding}} = \frac{E_{\text{tot}} - E_{\text{slab1}} - E_{\text{slab2}}}{A_{\text{interface}}}$$

where  $E_{\text{tot}}$  is the non-bonding energy of interface between *slab1* and *slab2* system.  $E_{\text{slab1}}$  and  $E_{\text{slab2}}$  are the non-bonding energies of *slab1* and *slab2* systems, respectively, and  $A_{\text{interface}}$  is the contact interfacial area.

### 3.2.4 Young's modulus calculation

DFT calculations, including the effects of spin polarization, were performed in CASTEP [20] to investigate the Young's modulus of  $\text{PbI}_2 \cdot \text{DMF}$  crystal. A generalized gradient approximation with the Perdew-Burcke-Ernzerhof (GGA-PBE) functional [21] was used to describe the exchange correlation potentials of electrons, while electron-ion interactions were represented by on-the-fly generated ultrasoft pseudopotentials with an energy cutoff of 571.4 eV. A Tkatchenko-Scheffler approach was implemented to correct the van der Waals interactions.[22] The criterion of SCF tolerance was set to  $1.0 \times 10^{-6}$  eV/atom. The Brillouin-zone was sampled by a  $3 \times 1 \times 1$  Monkhorst-Pack  $k$ -point grid.[23] The atomic positions and lattice parameters of the  $\text{PbI}_2 \cdot \text{DMF}$  crystal (space group  $\text{P2}_1/\text{n}$ ) were fully relaxed using the BFGS algorithm until the convergence criteria for energies, maximum forces, maximum stress, and maximum displacements satisfied  $1.0 \times 10^{-5}$  eV/atom, 0.03 eV/Å, 0.05 GPa, and 0.001 Å, respectively. Subsequently, elastic constants were calculated by setting the number of steps for each strain and the maximum strain amplitude to 6 and 0.005, respectively.

### 3.3 Results and Discussion

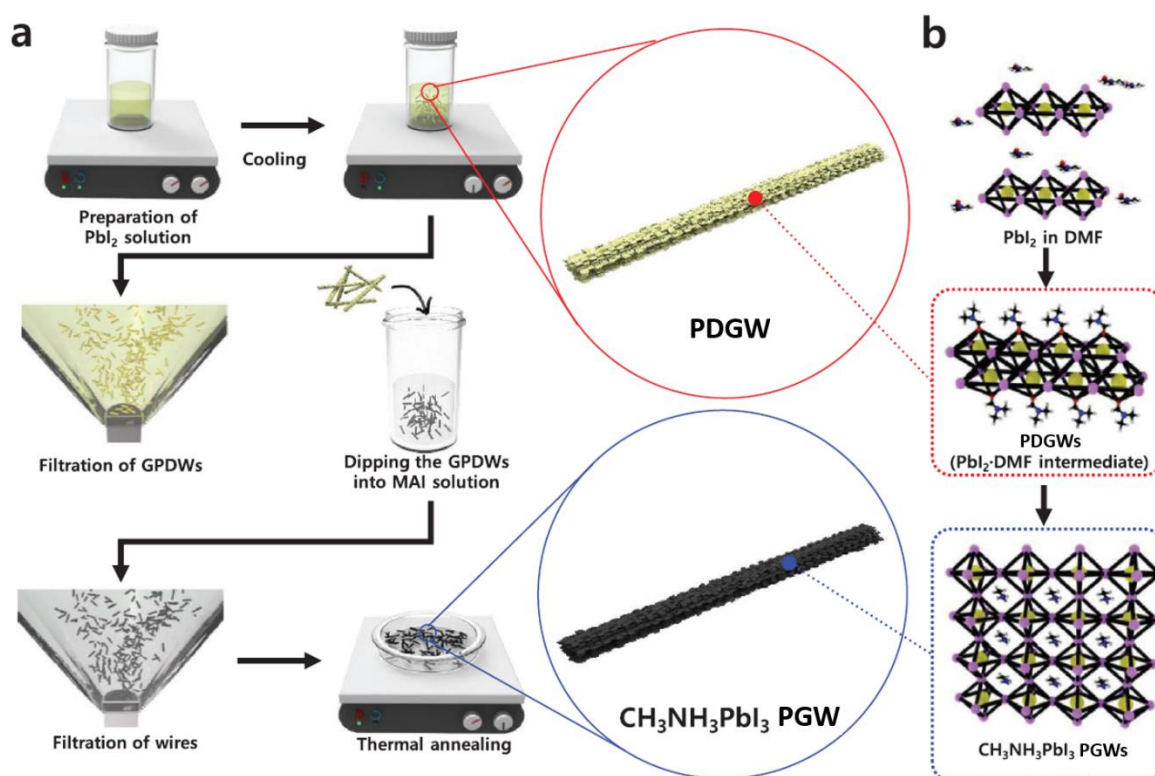


**Figure 3.2** Schematic images of the (a) synthesis process for PGWs and (b) crystal structure corresponding to each experiment process.

PGWs were synthesized using a template-free two-step method consisting of the fabrication of  $PbI_2 \cdot DMF$  granular wires (PDGWs) and dipping them into a solution of methylammonium iodide (MAI). **Figure 3.2** illustrates PGW synthesis and crystal structures corresponding to each step in the process. First, a saturated solution of  $PbI_2$  was prepared in DMF at 180 °C and cooled to room temperature for 48 h to obtain PDGWs by precipitation. The PDGWs were filtered using a conventional vacuum assisted method and dipped into MAI solution for 30 min. The resulting PGWs were filtered and heated at 130 °C for 10 min. To determine the crystal structure of each material, we compared XRD patterns of PDGWs,  $PbI_2$  GWs, and PGWs (**Figure 3.3a**). As already represented in Figure 3.1, the XRD pattern of PDGWs was consistent with a simulated diffractogram of  $PbI_2 \cdot DMF$  crystals, in which DMF is coordinated to  $PbI_2$  (**Figure 3.3b**). The primary diffraction peaks at 8.9° and 9.5° correspond to the (011) and (020) lattice planes, respectively. After annealing process up to 400 °C, DMF molecules were removed and formed  $PbI_2$  GWs, which is identified as (001) and (002) lattice planes in XRD pattern.

To examine the directionality of the PDGWs growth, the role of the solvent in granular wire formation

was investigated by changing the solvent in **Figure 3.4**. In an open system for fast precipitation by solvent evaporation, the same protocol was repeated by replacing DMF by  $\gamma$ -butyrolactone (GBL), another commonly used solvent of organo-lead halide perovskites. The optical microscopy (OM) images of  $\text{PbI}_2$ -based crystals extracted from DMF and GBL solutions were shown in Figure 3.4b and c, respectively.  $\text{PbI}_2$ -DMF crystals extracted from DMF exhibited directional anisotropic growth, while  $\text{PbI}_2$  crystals from GBL did not show directional growth. Unlike  $\text{PbI}_2$ -DMF crystals, crystals extracted from GBL showed only peaks corresponding to pure  $\text{PbI}_2$  in their XRD pattern. This indicates that the type of solvent greatly influences the composition of  $\text{PbI}_2$ -based crystals and the resulting growth direction. Furthermore, the precipitation conditions also play a key role in granular-shaped  $\text{PbI}_2$ -DMF growth. In the closed system, the evaporation of the solvent was insignificant, resulting in slow precipitation compared to the open system where rapid precipitation occurs due to subsequent evaporation of the solvent. Figure 3.4d and e showed OM images of extracted  $\text{PbI}_2$ -DMF and  $\text{PbI}_2$  crystals in the closed systems using DMF and GBL, respectively. Interestingly, granular-shaped  $\text{PbI}_2$ -DMF wires were observed only in the closed system with DMF solvent. By contrast,  $\text{PbI}_2$  crystals extracted from GBL were randomly aggregated without any defined orientation. Therefore, we can predict that the use of DMF and the slow precipitation of  $\text{PbI}_2$ -DMF in solution were the key steps for uniaxial growth, therefore suggesting the important role of DMF as a growth-directing agent.

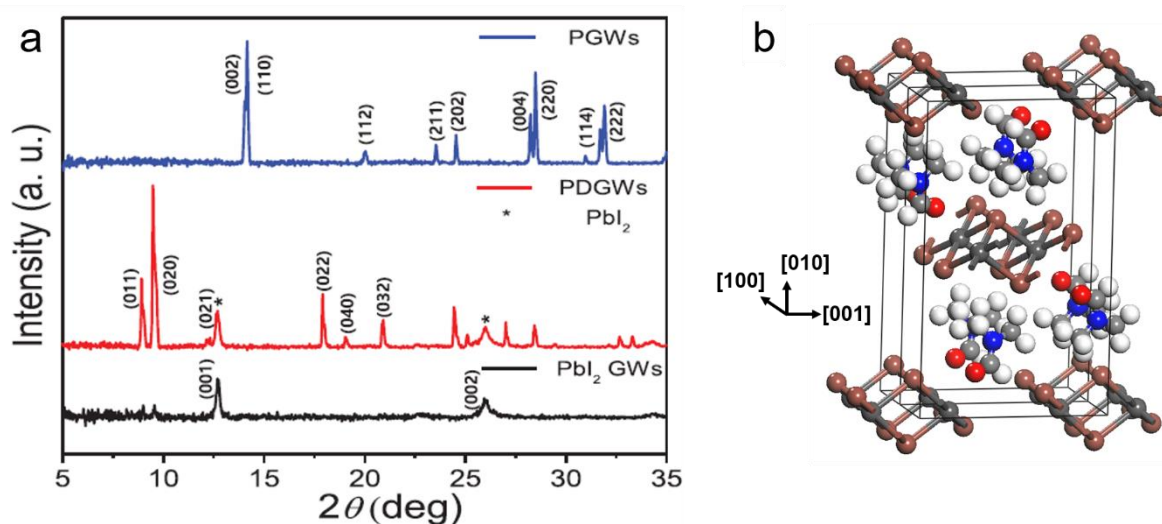


**Figure 3.3** (a) XRD patterns of PDGWs,  $\text{PbI}_2$  GWs, and PGWs. (b) Crystal structure of  $\text{PbI}_2$ ·DMF. Pb, I, C, N, O and H atom are dark grey, brown, grey, blue, red and white color, respectively.

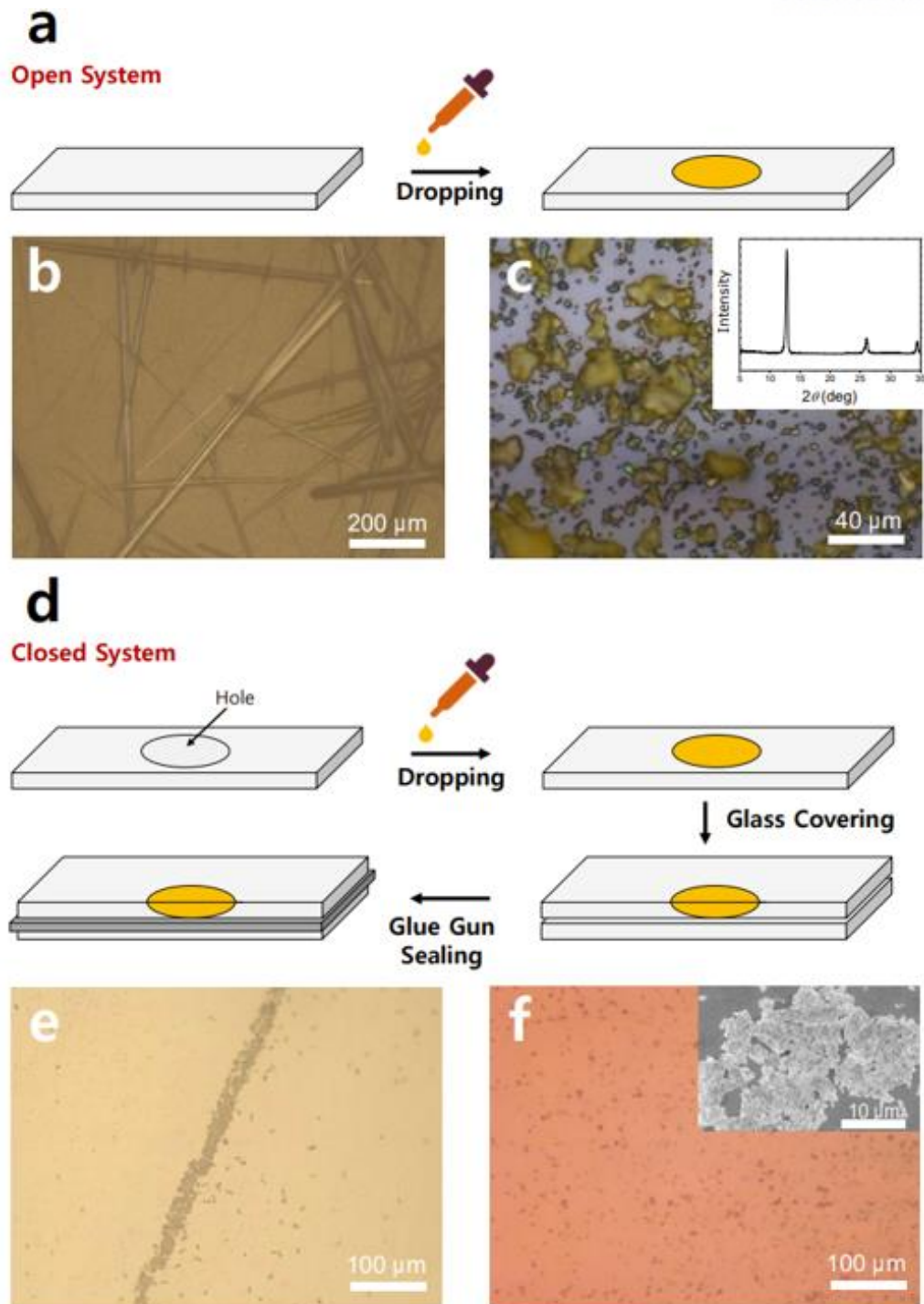


**Figure 3.4** (a) Schematic images of the precipitation process of  $\text{PbI}_2$  solution based on DMF and GBL solvent in the open system. Optical microscopy images of extracted (b)  $\text{PbI}_2 \cdot \text{DMF}$  from DMF solvent-based solution and (c)  $\text{PbI}_2$  from GBL solvent-based solution in the open system (inset: XRD patterns of  $\text{PbI}_2$  from GBL solvent-based solution). (d) Schematic images of the precipitation process of  $\text{PbI}_2$  solution based on DMF and GBL solvent in the closed system. Optical microscopy images of extracted (e)  $\text{PbI}_2 \cdot \text{DMF}$  from DMF solvent-based solution and (f)  $\text{PbI}_2$  from GBL solvent-based solution in the open system (inset: SEM image of randomly aggregated  $\text{PbI}_2$  particles extracted in GBL).

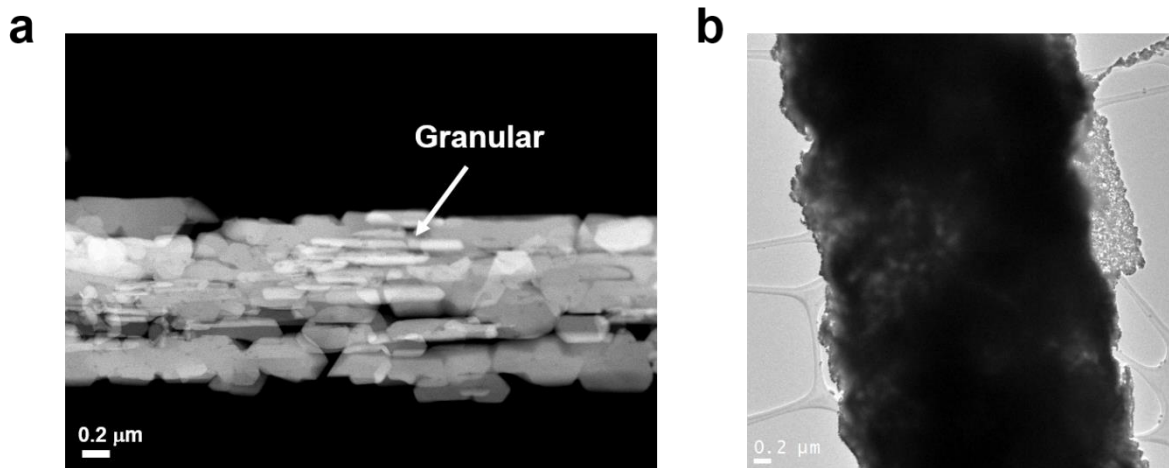


**Figure 3.5** Transmission electron microscopy (TEM) images of (a) PDGW and (b) PGW.

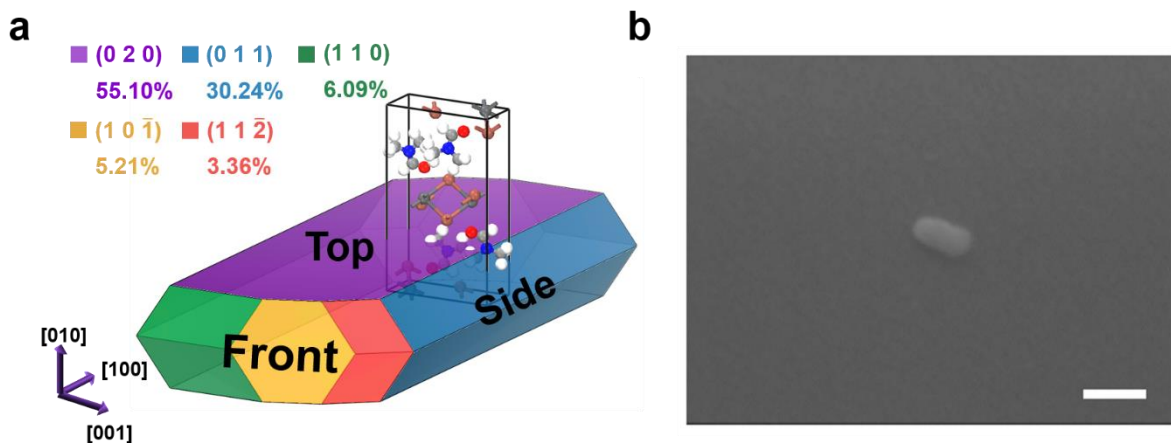


**Figure 3.6** (a) Growth morphology of  $\text{PbI}_2 \cdot \text{DMF}$ , (b) SEM images of  $\text{PbI}_2 \cdot \text{DMF}$  seed crystals (scale bar: 100 nm). Pb, I, C, N, O and H atom are dark grey, brown, grey, blue, red and white color, respectively.

$\text{PbI}_2 \cdot \text{DMF}$  seed particles yield the hexagonal grains through slow precipitation from DMF solvent, and particles attached in one direction to form a 1D wire as PDGWs. These wires can be used as corresponding templates for PGWs (**Figure 3.5**). Therefore, we investigated the morphology of  $\text{PbI}_2 \cdot \text{DMF}$  seed particles and formation mechanism of the PDGWs through theoretical calculations. First, the crystal morphology of  $\text{PbI}_2 \cdot \text{DMF}$  crystal was calculated as shown in **Figure 3.6a**. It was calculated based on the attachment energy and interplanar distance of  $\text{PbI}_2 \cdot \text{DMF}$  intermediate crystal. It is noted that attachment energy is proportional to crystal growth rate, and inversely proportional to exposed surface area. The obtained morphology was consistent with the  $\text{PbI}_2 \cdot \text{DMF}$  particles,

experimentally confirmed as a hexagonal form (Figure 3.6b). The exposed surfaces in the morphology were (020), (011), (110), (10 $\bar{1}$ ), and (11 $\bar{2}$ ) in the order of large surface area. Overall, the surface area appears dominantly as the growth rate is lower, and results in the lower attachment energy with longer interplanar distance as shown in Figure 3.7. The details of exposed surface structure considering the stable termination are represented in Figure 3.8. The (020) and (011) surfaces have alternatively stacked DMF and PbI<sub>2</sub> layers without any dangling atoms, resulting in low attachment energy. On the other hand, in case of the (110), (10 $\bar{1}$ ), and (11 $\bar{2}$ ) surfaces, the dangling Pb and I atoms were exposed to the surface as the periodically bonded PbI<sub>2</sub> layers along the [100] direction was cleaved. Thus, these surfaces exhibited high attachment energy with high electrostatic interaction due to dangling Pb and I atoms on the surfaces.

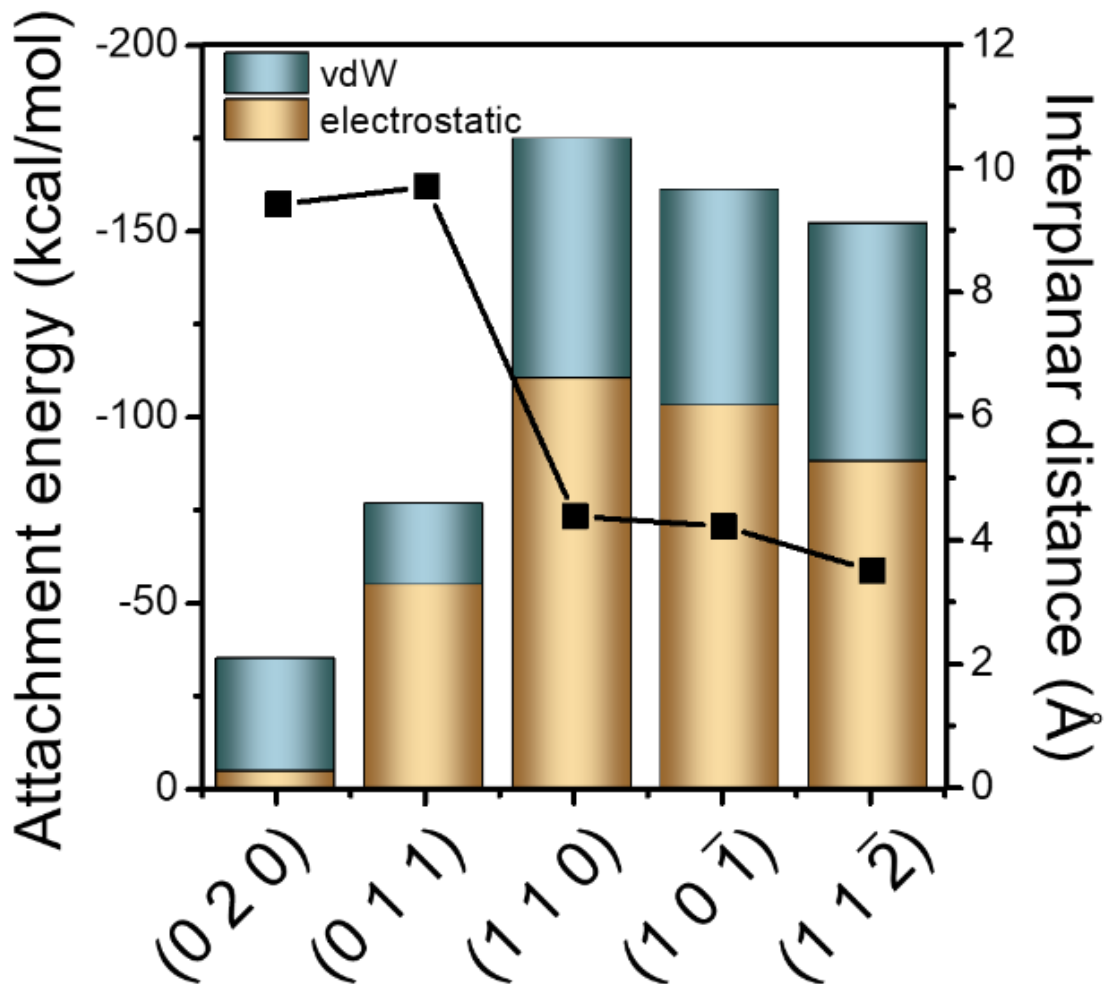
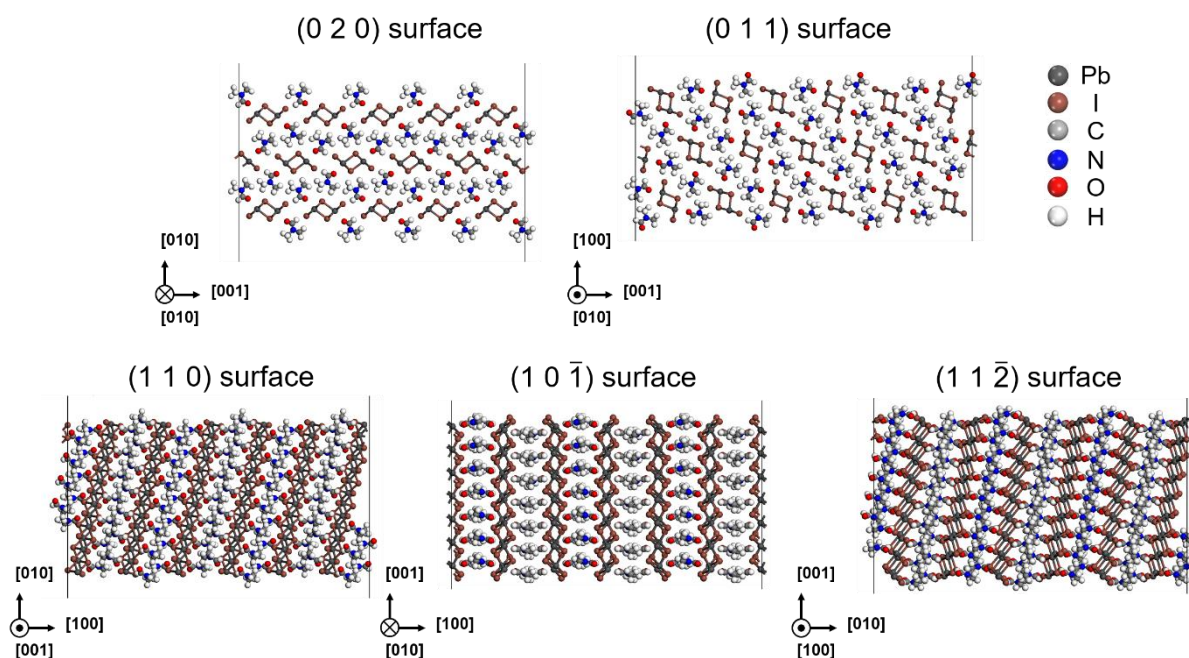


Figure 3.7 Attachment energies and interplanar distances of the exposed surfaces.



**Figure 3.8** The optimized bulk structure and the cleaved (020), (011), (110), (10 $\bar{1}$ ), and (11 $\bar{2}$ ) surfaces of PbI<sub>2</sub>·DMF crystal are shown. Pb, I, C, N, O, and H atoms are represented by dark gray, brown, gray, blue, red, and white, respectively.

**Table 3.3** Lattice parameters for exposed surfaces. Lattice parameters are given for the (020), (011), (110), (10 $\bar{1}$ ), and (11 $\bar{2}$ ) surfaces of PbI<sub>2</sub>·DMF crystal.

	a (Å)	b (Å)	$\gamma$ (°)
(020)	56.642	58.616	91.421
(011)	56.616	65.943	89.268
(110)	56.642	58.107	90.331
(10 $\bar{1}$ )	56.511	60.442	90.000
(11 $\bar{2}$ )	57.214	58.107	81.825

Based on the calculated morphology, the hexagonal particle was adopted for the crystal morphology of the PbI<sub>2</sub>·DMF which composed of ‘Top’ surface (i.e., (020) surface), ‘Side’ (i.e., (011) surface), and ‘Front’ (i.e., (110), (10 $\bar{1}$ ), and (11 $\bar{2}$ ) surfaces). Molecular dynamics (MD) simulations were performed to investigate the interaction between the hexagonal particles. The binding energies between the



exposed surfaces were calculated. Before calculation, we constructed interface model systems for the (020), (011), (110), (10 $\bar{1}$ ), and (11 $\bar{2}$ ) surfaces observed during PbI<sub>2</sub>-DMF growth. The slab thickness for all surfaces was around 30 Å and the area of the surface model was about 60 × 60 Å<sup>2</sup>. The interface systems were constructed using near coincidence site lattice (NCSL) theory [24]. The detailed lattice parameters of each surface are shown in **Table 3.3**. All surfaces were symmetric and stoichiometric and the interface systems were modelled using two identical (A-A interface) or different (A-B interface) surface slab models (**Figure 3.9**). The two slabs were initially separated from each other by 5 Å in the simulation box, where the height was set to 150 Å. A-B interface systems, constructed with two different surfaces, were modelled using the lattice parameters for the A surface, the B surface, and the average of the A and B surfaces, respectively.

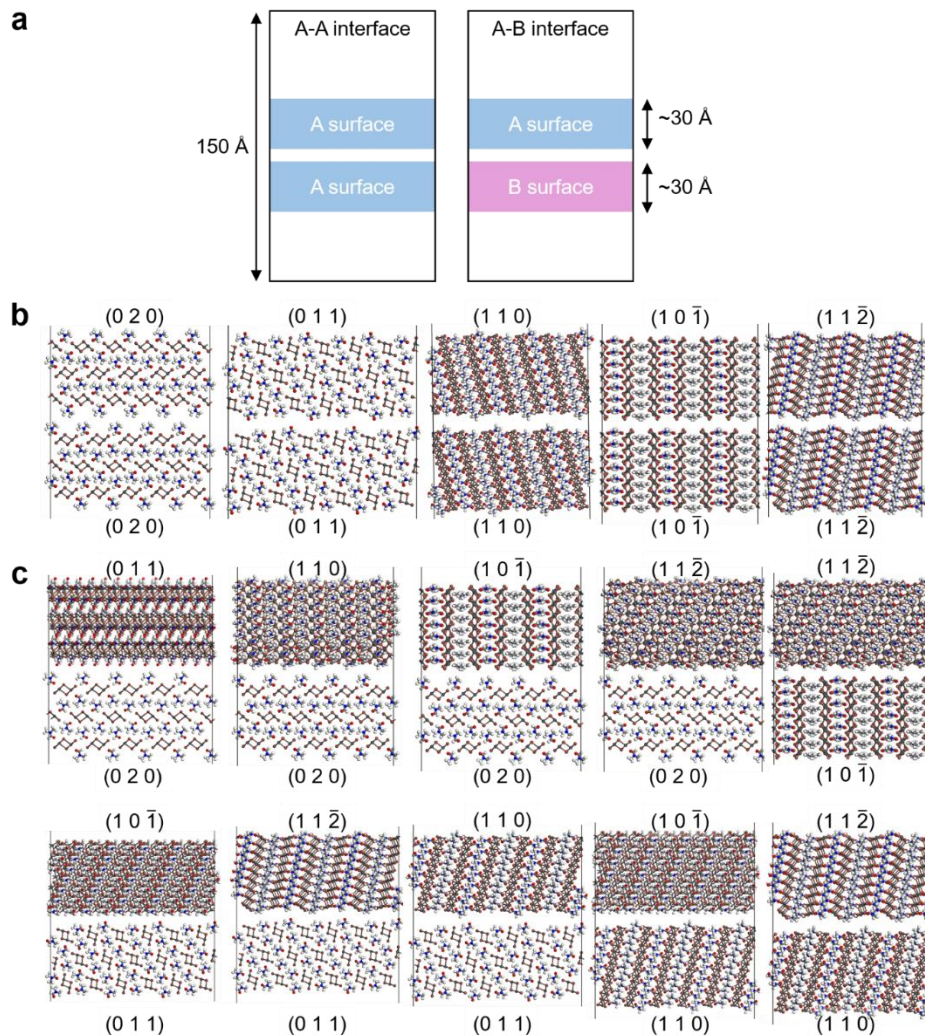


**Figure 3.9** Initial configurations of the interface model system. (a) A schematic shows model system interfaces composed of (b) identical surfaces, i.e., A-A interface, and (c) different surfaces, i.e., A-B interface. Pb, I, C, N, O, and H atoms are represented by dark gray, brown, gray, blue, red, and white, respectively.

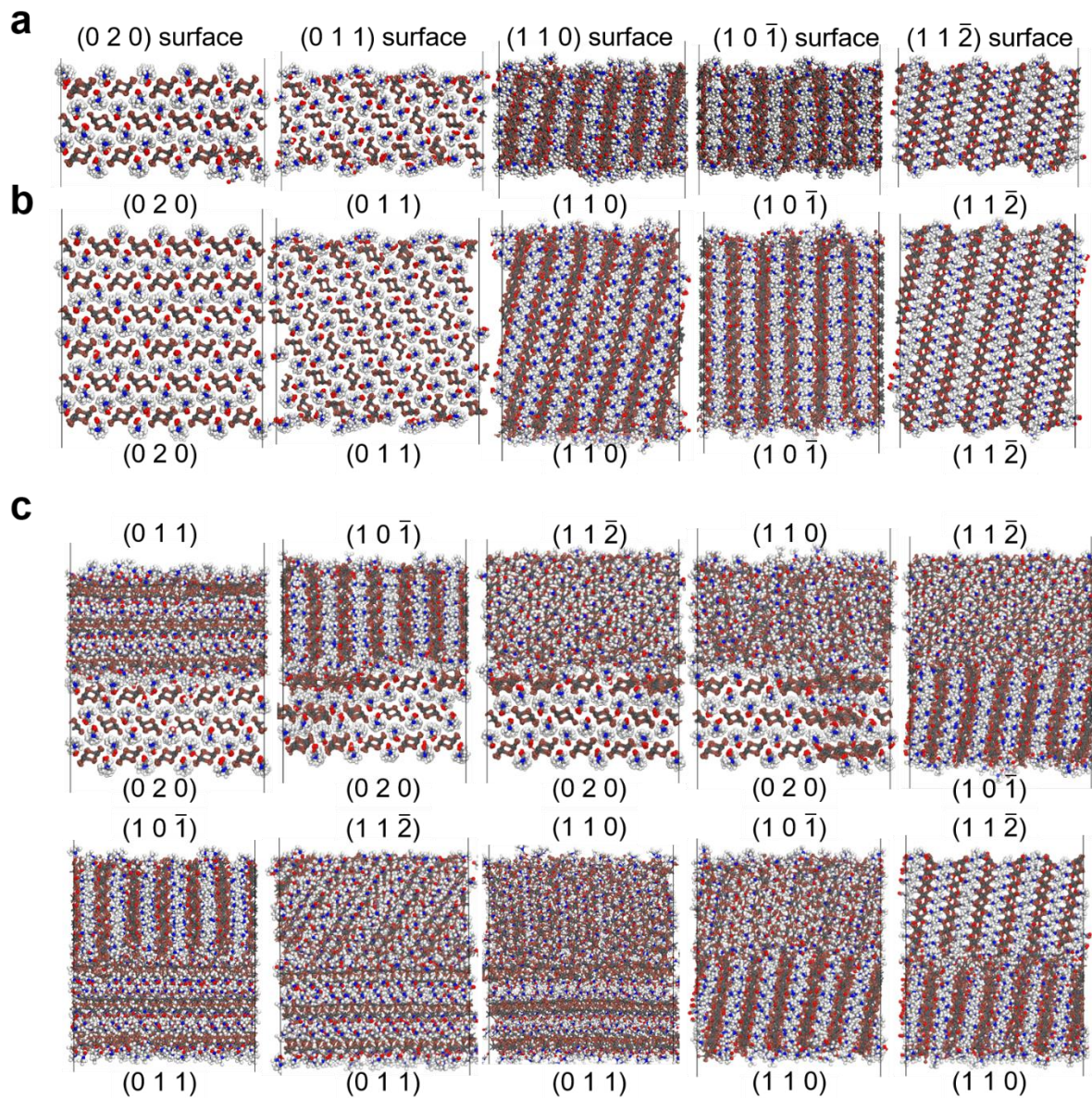


**Figure 3.10** Final configurations of the interface model system. (a) Final configurations are shown for the (020), (011), (110), (10 $\bar{1}$ ), and (11 $\bar{2}$ ) surfaces after 1 ns MD simulations. Final configurations are shown for (b) A-A interfaces, and (c) A-B interfaces after 1 ns MD simulations. Pb, I, C, N, O, and H atoms are represented by dark gray, brown, gray, blue, red, and white, respectively.

The equilibrium configurations of interfacial structures are shown in **Figure 3.10**. Generally, the binding energies between identical surfaces (i.e., A-A interface) were lower than the binding energies between different surfaces (i.e., A-B interface) as shown in **Figure 3.11**. This was due to the epitaxial strain induced by the adhesion of the surfaces with different lattice parameter; the A-B interfaces composed of different surfaces were relatively unfavorable than the A-A interface. More specifically, the A-A interfaces constructed by the ‘Front’ surfaces were more strongly bound than the other

interfaces, because ‘*Front*’ surfaces were composed of relatively reactive surfaces caused by high number of dangling atoms per unit area (i.e., planar density) and low coordination number of the exposed ions (**Figure 3.12** and **Table 3.4**). The binding energies for the A-B interfaces with ‘*Front*’ surfaces were also higher than those for other A-B interfaces. On the other hand, the binding energy between the interface with ‘*Side*’ or ‘*Top*’ surfaces showed lower binding energies due to their relatively low planar density on the surface. In particular, the binding energies between ‘*Front*’ and ‘*Side*’ surfaces, between ‘*Front*’ and ‘*Top*’ surfaces, and between ‘*Side*’ and ‘*Top*’ surfaces, which represent the perpendicular adsorption in the granular wire growth direction, were significantly weaker than those of other interfaces.

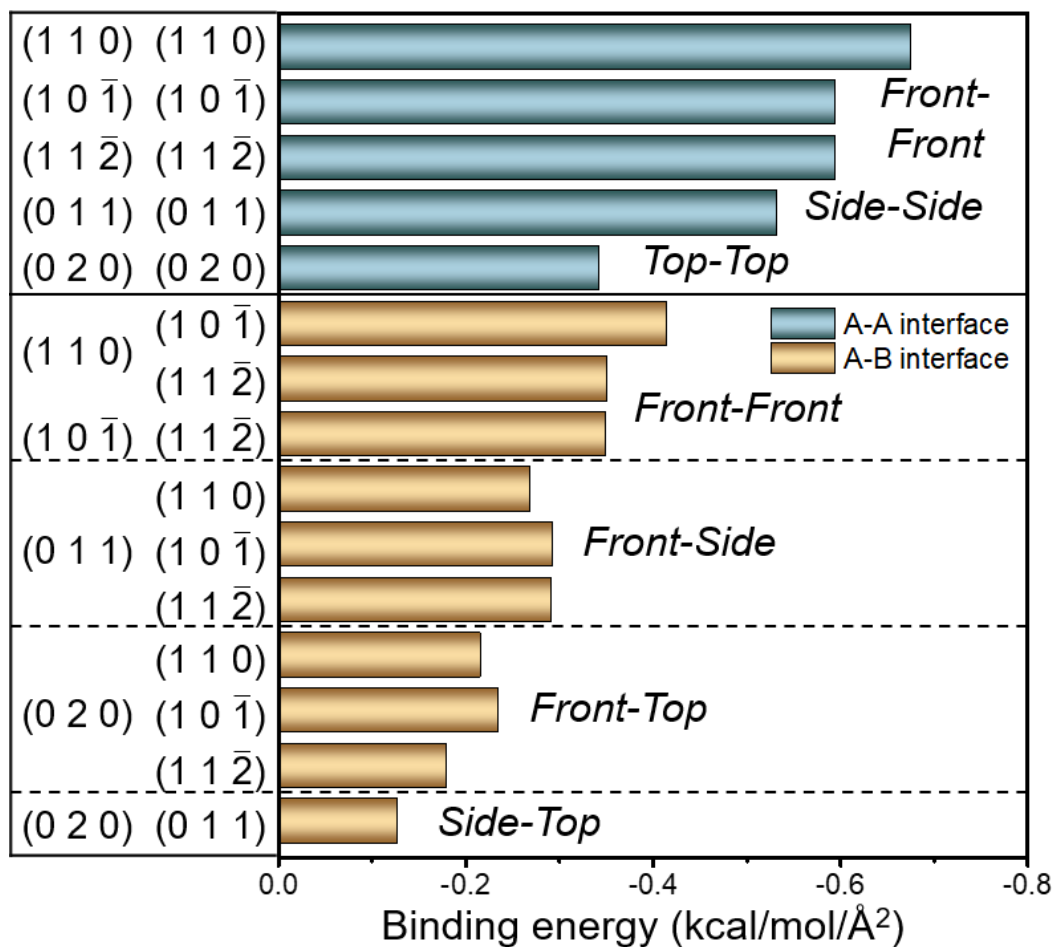


**Figure 3.11** Binding energies between the exposed surfaces.

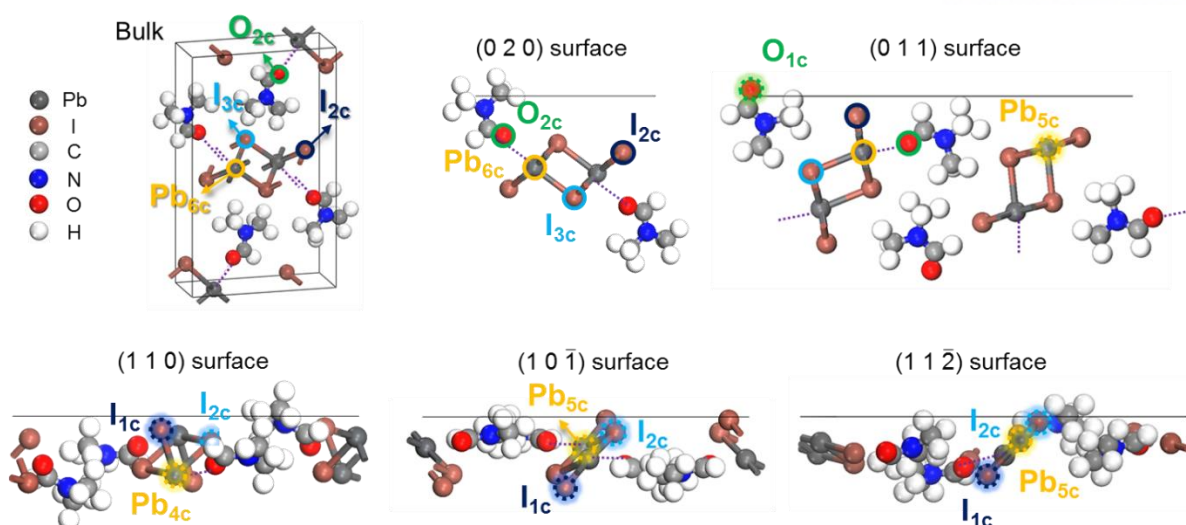


**Figure 3.12** Atomic configurations of bulk and each surface are shown with the atom type and coordination number. The subscript denotes the coordination number (Table 3.4). Pb, I, C, N, O, and H atom are shown in dark gray, brown, gray, blue, red, and white, respectively. Purple dotted lines represent close contact.

**Table 3.4** Planar density of exposed surfaces and coordination number (CN) of outermost dangling atoms.

Surface	Planar density ( $\text{\AA}^{-2}$ )					
	Total	Pb		I	O	
		CN = 5	CN = 4	CN = 2	CN = 1	CN = 1
(020)	–	–	–	–	–	–
(011)	0.0202	0.0101	–	–	–	0.0101
(110)	0.0274	–	0.0091	0.0091	0.0091	–
(10 $\bar{1}$ )	0.0264	0.0088	–	0.0088	0.0088	–
(11 $\bar{2}$ )	0.0219	0.0073	–	0.0073	0.0073	–

Thus, PDGWs were predicted to grow along the forward direction (1D) according to the strong interaction between ‘*Front*’ and ‘*Front*’ surfaces of the crystal morphology of  $\text{PbI}_2 \cdot \text{DMF}$  (**Figure 3.13**). In conclusion,  $\text{PbI}_2 \cdot \text{DMF}$  crystal forms hexagonal-shaped granular particles which is thermodynamically stable, resulting in oriented attachment in the ‘*Front*’ direction to form the granular wire morphology.

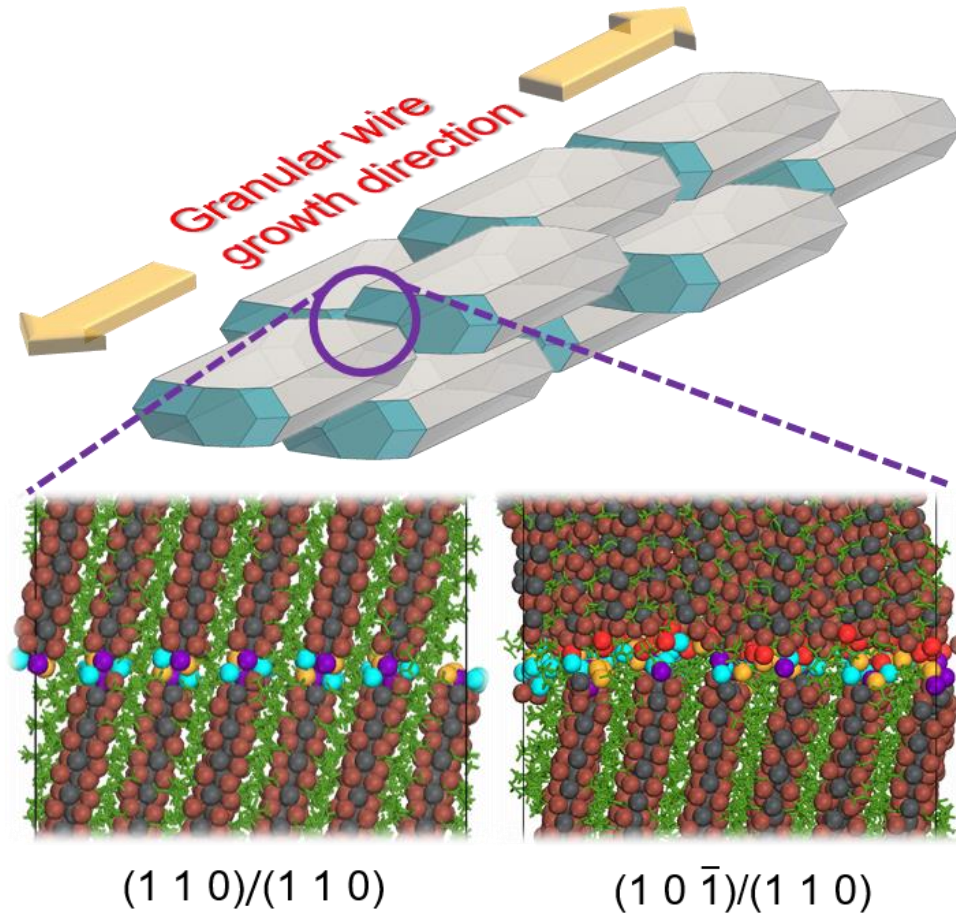


**Figure 3.13** Granular wire growth scheme and its interfacial structures between identical (110) surfaces and between (110) and  $(10\bar{1})$  surface. Bulk Pb and I atoms and DMF molecules are shown in dark gray, brown, and green, respectively. 5- and 4- coordinated Pb atoms are shown in red and purple while 2- and 1- coordinated I atoms are shown in orange and cyan, respectively.

Given the growth mechanism of the granular wire, it forms the grain boundaries with the contacts of the grain surfaces. Due to the grain boundaries, the defects form easily on the surface and generate trap states (i.e., defect transition states) in the bandgap. Recent experiments on polycrystalline lead iodide perovskite films have indicated the presence of charge carrier traps on the perovskite surface (**Figure 3.14**) [25,26]. These traps probably cause the capture of free electrons or holes on the surface of lead iodide perovskite, resulting in the formation of localized energy states within the bandgap of the bulk

material. The unbalanced energy state between grain boundaries and the bulk material gives rise to band bending [27,28]. The band bending occurs at the grain boundaries of perovskite. The suppression of dark current in our PGW devices is due primarily to band bending at the perovskite grain surface and the structure of the PGWs formed by the aggregation of perovskite grain crystals. Therefore, we speculated that ultrahigh detectivity (i.e.,  $3.17 \times 10^{15}$  Jones) of our PGWs largely originates from two distinct electronic properties that result in decreased dark current: the easy generation of deep trap states at the surface and upward band bending at grain boundaries

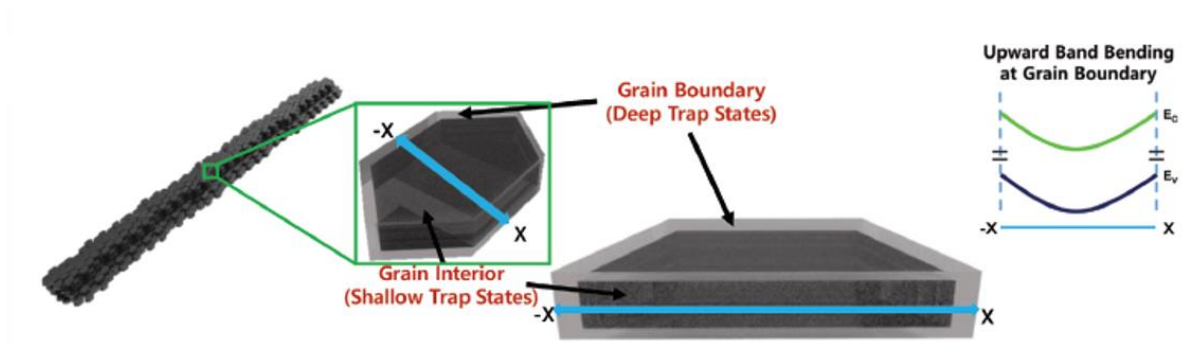


**Figure 3.14** Schematic of band bending of PGWs due to trap states on the surface in the radial direction.

### 3.4 Conclusion

Control over the morphology and crystallinity of metal halide perovskite materials is of key importance in the development of high-performance optoelectronics. Here, solvent engineering in the perovskite for accomplishing unprecedentedly high photodetectivity ( $3.17 \times 10^{15}$  Jones) were performed. Using DMF polar solvent, the intermediate structure was identified as a  $\text{PbI}_2 \cdot \text{DMF}$  crystal. The DMF solvent intercalated into the  $\text{PbI}_2$  to form intermediate structure due to strong coordination between  $\text{Pb}^{2+}$  and oxygen of DMF. We also investigated the specific growth conditions for PDGWs and confirmed the growth mechanism of PDGWs. Under the closed system, the slow crystallization induced to form granular. We examined that the thermodynamic stable morphology of  $\text{PbI}_2 \cdot \text{DMF}$  crystal has a hexagonal granular shape. The one-dimensional self-assembly of perovskite grains is driven by differences in the interaction energies between exposed surfaces of the granular particles. Due to its 1D granular wire shape, many grain boundaries and defects were formed on the surface, which generate trap states (i.e., defect transition states) in the bandgap. Due to the easy generation of deep trap states at the surface resulting from the granular wire shape and upward band bending at grain boundaries, the dark current of PGWs were suppressed. The inherent photodetection ability originates from an extremely low dark current that is limited by energetic barriers featuring unique band-edge modulation along the long axis of wire. The “self-assembled nanograin engineering” strategy developed in this study provides a viable method for the development of high-performance perovskite photodetectors and can be extended to other integrated optoelectronic systems.

### 3.5 References

1. M. A. Green, A. Ho-Baillie, and H. J. Snaith, *Nat. Photonics* **2014**, *8*, 506–514.
2. L. Youngbin, K. Jeong, H. Euyheon, R. Chang-Ho, Y. W. Jong, A. Jong-Hyun, P. J. Hyeok, and C. J. Ho, *Adv. Mater.* **2015**, *27*, 41–46.
3. F. P. Garcia de Arquer, A. Armin, P. Meredith, and E. H. Sargent, *Nat. Rev. Mater.* **2017**, *2*, 16100.
4. P. Liu, X. He, J. Ren, Q. Liao, J. Yao, and H. Fu, *ACS Nano* **2017**, *11*, 5766–5773.
5. S. D. Stranks, and H. J. Snaith, *Nat. Nanotechnol.* **2015**, *10*, 391–402.
6. N. J. Jeon, J. H. Noh, Y. C. Kim, W. S. Yang, S. Ryu, and S. I. Seok, *Nat. Mater.* **2014**, *13*, 897–903.
7. Y. Jo, K. S. Oh, M. Kim, K. H. Kim, H. Lee, C. W. Lee, and D. S. Kim, *Adv. Mater. Interfaces* **2016**, *3*, 1500768.
8. A. Wakamiya, M. Endo, T. Sasamori, N. Tokitoh, Y. Ogomi, S. Hayase and Y. Murata, *Chem. Lett.*, **2014**, *43*, 711–713.
9. X. Liu, L. Gu, Q. Zhang, J. Wu, Y. Long, and Z. Fan, *Nat. Commun.* **2014**, *5*, 1–9.
10. F. Meneses, S. E. Urreta, J. Escrig, and P. G. Bercoff, *Curr. Appl. Phys.* **2018**, *18*, 1240–1247.
11. H. Zeng, S. Michalski, R. D. Kirby, D. J. Sellmyer, L. Menon, and S. Bandyopadhyay, *J. Phys.: Condens. Matter* **2002**, *14*, 715.
12. T. L. Wade, and J. E. Wegrowe, *Eur. Phys. J. Appl. Phys.* **2005**, *29*, 3–22.
13. P. Hartman, and P. Bennema, *J. Cryst. Growth* **1980**, *49*, 145–156.
14. J. Wang, R. M. Wolf, J. W. Caldwell, P. A. Kollman, and D. A. Case, *J. Comput. Chem.* **2004**, *25*, 1157–1174.
15. J. Wang, and T. Hou, *J. Chem. Theory Comput.* **2011**, *7*, 2151–2165.
16. C. M. Handley, and C. L. Freeman, *Phys. Chem. Chem. Phys.* **2017**, *19*, 2313–2321.
17. A. A. Samoletov, C. P. Dettmann, and M. A. J. Chaplain, *J. Stat. Phys.* **2007**, *128*, 1321–1336.
18. P. P. Ewald, *Annalen der Physik* **1921**, *369*, 253–287.
19. M. P. Tosi, *in Solid State Phys.* **1964**, *16*, 1–120.
20. S. J. Clark, M. D. Segall, C. J. Pickard, P. J. Hasnip, M. I. Probert, K. Refson, M. C. Payne, and Z. Kristallogr. *Cryst. Mater.* **2005**, *220*, 567-570.
21. J. P. Perdew, K. Burke, and M. Ernzerhof, *Phys. Rev. Lett.* **1996**, *77*, 3865–3868.
22. A. Tkatchenko, and M. Scheffler, *Phys. Rev. Lett.* **2009**, *102*, 073005.
23. H. J. Monkhorst, and J. D. Pack, *Phys. Rev. B* **1976**, *13*, 5188–5192.
24. T. Sayle, R. Catlow, D. Sayle, S. Parker, and J. Harding, *Philos. Mag. A* **1993**, *68*, 565–573.
25. H. J. Snaith, A. Abate, J. M. Ball, G. E. Eperon, T. Leijtens, N. K. Noel, S. D. Stranks, J. T. W. Wang, K. Wojciechowski, and W. Zhang, *J. Phys. Chem. Lett.* **2014**, *5*, 1511–1515.



26. X. X. Wu, M. T. Trinh, D. Niesner, H. M. Zhu, Z. Norman, J. S. Owen, O. Yaffe, B. J. Kudisch, and X. Y. Zhu, *J. Am. Chem. Soc.* **2015**, *137*, 2089–2096.
27. Z. Zhang, and J. T. Yates, *Chem. Rev.* **2012**, *112*, 5520–5551.
28. C. Y. Chen, J. R. D. Retamal, I. W. Wu, D. H. Lien, M. W. Chen, Y. Ding, Y. L. Chueh, C. I. Wu, and J. H. He, *ACS Nano* **2012**, *6*, 9366–9372.

## Chapter 4. Morphological Engineering of Quantum Dots through Oleate Ligand-ZnSe Shell Interaction with Temperature Control

*This chapter includes the published contents:*

Haewoon Seo<sup>†</sup>, [Ju Hyun Park](#)<sup>†</sup>, O-Hoon Kwon, O. Pil Kwon, Sang Kyu Kwak<sup>\*</sup>, and Sang-Wook Kim<sup>\*</sup>, “Highly Qualified InP Based QDs through Temperature Controlled ZnSe Shell Coating Process and Their DFT Calculation” *Nanoscale Advances*, 2, 5615–5622, 2020 (<sup>†</sup>: **equally contributed**)  
Reprinted with permission. Copyright © The Royal Society of Chemistry 2020

---

### 4.1 Introduction

Colloidal semiconductor nanocrystals (NCs), commonly known as quantum dots (QDs), have been extensively studied in various fields, such as light emission [1-4] and light energy harvesting [5-8], owing to their inherent optoelectronic properties. Among them, research on QDs that can be applied to displays by using a narrow emission linewidth and emission peak tuning depending on the size of the QDs is in progress. In particular, CdSe-based core/shell QDs exhibited superior optical properties and stability compared to organic dyes [9-11]. However, the usage of cadmium is regulated worldwide due to its toxicity [12]. Therefore, as an alternative material, InP-based QDs are the most noteworthy noticed.

Unfortunately, the performance of such InP-based QDs is inferior to that of CdSe-based QDs in many parts, especially in the wide linewidth of emission light in all visible regions, which is represented by full width at half maximum (FWHM). The FWHM of emission light is an important characteristic in displays because it affects the color gamut – in particular, a wider color gamut can be obtained with a narrower FWHM. However, in the case of InP QDs as the core, the main research has been focused on achieving high efficiency to alternate CdSe in the green and red emission ranges [13-15]. In terms of the FWHM aspect, green has a FWHM of approximately 40-45 nm on average, and 36 nm for the narrowest emission [16]. Some studies have been conducted to improve the photoluminescence (PL) line narrowing of InP-based QDs. For example, Li et al. controlled the reaction temperature and used new precursors, which resulted in a quantum yield (QY) of 70% and FWHM of 45 nm in green [17]. However, the method did not have any effects on the red color.

As a part of another effort, a buffer layer between the InP core and ZnS shell was developed and demonstrated the effects. InP/GaP/ZnS core/shell/shell structures that used a GaP buffer layer between the InP core and ZnS shell have been fabricated [18,19]. The QDs exhibited an FWHM of 42 nm and QY of 85%; however, narrower emission was impossible through forming a thicker GaP layer.

Ramasamy et al. used a ZnSe buffer layer between InP and ZnS; as a result, spherical shaped InP/ZnSe/ZnS core/shell/shell QDs were fabricated [20]. To coat high-quality ZnSe shells on InP, the addition of ZnSe precursors was finely controlled, and a QY of 50-70% and an FWHM of 38 nm in green and 44 nm in red were obtained [21]. Going beyond the previous studies, to induce the more confined effect depending on the morphology for high efficiency, we introduced the heating-up method which control the temperature.

In this study, InGaP/ZnSe/ZnS core/shell/shell QDs were obtained by coating a ZnSe shell on the InGaP core with oleate ligand, using a heating-up method in which ZnSe precursors were added to a low-temperature core solution and then rapidly raised to a temperature higher than 300 °C. Thus, tetrahedral-shaped QDs having an FWHM of 37 nm, green emission of 532 nm, and QY of 85% were obtained. In the experiment, ZnSe with a bandgap of 2.7 eV and a lattice parameter of 5.66 Å played the role of a lattice buffer layer between the core and outer shell in the type-I band offsets. In addition, this method was applied to red-emitting QDs, and the emission FWHM of more than 60 nm was reduced to 40.4 nm. High crystallinity was obtained, and the QY significantly improved to 78%. To understand the phenomena of highly improved FWHM, temperature-controlled experiments were conducted with theoretical calculations. For the interaction of oleate ligand as a function of temperature, Gibbs free energy calculations were performed to evaluate the morphology depending on the temperature.

## 4.2 Computational details

### 4.2.1 Density functional theory (DFT) calculation

DFT calculations were performed using the Dmol<sup>3</sup> program [22,23]. For the exchange-correlation energy, the generalized gradient approximation with the Perdew–Burke–Ernzerhof functional was used, and the semiempirical Grimme method for dispersion correction was applied [24,25]. All electron relativistic method was employed for core treatment. The spin-polarized calculations were carried out using the DNP 4.4 basis set. The Brillouin zone was integrated using a  $2 \times 2 \times 1$  k-point grid with the Monkhorst–Pack scheme for surface systems [26]. The convergence criteria for the geometry optimization were  $1.0 \times 10^{-5}$  Ha, 0.002 Ha/Å, and 0.005 Å for energy, force, and displacement, respectively. The self-consistent field convergence was less than  $1.0 \times 10^{-6}$  Ha, and the electron smearing value was set to 0.005 Ha.

### 4.2.2 Gibbs free energy for temperature effect

The Gibbs free energy of system ( $\Delta G_{sys}$ ) can be calculated as

$$\Delta G_{sys} = \Delta E_{sys} + \Delta ZPE_{sys} - T\Delta S_{sys} \quad (1)$$

where  $\Delta E_{sys}$  is the total energy difference of the system,  $\Delta ZPE_{sys}$  is the difference in zero-point energy of the system, and  $\Delta S_{sys}$  is the total entropy difference of the system.  $E$  and  $S$  were calculated based on the contributions of translational, rotational, and vibrational motions:  $E = E_0 + E_{translation} + E_{rotation} + E_{vibration}$ ;  $S = S_{translation} + S_{rotation} + S_{vibration}$  where  $E_0$  is the electronic energy of ground state. Subscript *sys* represents *bind*, *ad*, *struc*, and *rec*, which stand for binding, adsorption, structure, and reconstruction, respectively. The binding energy ( $\Delta E_{bind}$ ) can be expressed as follows

$$\Delta E_{bind} = E_{surf+Zn(oleate)_2} - E_{rec} - E_{adsorbed} \quad (2)$$

where  $E_{surf+Zn(oleate)_2}$  is the total energy of binding of Zn(oleate)<sub>2</sub> to the surface, and  $E_{rec}$  and  $E_{adsorbed}$  are the total energies of the reconstructed surface and adsorbed Zn(oleate)<sub>2</sub>, respectively. The adsorption energy ( $\Delta E_{ad}$ ) can be expressed as follows.

$$\Delta E_{ad} = E_{surf+Zn(oleate)_2} - E_{slab} - E_{Zn(oleate)_2} \quad (3)$$

where  $E_{slab}$  and  $E_{Zn(oleate)_2}$  are the total energies of the ZnSe slab model and an isolated Zn(oleate)<sub>2</sub>, respectively. The reconstruction energy of surface ( $\Delta E_{rec}$ ) and the structural deformation energy of adsorbate ( $\Delta E_{struc}$ ) can be expressed as

$$\Delta E_{rec} = E_{rec} - E_{slab} \quad (4)$$

$$\Delta E_{struc} = E_{adsorbed} - E_{Zn(oleate)_2} \quad (5)$$

Thus, the simplified relation between binding energy and adsorption energy is derived in the following equation:

$$\Delta E_{ad} = \Delta E_{bind} + \Delta E_{rec} + \Delta E_{struc} \quad (6)$$

The surface free energy ( $\gamma(hkl)(T)$ ) can be expressed in the following equation [27].

$$\gamma(hkl)(T) = \frac{G^{hkl}_{slab}(T) - G_{bulk}(T)}{2A} \quad (7)$$

where  $G^{hkl}_{slab}(T)$  and  $G_{bulk}(T)$  are the Gibbs free energies of the ( $h k l$ ) slab model and bulk with the same number of atoms for the slab model, respectively.  $A$  is the exposed surface area for a given ( $h k l$ ) plane. The relaxed surface free energy by ligand ( $\gamma_r(hkl)(T)$ ) can be expressed in the following equation [28].

$$\gamma_r(hkl)(T) = \gamma(hkl)(T) + \theta_{hkl} \Delta G_{ad} \quad (8)$$

where  $\theta_{hkl}$  is the ( $h k l$ ) surface coverage of the ligand. By using the relaxed surface free energy, the morphology is predicted from Wulff construction [29].

### 4.3 Results and Discussion

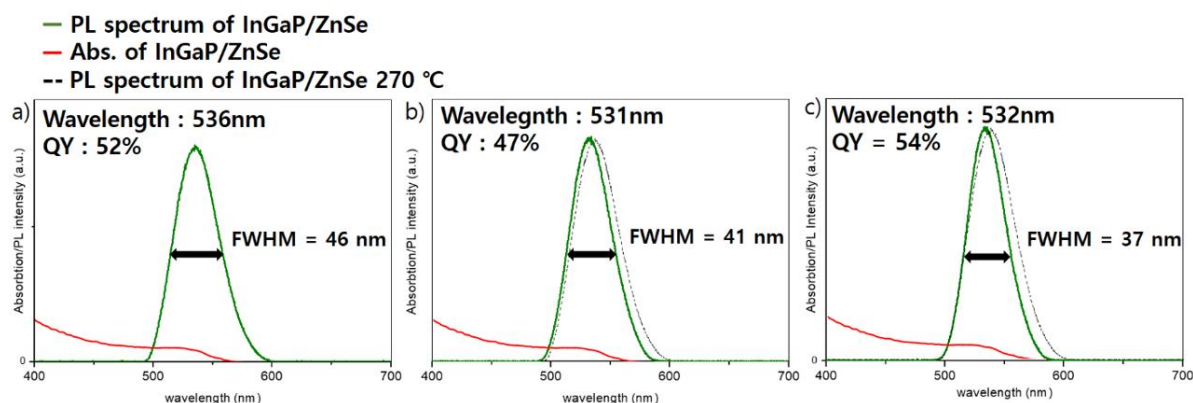


**Figure 4.1** Absorption and PL data of InGaP/ZnSe by ZnSe shell coating temperature at (a) 270 °C, (b) 300 °C and (c) 320 °C.

In experiment, clear absorption peak shoulder of the InGaP core is observed when heated to 300 °C. The InGaP core has a size of about 2.2–2.5 nm and shows an absorption peak at about 430 nm. When the ZnS shell is coated on InGaP core without the ZnSe buffer layer, the QY of 85% and a FWHM of 41 nm are observed. It is quite high QY, but relatively wide value of FWHM. To improve the optical characteristics, we coated an additional II–VI type ZnSe layer between the core and ZnS shell to release the interfacial stress. Zinc oleate and TOP-Se, used as precursors of the ZnSe shell, were added to the core solution at 200 °C, and the solution was heated as function of temperature. To optimize the optical properties of the QDs, especially the FWHM, the ZnSe shell coating temperature was tuned to 270 °C, 300 °C, and 320 °C. The resulting optical effects are illustrated in **Figure 4.1**. The FWHM and the peak of emission wavelength were 46 nm at a wavelength of 536 nm at 270 °C, 41 nm at 531 nm at 300 °C, and 37 nm at 532 nm at 320 °C. As the temperature increased, the QDs exhibited a narrower FWHM; however, the peaks of the emission wavelength were observed at similar wavelengths regardless of temperature. The average value of QYs of the QDs was approximately 50%. The reactions under 270 °C (i.e., at 250 °C) exhibited similar results to those at 270 °C. At more than 320 °C, reactions using a high boiling-temperature solvent (i.e., 340 °C reaction temperature) resulted in aggravated QY and FWHM of QDs. As the temperature increases, the size of particle increases (**Figure 4.2**), and the tetrahedron shape can be observed in overall. For the details, the morphology of the QDs became to be a truncated tetrahedron shape.

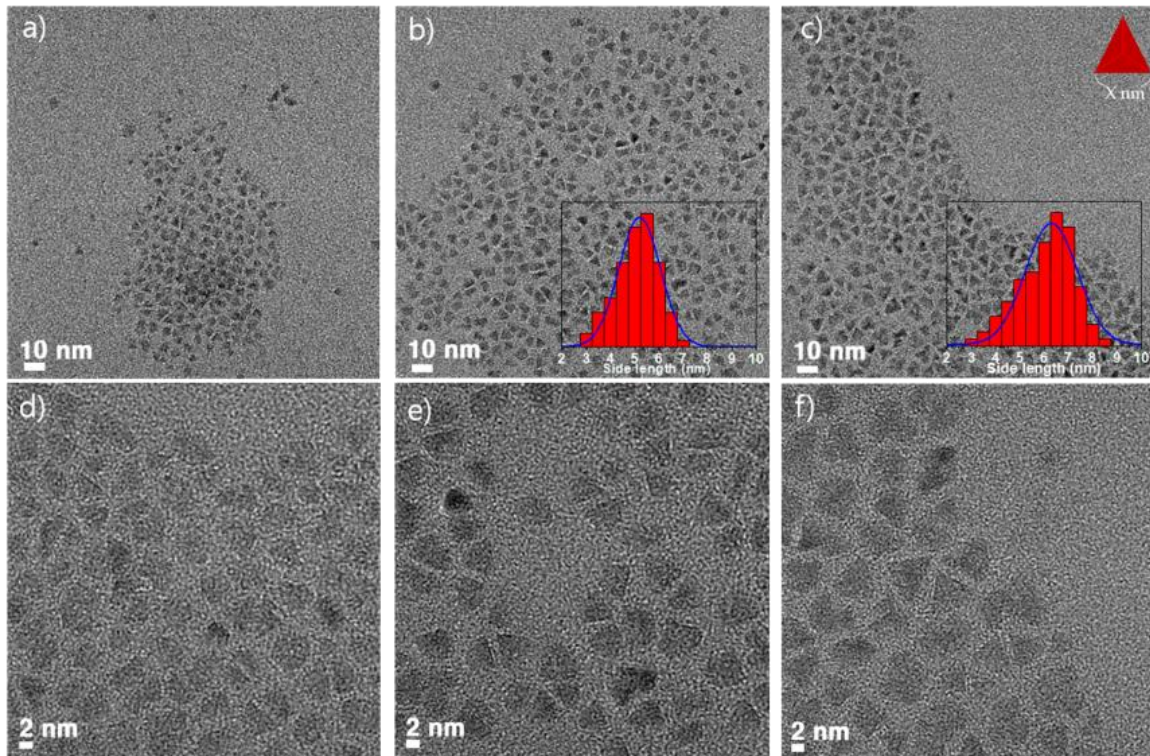


**Figure 4.2** TEM image of InGaP/ZnSe; (a,d) shell coated at 270 °C, (b,e) shell coated at 300 °C, and (c,f) shell coated at 320 °C.

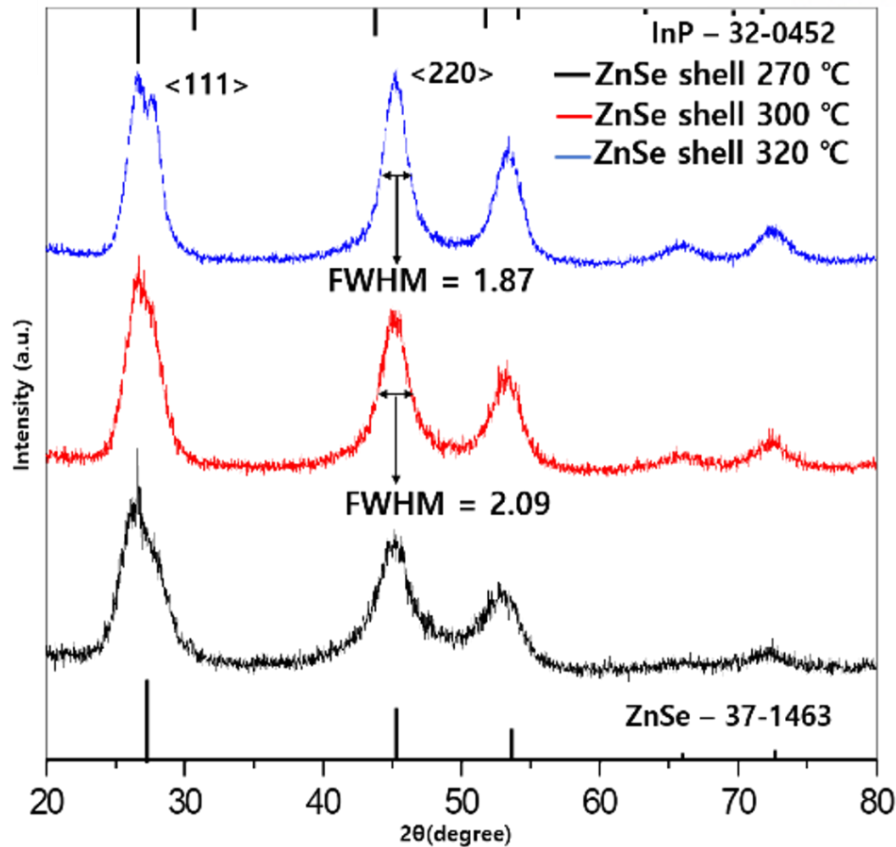


**Figure 4.3** PXRD patterns of InGaP/ZnSe by ZnSe shell coating temperature at 270 °C, 300 °C, and 320 °C.

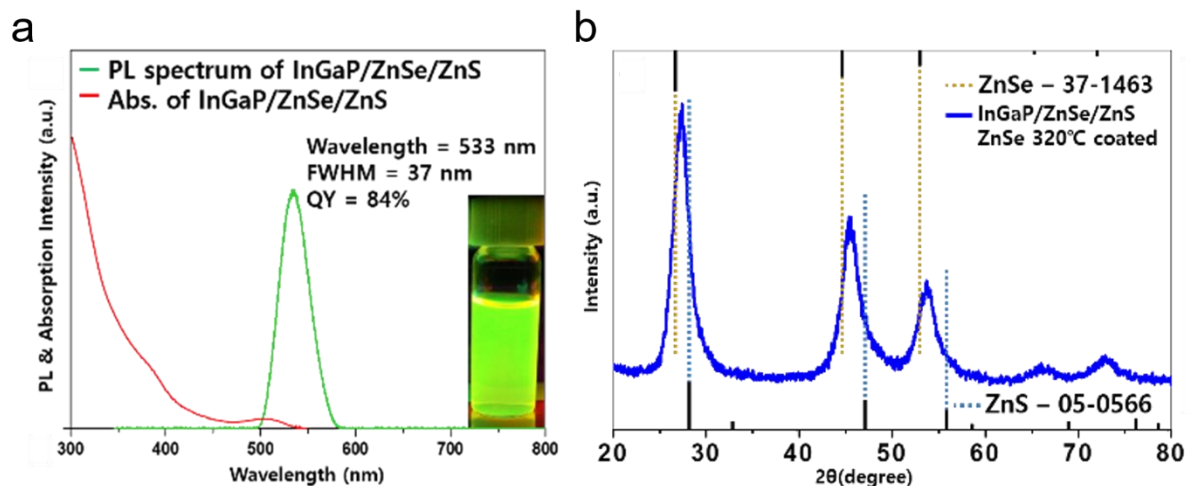


**Figure 4.4** (a) PL & absorption data of InGaP/ZnSe/ZnS, (b) PXRD pattern of InGaP/ZnSe/ZnS

To elucidate the structure-property relation depending on the temperature, the morphology and crystal structures were analysed using PXRD as shown **Figure 4.3**. Generally, the change of morphology occurs because of the relative stability of the crystal facet and adsorption/desorption characteristics of



the surfactants under high-temperature annealing. The PXRD data showed that every diffraction peak including  $\langle 111 \rangle$ ,  $\langle 220 \rangle$ , and  $\langle 311 \rangle$  became sharpened as the temperature increased. The FWHM values of the  $\langle 220 \rangle$  peak at 320 °C, 300 °C, and 270 °C were 1.87, 2.09, and 2.24, respectively, implying that the crystallinity improved as the temperature increased. In the core/shell structure, the diffraction peaks in the PXRD patterns shifted to the peak of the ZnSe (i.e., shell material), which were usually located between the core and shell peaks. However, the PXRD peaks of the InGaP/ZnSe core/shell were located on the ZnSe position, indicating that the ZnSe shell was very thick. Also, as the temperature increased, the  $\langle 220 \rangle$  peak developed rather than a  $\langle 111 \rangle$  peak. The PXRD pattern demonstrated that the  $\langle 220 \rangle$  peak was higher than the  $\langle 111 \rangle$  peak. The  $\langle 111 \rangle$  peak was split, and the peak of the InP core also appeared. This phenomenon may be attributed to the high crystallinity of the inner core because of annealing at a high temperature during ZnSe shell coating. This also indicates that high-temperature annealing affects not only the ZnSe shell coating, but also the crystallinity of the core itself. Finally, the QDs exhibited the significantly increase of QY from 54% to 84%, and the PXRD pattern exhibited a small shift of every peak from ZnSe to ZnS (**Figure 4.4**). The improved performance (i.e., higher QY and narrower FWHM) was attributed to the morphological change from spherical [21] to truncated tetrahedral shape.

**Table 4.1.** Interplanar distance according to the miller indices of the possible growth surfaces of zincblende ZnSe

$h k l$	Interplanar distance (Å)
{111}	3.272
{11 $\bar{1}$ }	3.272
{200}	2.834
{220}	2.004

The relationship between temperature and InGaP/ZnSe QD morphology were studied by DFT calculations. Since the volume of the ZnSe shell occupies most of the nanoparticles, the focus is on the surface structure of the ZnSe shell to investigate the morphology of QDs. The low index surfaces with relatively large interplanar distances are likely to be exposed [30-32]; thus, the relationship between surface indices and interplanar distances in the ZnSe bulk structure was examined as represented in **Table 4.1**. The slab models representing each surface were stoichiometric, and a vacuum region of approximately 20 Å perpendicular to the surface was applied to avoid self-interaction (**Figure 4.5**). The (111) surface, (11 $\bar{1}$ ) surface, and (200) surface are the polar surfaces which have two different kinds of terminations: Zn- and Se-termination. Each surface energy is represented below each slab model. The

(220) surface is the most stable surface which is the non-polar surface. In case of NCs, the morphology is largely controlled by the ligand. Thus, the interaction of each surface with the ligand is also significantly important [28]. As in the experiment, we considered oleate ligand as  $\text{Zn}(\text{oleate})_2$  model (Figure 4.6), because the X-type ligand (i.e., oleate) can be strongly attached to the ZnSe surface. The interactions between each surface and  $\text{Zn}(\text{oleate})_2$  were calculated considering the surface with stable termination (Figure 4.7). The detailed lattice parameters of each surface and coverage of  $\text{Zn}(\text{oleate})_2$  are shown in Table 4.2.

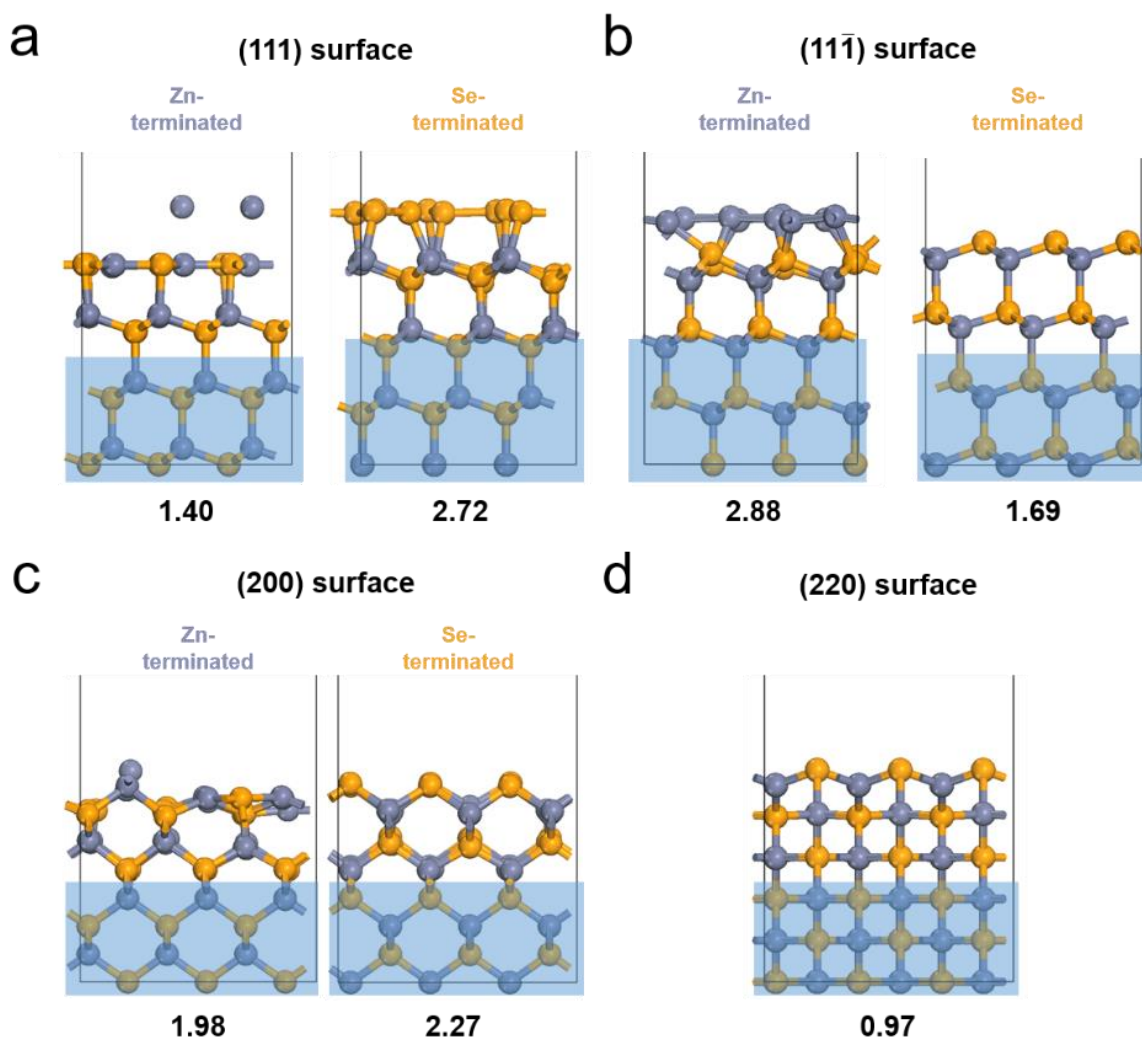


**Figure 4.5** Optimized slab models of (a) ZnSe (111) surface, (b) (111̄) surface, (c) (200) surface, and (d) (220) surface. The numbers below each figure represent the surface energy (in kcal/mol/Å<sup>2</sup>). The bottom blue regions were fixed to theoretically mimic the bulk phase. Zn and Se are represented by navy and orange colored spheres, respectively.

**Table 4.2.** Lattice parameters  $a$ ,  $b$ , and  $\varphi$  for the slab models and coverage ( $\theta$ ) of  $\text{Zn(oleate)}_2$  to each surface for used in the calculation for the relaxed surface free energy.  $\theta$  was assumed to be equal to the number of dangling Se on each surface divided by twice of area. Since the ligand consists of two oleate ions, the coverage for ligand adsorption was taken to be a half of the number of dangling Se exposed on each surface.

$hkl$	$a$ (Å)	$b$ (Å)	$\varphi$ (°)	$\theta$ ( $\text{Zn(oleate)}_2/\text{Å}^2$ )
{111}	12.0137	12.0137	120	0.036
{11 $\bar{1}$ }	12.0137	12.0137	120	0.036
{200}	12.0137	12.0137	90	0.022
{220}	11.3266	12.0137	90	0.031

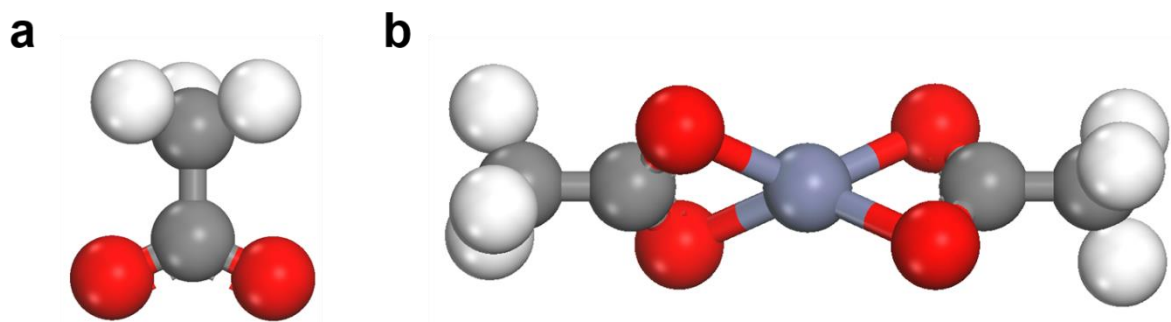


**Figure 4.6** Optimized ligand models of (a) oleate, (b)  $\text{Zn(oleate)}_2$ . The acetate ion was used to represent the oleate ion, which have the same carboxylate group. Zn, O, C, and H are represented by navy, red, grey and white colored spheres, respectively.

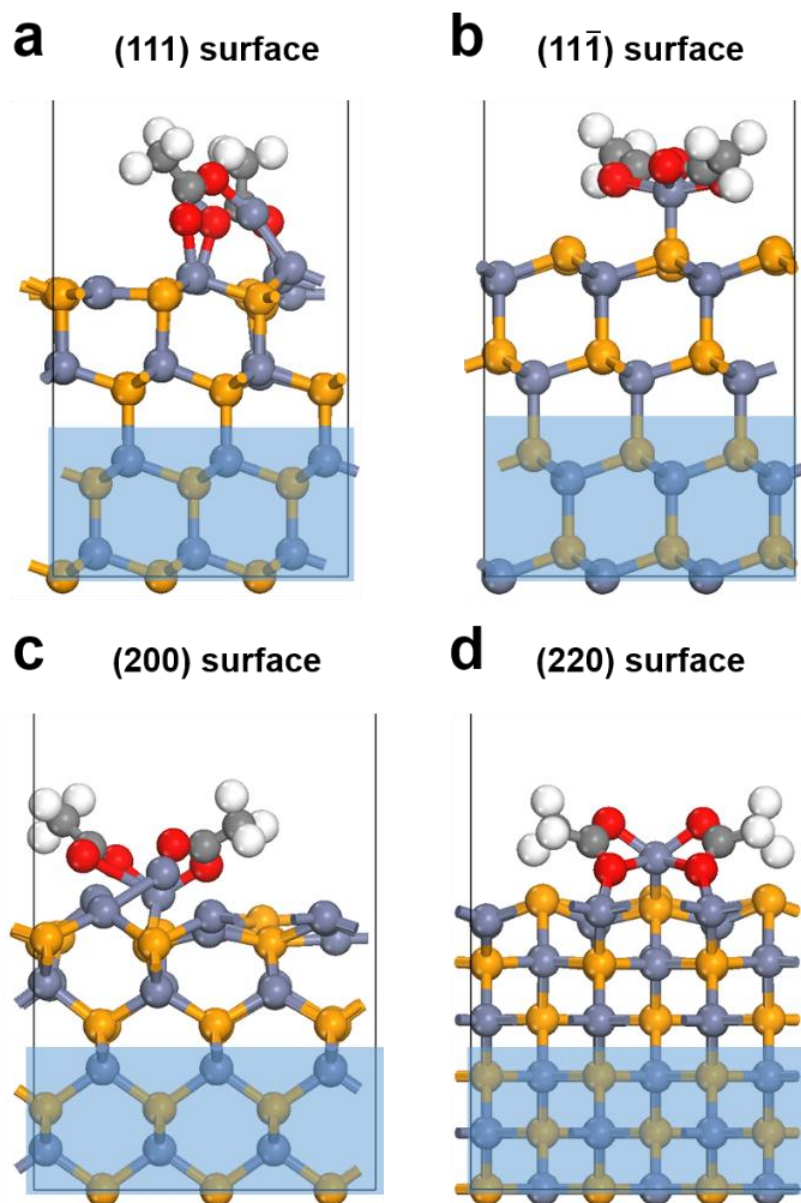


**Figure 4.7** Optimized structures of each ZnSe surface with Zn(oleate)<sub>2</sub> model; (a) ZnSe (111) surface, (b) (11 $\bar{1}$ ) surface, (c) (200) surface, and (d) (220) surface. The bottom blue regions were fixed to theoretically mimic the bulk phase. Zn, Se, O, C, and H are represented by navy, orange, red, grey and white colored spheres, respectively.

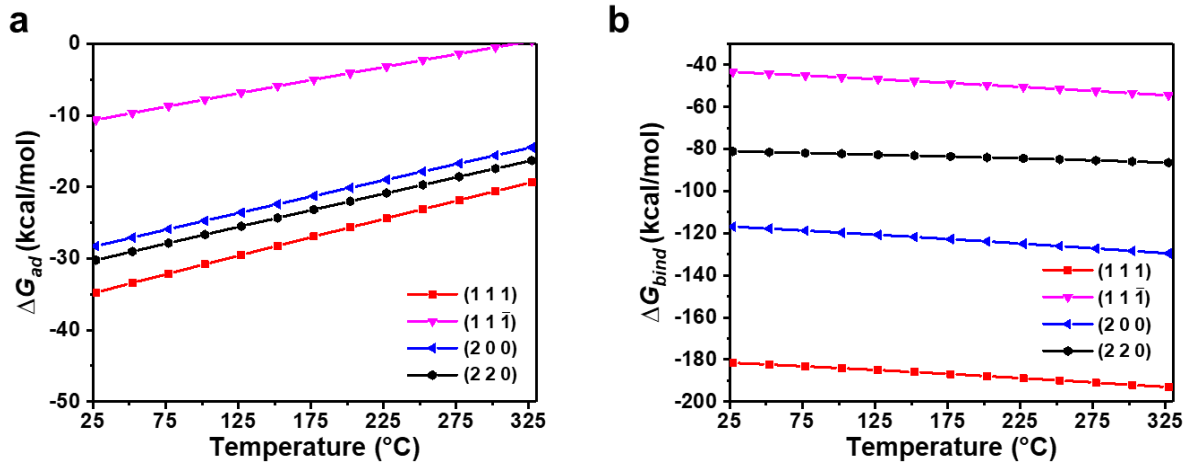


**Figure 4.8** (a) Gibbs free energy for adsorption of oleate ( $\Delta G_{ad}$ ) —  $\Delta G_{ad}$  is calculated from Eqs. (1) and (3). (b) Gibbs free energy of binding of  $\text{Zn(oleate)}_2$  ( $\Delta G_{bind}$ ) to each ZnSe surface depending on temperature, —  $\Delta G_{bind}$  is calculated from Eqs. (1) and (2).

As shown in **Figure 4.8**, the Gibbs free energy of the (adsorption) binding of  $\text{Zn(oleate)}_2$  ( $\Delta G_{bind}$ ) to the (111) surface is the strongest, so we can predict that the tetrahedral-shaped QD surrounded by the (111) surface can be observed. Considering the dimerization-anion passivation or co-passivation, the stabilization effect on cation-terminated (111) surface is higher than that of other surfaces, resulted in tetrahedral shape [33].

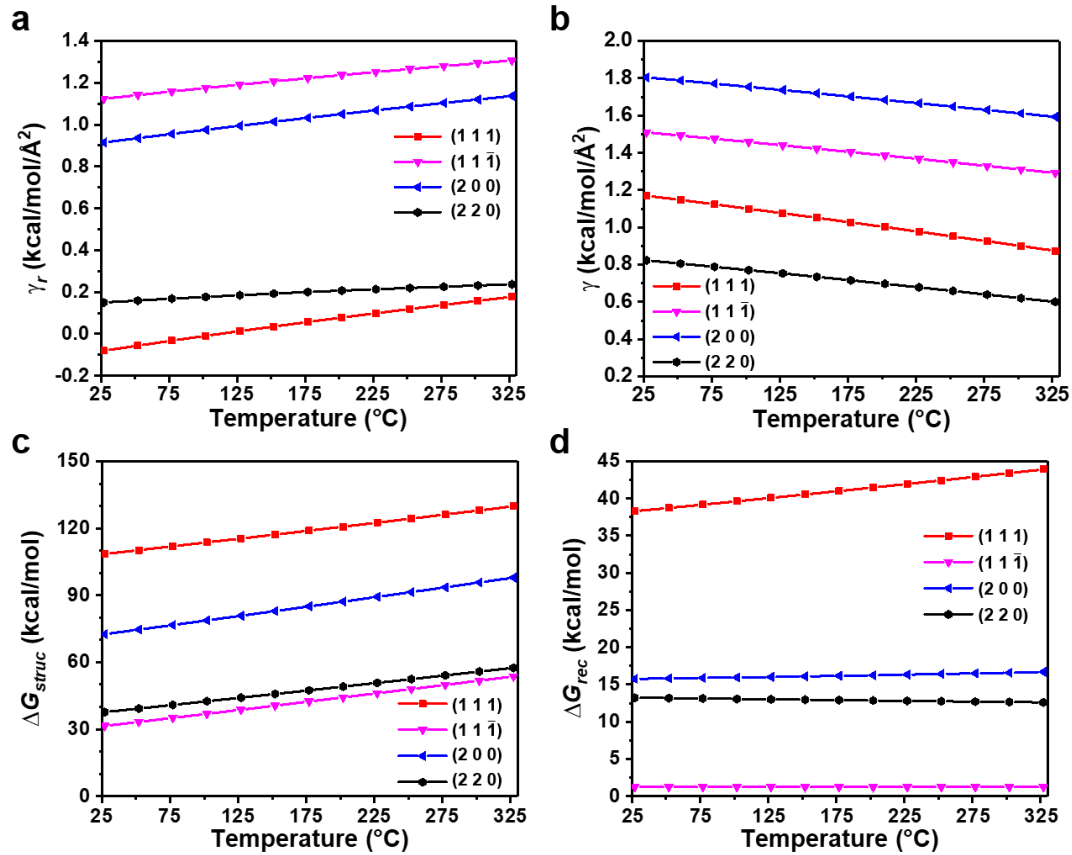


**Figure 4.9** (a) Relaxed surface free energy ( $\gamma_r$ ) as a function of the temperature —  $\gamma_r$  is calculated from Eq.(8). (b) Surface free energy as a function of the temperature —  $\gamma$  is calculated from Eq.(7). (c) Gibbs free energy for structural change of adsorbed Zn(oleate)<sub>2</sub> ( $\Delta G_{struc}$ ) as a function of the temperature —  $\Delta G_{struc}$  is calculated from Eqs. (1) and (5), (d) Gibbs free energy for reconstruction of surface ( $\Delta G_{rec}$ ) as a function of the temperature —  $\Delta G_{rec}$  is calculated from Eqs. (1) and (4).

To further investigate the morphological change depending on temperature, we calculated the relaxed surface free energy ( $\gamma_r$ ) (**Figure 4.9a**). The order of stability of the relaxed surface was (111), (220), (200), and (11 $\bar{1}$ ). Interestingly, the (220) surface became the second most stable because of the large contribution of the surface free energy among other energies as shown in **Figure 4.9b**. Additionally,  $\gamma_r(111)$  and  $\gamma_r(220)$  became asymptotically close as the temperature increased. Subsequently, the equilibrium morphologies depending on the temperature were calculated through the Wulff construction [29] with the  $\gamma_r$ 's (**Figure 4.10**). When the temperature was approximately 227 °C, a tetrahedron predominantly surrounded by a (111) surface was obtained. As the temperature increased further, a (220) surface began to appear at the vertices of the tetrahedron, because the increasing rate of  $\gamma_r(220)$  was the lowest among the surfaces with considerably low  $\gamma_r(220)$  (i.e.; in a high-surface-stability state). These morphological changes can affect the change in the XRD peak intensity [34] (**Figure 4.11**). The increase rate of the <220> peak intensity in the experimental XRD (Figure 4.3) was found to be greater than that

of the  $\langle 111 \rangle$  peak intensity because of the increasing areal fraction of the (220) surface in the tetrahedron. It is unclear as to why the FWHM of PL is narrow; however, previous reports can provide guidance. Kim et al. demonstrated that the electrons in the tetrahedron are subject to more quantum confinement than those in the spherical shape of the same volume [35,36]. As a result, bandgap changes with size nonuniformity in the tetrahedral-shaped QDs are less than those of spherical QDs. Although the edge lengths are slightly different in the tetrahedral shape, the bandgaps are similar, and the FWHM of the PL become narrower. QDs of an InGaP/ZnSe/ZnS structure were fabricated by adding a zinc-DDT complex as a ZnS precursor.

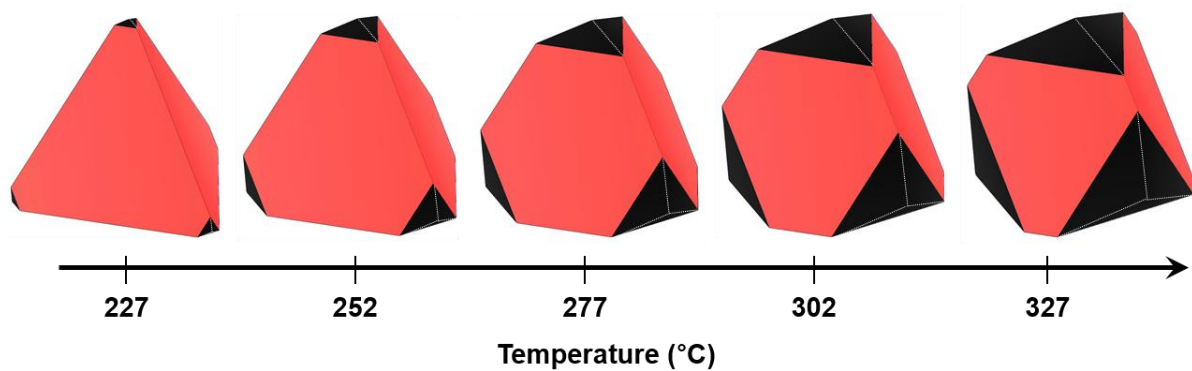


**Figure 4.10** Equilibrium morphology based on  $\gamma_i$ , with respect to temperature — red and black represent the (111) and (220) surfaces, respectively.

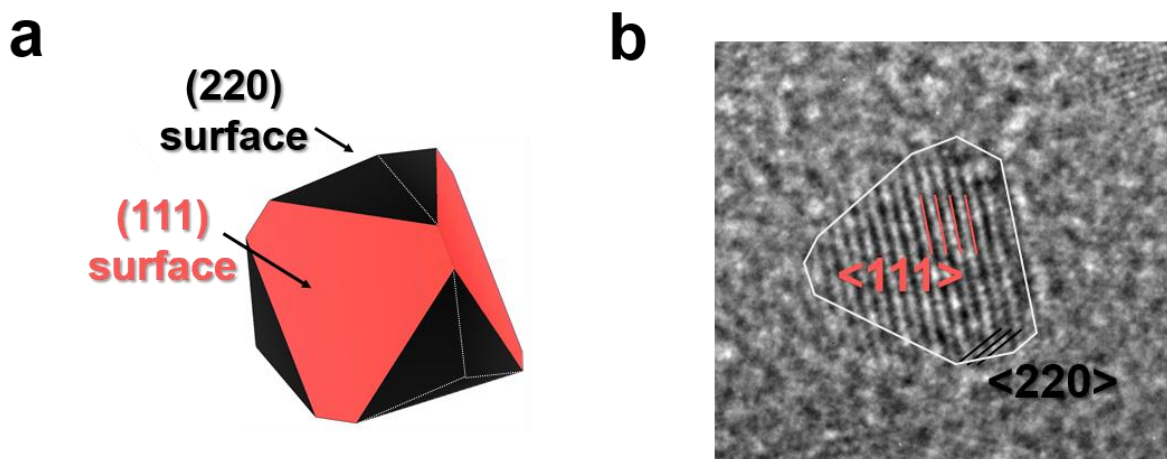


**Figure 4.11** (a) Predicted morphology at 327 °C, and (b) HR-TEM image of InGaP/ZnSe at 320 °C.

## 4.4 Conclusion

At summary, we developed highly qualified InGaP/ZnSe/ZnS QDs with a QY of 85% and emission linewidth of 37 nm FWHM. The QDs had thick ZnSe shells, which were obtained by high-temperature annealing. This annealing process resulted in the formation of tetrahedron-shaped nanoparticles and a very narrow emission linewidth. The morphology is governed by surface stability, which is associated with the interaction between the ligand and crystal surface. When the temperature is approximately 227 °C, a tetrahedron predominantly surrounded by a (111) surface can be obtained, because the ligand strongly binds to the (111) surface. As the temperature increases further, the (220) surface begins to appear at the vertices of the tetrahedron, because  $\gamma_r$  (220) is relatively low, and the increase rate of  $\gamma_r$  (220) is the slowest among the surfaces. These morphological changes can affect the XRD peak intensity, which indicated that the (220) peak increased. Due to its morphology, the electron wavefunctions are more quantum-confined to improve high quantum yield. Through this morphological engineering, the final InGaP/ZnSe/ZnS QDs was also applied to red emission, exhibited a highly improved QY of 78% and emission FWHM of 40 nm at the 623 nm peak.



## 4.5 References

1. E. Jang, S. Jun, H. Jang, J. Lim, B. Kim, and Y. Kim, *Adv. Mater.* **2010**, *22*, 3076–3080.
2. J. H. Chang, D. Hahm, K. Char, and W. K. Bae, *J. Inf. Disp.* **2017**, *18*, 57–65.
3. O. Chen, J. Zhao, V. P. Chauhan, J. Cui, C. Wong, D. K. Harris, H. Wei, H.-S. Han, D. Fukumura, R. K. Jain, and M.G. Bawendi, *Nat. Mater.* **2013**, *12*, 445–451.
4. W. K. Bae, J. Kwak, J. W. Park, K. Char, C. Lee, and S. Lee, *Adv. Mater.* **2009**, *21*, 1690–1694.
5. G. Konstantatos, I. Howard, A. Fischer, S. Hoogland, J. Clifford, E. Klem, L. Levina, and E. H. Sargent, *Nature* **2006**, *442*, 180.
6. N. Huo, S. Gupta, and G. Konstantatos, *Adv. Mater.* **2017**, *29*, 1606576.
7. I. Gur, N. A. Fromer, M. L. Geier, and A. P. Alivisatos, *Science* **2005**, *310*, 462.
8. J. P. Park, J. H. Heo, S. H. Im, and S. -W. Kim, *J. Mater. Chem. A* **2016**, *4*, 785–790.
9. H. S. Jang, H. Yang, S. W. Kim, J. Y. Han, S. -G. Lee, and D. Y. Jeon, *Adv. Mater.* **2008**, *20*, 2696–2702.
10. J. Lim, B. G. Jeong, M. Park, J. K. Kim, J. M. Pietryga, Y. S. Park, V. I. Klimov, C. Lee, D. C. Lee, and W. K. Bae, *Adv. Mater.* **2014**, *26*, 8034–8040.
11. D. V. Talapin, A. L. Rogach, A. Kornowski, M. Haase, and H. Weller, *Nano Lett.* **2010**, *1*, 207–211.
12. European Union Law, 2017; <https://eur-lex.europa.eu/legal-content/EN/TXT/HTML/?uri=CELEX:52017SC0466&rid=6> (accessed date: 23 Jan 2019).
13. J. Lim, M. Park, W. L. Bae, D. Lee, S. Lee, C. Lee, and K. Char, *ACS nano* **2013**, *7*, 9019–9026.
14. E. Ryu, S. Kim, E. Jang, S. Jun, H. Jang, B. Kim, and S. -W. Kim, *Chem. Mater.* **2009**, *21*(4), 573–575.
15. X. Yang, D. Zhao, K. S. Leck, S. T. Tan, Y. X. Tang, J. Zhao, H. V. Demir, and X. W. Sun, *Adv. Mater.* **2012**, *24*, 4180–4185.
16. Y. Kim, S. Ham, H. Jang, J. H. Min, H. Chung, J. Lee, D. Kim, and E. Jang, *ACS Appl Nano Mater.* **2019**, *2*, 1496–1504.
17. L. Li, and P. Reiss, *J. Am. Chem. Soc.* **2008**, *130*, 11588–11589.
18. S. Kim, T. Kim, M. Kang, S. K. Kwak, T. W. Yoo, L. S. Park, I. Yang, S. Hwang, J. E. Lee, S. K. Kim, and S. -W. Kim, *J. Am. Chem. Soc.* **2012**, *134*, 3804.
19. J. P. Park, J. J. Lee, and S. -W. Kim, *Sci. Rep.* **2016**, *6*, 30094.
20. P. Ramasamy, K. J. Ko, J. W. Kang, and J. S. Lee, *Chem. Mater.* **2018**, *30*, 3643–3647.
21. Y. Li, X. Hou, X. Dai, Z. Yao, L. Lv, Y. Jin, and X. Peng, *J. Am. Chem. Soc.* **2019**, *141*, 6448–6452.
22. B. Delley, *J. Chem. Phys.* **1990**, *92*, 508–517.
23. B. Delley, *J. Chem. Phys.* **2000**, *113*, 7756–7764.

24. J. P. Perdew, K. Burke, and M. Ernzerhof, *Phys. Rev. Lett.* **1996**, 77, 3865–3868.
25. S. Grimme, *J. Comput. Chem.* **2006**, 27, 1787–1799.
26. H. J. Monkhorst, and J. D. Pack, *Phys. Rev. B* **1976**, 13, 5188–5192.
27. C. Arrouvel, M. Digne, M. Breyss, H. Toulhoat, and P. Raybaud, *J. Catal.* **2004**, 222, 152–166.
28. C. R. Bealing, W. J. Baumgardner, J. J. Choi, T. Hanrath, and R. G. Hennig, *ACS Nano* **2012**, 6, 2118–2127.
29. G. Wulff, *Z. Krystallogr.* **1901**, 34, 449–530.
30. A. Bravais, *Etudes Crystallographiques*, Academie des Sciences, Paris, **1913**.
31. G. Friedel, *Bull. Soc. Fr. Mineral.* **1907**, 30, 326–455.
32. J. D. H. Donnay, and D. Harker, *Am. Mineral.* **1937**, 22, 446–467.
33. J.-H. Ko, D. Yoo, Y.-H. Kim, *Chem. Comm.* **2017**, 53, 388–391.
34. M. Inoue, and I. Hirasawa, *J. Cryst. Growth.* **2013**, 380, 169–175.
35. K. Kim, D. Yoo, H. Choi, S. Tamang, J. H. Ko, S. Kim, Y.-H. Kim, and S. Jeong, *Angew. Chem. Int. Ed. Engl.* **2016**, 55, 3714–3718.
36. E. Cho, H. Jang, J. Lee, and E. Jang, *Nanotechnology* **2013**, 24, 215201.

## Chapter 5. Summary and Future Perspectives

In this dissertation, multiscale simulation methods have been applied to various crystallization applications. We theoretically studied the crystal structure and morphology of semiconductor materials, and also investigated their mechanisms or dependent properties. Both internal and external factors (i.e., chemical modification, solvent type, ligand interaction depending on the temperature) were considered as factors controlling the crystal structure and morphology.

In Chapter 1, the background of crystallization as well as the factors that influence the crystal structure and morphology during crystallization processes were introduced. Specifically, it has been described in detail that chemical modification, solvent type, and ligand interaction can affect the crystal structures and morphology of semiconductor materials. Multiscale simulation encompassing DFT calculation, Monte Carlo simulation, MD simulation, and morphology models were used to identify unknown crystal structures synthesized in the experiment, and to investigate the fundamental issue of predicting the resulting properties and shape changes.

In Chapter 2, we designed crystal structures using chemical modification including the fluorination of organic molecules and different compositions of small organic molecules. In the case of hexabenzocoronene (HBC), there exists a variable degree of contortion and is easily tuned by functional groups. Contorted HBC (cHBC) is capable of making the molecular shape complementarity with a  $C_{60}$  molecule. Also, through fluorination, the electron withdrawing group can modify the electronic structure of cHBC. Thus, using small organic molecules (i.e., cHBC, fluorinated cHBC (F-cHBC),  $C_{60}$ ), crystal engineering was performed to design solid solutions and cocrystals. Under the given experimental condition, the organic crystal phases were identified through polymorph prediction. With these identified crystal structures, the electro-chemical properties were investigated using Monte Carlo simulation and DFT calculation. For the pristine cHBC crystal structure, an  $R\bar{3}$  crystal phase is formed, and the Li-ions are stored in the vacant site between the bent edge aromatic rings, resulting in a battery-like behavior. For the pristine F-cHBC crystal structure, a  $P2_1/c$  crystal phase is formed, and the Li-ions are stored around the electronegative fluorine atom. Due the strong interaction between fluorine atom and Li-ions, the ion diffusion on the surface is accelerated to reveal pseudocapacitive behavior. In case of the solid solution of cHBC and F-cHBC with 1:1 ratio, a  $P2_1/n$  crystal phase is formed, resulting in both battery and capacitive behaviors. Lastly, the usage of the spherical shaped  $C_{60}$ , resulted in the the cocrystal of cHBC and  $C_{60}$  to form a  $Pnmm$  phase. Due to its doubly concave shape, battery like behaviors were also exhibited better than that of the performance of graphite. Based on these results, the crystal structures were confirmed to be different depending on the molecule and their constituents, resulting in different electrochemical behaviors. This difference in electrochemical performance can be attributed to the difference in adsorption sites caused by the distinctive chemical nature of the molecules.

Based on the crystal engineering studies, the design and control of functional crystalline phase will succeed in obtaining target properties effectively through multiscale simulations.

In Chapter 3, solvent engineering techniques such as solvent-driven and solvent-removing processes are effectively applied to finetune the morphology of perovskite materials. In our experiment, due to the strong coordination between  $\text{Pb}^{2+}$  and oxygen of DMF, the DMF solvent molecules were intercalated into the  $\text{PbI}_2$  to form intermediate phase, so that  $\text{PbI}_2 \cdot \text{DMF}$  crystal was slowly precipitated under the supersaturation condition. The slow precipitation caused many seeds to form, inducing slow crystal growth. As a result, a granular wire shaped  $\text{PbI}_2 \cdot \text{DMF}$  crystal was formed. To figure out the formation mechanism of the granular wire, we firstly investigated the crystal structure of the intermediate phase based on experimental XRD and developed the forcefield parameters of  $\text{PbI}_2 \cdot \text{DMF}$  crystal of intermediate phase. In bulk  $\text{PbI}_2 \cdot \text{DMF}$  crystal,  $\text{PbI}_2$  is periodically bonded along the [100] direction, and the oxygen of the DMF molecule bonded to  $\text{Pb}^{2+}$ . Due to this structural property, the (020) and (011) surfaces have relatively low attachment energies compared to (110),  $(10\bar{1})$ , and  $(11\bar{2})$  surfaces due to the low density of dangling atoms. Lower attachment energies induced a larger surface area due to slow crystal growth. The crystal growth morphology model of  $\text{PbI}_2 \cdot \text{DMF}$  crystal predicted through the attachment energy represented a hexagonal plate shape. The front surfaces of the hexagonal granular composed of (110),  $(10\bar{1})$ , and  $(11\bar{2})$  surfaces exhibited the highest binding energies out of all combination of exposed surfaces. This means the granular can grow in the frontal direction to produce a granular wire shape. In the granular wire morphology, the formulation of numerous grain boundaries and defects on the surface were observed. Such surface characteristics facilitate the generation of deep trap states and band bending, resulting in ultra-high photodetectivity. Solvent engineering enables the effective control of the intermediate crystal structure and morphology of the perovskite material. In addition, the derived morphology can be determined through various crystallization paths depending solvent types with various crystallization methods.

In Chapter 4, for nanocrystals, the ligand and surface energy play a critical role in determining the morphology. In particular, for colloidal nanocrystal such as ZnSe materials, various morphologies may appear depending on the reaction temperature due to the difference in the interaction between the ligand and the exposable surfaces. To investigate effect of temperature on the capping capability of ligands, we calculated the Gibbs free energy using DFT calculation. Generally, as the temperature increases, the absolute adsorption free energy decreases, and the relaxed surface free energy increases. Due to the fact that the free energy values of the most stable (111) and (220) surfaces approach each other, a difference is induced in the equilibrium morphology model. At approximately 230 °C (relatively low temperature), a tetrahedron predominantly surrounded by a (111) surface can be obtained because the oleate ligand strongly binds to the (111) surface. As the temperature increases further, the (220) surface begins to appear at the vertices of the tetrahedron. Due to its

morphology, the electron wavefunctions are more quantum-confined to improve high quantum yield. Through morphological engineering, we can design and successfully obtain a specific morphology that can achieve improved performance.

Overall, these studies demonstrated the design and control strategies of crystal structure and morphology of semiconductor materials. Crystal engineering, solvent engineering, and morphological engineering are expected to improve the electrical and optical performances of each semiconductor material. The database construction of chemical modification and morphology-controlled technologies using solvents and ligands described in the thesis are believed to contribute to the technological advances and resolution of fundamental issues in each field of energy storage and optoelectronic application.

## List of Publications

### First or co-first author [†: equal contribution]

1. Ju Hyun Park, Sun Ha Kim, Jin Chul Kim, Byoung-Young Choi, Sang Kyu Kwak, Oc Hee Hand\*, Yong-Il Kim\*, Seung-Woo Lee\*, “Role of Intercalated Water in Calcium Hydroxide Interlayers for Carbonation Reaction”  
*In preparation*
2. Sang Eun Yoon†, Yongjin Kim†, Ju Hyun Park†, Hyogeun Gwon†, Unjeong Kim, Hyeongjun Kim, Hyungtak Seo, Sang Kyu Kwak\*, Sang-Wook Kim\* Jong H. Kim\*, “Semiconductor-to-Metal Transition in Colloidal Nanocrystal Solids”  
*In preparation*
3. Jaehyun Park†, Ju Hyun Park†, Minseok Yang†, Se Hun Joo, Sang Kyu Kwak\*, Seokhoon Ahn\*, and Seok Ju Kang\*, “Solid Solution of Semiconducting Contorted Small Molecules for High-Performance Li/Na-Ion Host Electrodes”  
*Energy Storage Materials*, **2021**, 36, 123–131.
4. Haewoon Seo†, Ju Hyun Park†, O-Hoon Kwon, Sang Kyu Kwak\*, and Sang-Wook Kim\*, “Highly Qualified InP Based QDs through Temperature Controlled ZnSe Shell Coating Process and Their DFT Calculation”  
*Nanoscale Advances*, **2020**, 2, 5615–5622.
5. Jae Young Noh†, Seungmin Baek†, Ju Hyun Park†, Sang Kyu Kwak\*, and Sang-Wook Kim\*, “Bromine Precursor Mediated Synthesis of Shape Controlled Cesium Bromide Nano-platelets and Their Mechanism Study by DFT Calculation”  
*Inorganic Chemistry*, **2020**, 59(21), 15717–15723.
6. Su Hwan Kim†, Ju Hyun Park†, Eun Min Go†, Woo-Sik Kim\*, and Sang Kyu Kwak\*, “Separation principle of xylene isomers and ethylbenzene with hydrogen-bonded host frameworks via first-principles Calculation”  
*Journal of Industrial and Engineering Chemistry*, **2020**, 85, 276–281.
7. Hye Ji Han†, Ju Hyun Park†, Jin Kyoung Park†, Imanuel Kristanto, Bum Jun Park\*, Sang Kyu Kwak\*, and Sang Hyuk Im\*, “Uniform Ag Nanocubes Prepared by AgCl Particle-Mediated Heterogeneous Nucleation and Disassembly and Their Mechanism Study by DFT Calculation”  
*Small*, **2019**, 15(43), 1904031.
8. Jaehyun Park†, Cheol Woo Lee†, Ju Hyun Park†, Se Hun Joo, Sang Kyu Kwak\*, Seokhoon Ahn\*, and Seok Ju Kang\*, “Capacitive Organic Anode Based on Fluorinated-Contorted Hexabenzocoronene: Applicable to Lithium-Ion and Sodium-Ion Storage Cells”  
*Advanced Science*, **2018**, 5(12), 1801365.
9. Jihye Bong†, Ju Hyun Park†, Taekyung Lim, Seok Ju Kang, Sang Kyu Kwak\*, and Sanghyun Ju\*, “Contact Angle Analysis for the Prediction of Defect States of Graphene Grafted with Functional Groups”  
*Advanced Materials Interfaces*, **2018**, 5(19), 1800166.

## Co-author

10. Yoon Ho Lee<sup>†</sup>, Inho Song<sup>†</sup>, Su Hwan Kim, Ju Hyun Park, Sung O Park, Jeong Hun Lee, Yousang Won, Kilwon Cho, Sang Kyu Kwak\*, and Joon Hak Oh\*, “Perovskite Granular Wire Photodetectors with Ultrahigh Photodetectivity”  
*Advanced Materials*, **2020**, 32(32), 2002357.
11. Gwan Yeong Jung<sup>†</sup>, Eunhye Shin<sup>†</sup>, Ju Hyun Park, Byoung-Young Choi, Seung-Woo Lee, and Sang Kyu Kwak\*, “Thermodynamic Control of Amorphous Precursor Phases for Calcium Carbonate via Additive Ions”  
*Chemistry of Materials*, **2019**, 31(18), 7547–7557.
12. Jaehyun Park<sup>†</sup>, Se Hun Joo<sup>†</sup>, Yoon-Jeong Kim<sup>†</sup>, Ju Hyun Park, Sang Kyu Kwak\*, Seokhoon Ahn\*, and Seok Ju Kang\*, “Organic Semiconductor Cocrystal for Highly Conductive Lithium Host Electrode”  
*Advanced Functional Materials*, **2019**, 29(32), 1902888.
13. Zengmin Tang, Ju Hyun Park, Su Hwan Kim, Jaemin Kim, Junyoung Mun, Sang Kyu Kwak, Woo-Sik Kim\*, and Taekyung Yu\*, “Synthesis of Cu<sub>7</sub>S<sub>4</sub> nanoparticles: Role of halide ions, calculation, and electrochemical properties”  
*Journal of Alloys and Compounds*, **2018**, 764, 333–340.
14. Jaehyun Park<sup>†</sup>, Cheol Woo Lee<sup>†</sup>, Se Hun Joo<sup>†</sup>, Ju Hyun Park, Chihyun Hwang, Hyun-Kon Song, Young Seok Park, Sang Kyu Kwak\*, Seokhoon Ahn\*, and Seok Ju Kang\*, “Contorted polycyclic aromatic hydrocarbon: promising Li insertion organic anode”  
*Journal of Materials Chemistry A*, **2018**, 6(26), 12589–12597.
15. Kyungtae Kim<sup>†</sup>, Minjeong Ha<sup>†</sup>, Byeongwook Choi<sup>†</sup>, Se Hun Joo, Han Sol Kang, Ju Hyun Park, Bongjun Gu, Chanho Park, Cheolmin Park, Jongbok Kim, Sang Kyu Kwak, Hyunhyub Ko\*, Junggho Jin\*, and Seok Ju Kang\*, “Biodegradable, electro-active chitin nanofiber films for flexible piezoelectric transducers”  
*Nano Energy*, **2018**, 48, 275–283.
16. Seungyeol Lee, Seungmin Baek, Joong Pill Park, Ju Hyun Park, Dae Yeon Hwang, Sang Kyu Kwak\*, and Sang-Wook Kim\*, “Transformation from Cu<sub>2</sub>-xS Nanodisks to Cu<sub>2</sub>-xS@CuInS<sub>2</sub> Heteronanodisks via Cation Exchange”  
*Chemistry of Materials*, **2016**, 28(10), 3337–3344.
17. Jihye Bong, Changui Ahn, Taekyung Lim, Ju Hyun Park, Sang Kyu Kwak, Seokwoo Jeon\*, and Sanghyun Ju\*, “Controlled three-dimensional interconnected capillary structures for liquid repellency engineering”  
*RSC Advances*, **2016**, 6(66), 61909–61914.
18. Jihye Bong, Taekyung Lim, Keumyoung Seo, Cho-Ah Kwon, Ju Hyun Park, Sang Kyu Kwak\*, and Sanghyun Ju\*, “Dynamic graphene filters for selective gas-water-oil separation”  
*Scientific Reports*, **2015**, 5:14321.

## Acknowledgements

First and foremost, I would like to express sincere appreciation for my academic advisor Professor Sang Kyu Kwak for the guidance and support during the 8 years of my study and research at UNIST. I have been able to learn how to become a better researcher from all the valuable lessons and will try my best to keep up with the good work.

I would also like to express my gratitude to my committee members Professor Seok Ju Kang, Professor Jiseok Lee, Professor Jun Hee Lee, and Professor Sang-Wook Kim for serving as my committee members as well as their valuable feedback. The guidance and expert advice throughout all the collaborated-researches have surely helped set directions in my doctoral research.

I would also like to thank all my labmates who have helped me throughout my studies in many aspects. Special thanks to Dr. Yuan-jun Gao, Dr. Tae Kyung Lee, Dr. Gwan Yeong Jung, Dr. Eunhye Shin, Dr. Dae Yeon Hwang, Dr. Sung O Park, and Dr. Woo Cheol Jeon who have been able to lead by an example, and also my colleagues Se Hun Joo, Eun Min Go, and Su Hwan Kim. I would also like to thank Jeong Hyeon Lee and Jin Chul Kim who have been very helpful in the various discussions for my research. Also I would like to thank Jiyun Lee, Kyung Min Lee, Hyeong Yong Lim, Hyeongjun Kim, Seonwoo Shin, Yujin Kim, Ji Eun Lee, Seung Hak Oh, Seung Min Lee, and Seong Hyeon Kweon for being such wonderful lab mates, and finally, Kristanto Imanuel, who has personally assisted me a lot in enhancing my English skills.

I would also like to thank my friends Na Kyung Kwon and Huyeon Choi who have always been supportive since my undergrad throughout all my studies. I have personally been able to share so much and earn the courage to continue my studies. I would also like to thank Yu Kyung Shin, Joo Young Lee, and Soyoung Jeon, who have been close friends and supported me throughout the years.

Last but not least, I would like to thank my family, for their support and love. I would like to express special thanks to my parents for all the support they have given, as mentors and as parents who helped me endure the hardships throughout my studies and make plans for my future, as well as my grandmother, who has always believed in me. I would also like to thank my brother, for being supportive and providing motivation.

I would not have been able to make it this far without all the help from the people around me, and would like to express my deepest gratitude, again, to everyone who has helped me make it through my studies.

Sincerely,

Ju Hyun Park



## Acknowledgements (감사의 글)

지난 10년 동안 울산과학기술원에서의 긴 생활을 박사과정을 끝으로 마무리하게 되었습니다. 그동안 많은 분들의 도움과 기원으로 박사학위를 무사히 얻을 수 있었던 것 같아 감사의 글을 전합니다. 무엇보다 저의 지도 교수님 이신 곽상규 교수님께 진심으로 감사하는 마음을 전합니다. 2013년 학부 연구 인턴부터 2020년 박사과정을 마칠 때까지 무려 8년이라는 시간 동안 교수님께서 가르쳐 주셨던 연구자로서의 자세, 열정, 끈기를 통해 독립적인 연구자로 거듭날 수 있었습니다. 연구 뿐만 아니라 인생 전반에 걸친 교수님의 지도로 더욱 성숙한 사람이 될 수 있었습니다. 교수님께서 주신 모든 교훈을 가슴 깊이 새기며, 더욱더 발전하고 성장하여 자랑스러운 제자가 되도록 노력하겠습니다.

또한, 바쁘신 와중에도 기꺼이 저의 박사학위 심사위원을 맡아 주신 강석주 교수님, 이지석 교수님, 이준희 교수님, 김상욱 교수님께도 진심으로 감사의 말씀 올립니다. 학위 과정 동안 공동 연구를 수행할 수 있는 소중한 기회를 주셔서 감사드립니다. 또한, 박사학위 심사기간 동안 교수님들께서 말씀해주신 조언과 격려는 앞으로 제가 수행할 연구 방향 설정에 큰 도움이 될 것입니다.

그리고 연구실 생활을 동고동락하면서 많은 일을 함께 겪어온 연구실 사람들에게도 감사합니다. 앞에서 끌어준 래경, 관영, 은혜, 대연, 성오, 우철 1기수 선배들에게 특히 감사드리며, 같은 동기라서 더욱 위로와 힘이 되어준 세훈, 은민, 수환에게도 고맙다고 전하고 싶습니다. 그리고 후배지만 활발한 디스커션 상대해준 정현, 진철이에게도 고맙다고 말하고 싶습니다. 뿐만 아니라, 지윤, 경민, 형용, 형준, 선우, 유진, 지은, 승학, 승민, 성현에게도 부족한 선배지만 잘 따라와줘서 항상 고맙습니다. 마지막으로, 부족한 나의 영어 실력 향상을 위해 영어 선생님이 되어준 Kris에게도 이 자리를 빌어 감사하는 마음을 전달하고 싶습니다.

학부 시절부터 박사과정까지 바로 옆에서 힘들 때는 진심 어린 위로와 기쁨 때는 자기 일처럼 기뻐하며 축하해준 나경이, 후연이에게 고맙다는 말을 전하고 싶습니다. 박사 과정의 고생을 함께 공감할 수 있는 그들 덕분에 더욱 위로와 용기를 얻을 수 있었습니다. 그리고, 항상 나의 상황을 이해해주고, 배려하여 내 스케줄에 맞춰준 유경이, 주영이, 소영이 모두 너무나 고맙고, 덕분에 스트레스 풀면서 외롭지 않은 대학원 생활을 보낼 수 있었습니다.

끝으로, 세상에서 가장 소중한 우리 가족, 그 동안 무한한 지지와 희생 덕분에 박사학위 과정을 무사히 마칠 수 있었습니다. 학부 졸업하기 전 부모님 앞에서 발표하였던 앞으로의 인생 플랜을 들으시며, 저를 항상 믿어 주시고, 모든 면을 지원해 주셔서 감사드립니다. 사랑합니다. 그리고 그 누구보다 여성스럽고 사랑스러운 우리 할머니에게도 감사의 말씀드립니다. 오래오래 제 곁에서 건강하셨으면 좋겠습니다. 마지막으로, 자신의 꿈을 이룬 멋진 동생 지훈이에게도 그동안 고생 많았고, 누나를 자랑스러워 해줘서 고맙다고 전하고 싶습니다. 앞으로 다가올 새로운 미래 앞에 두려워 하지 말고, 포기하지 않고, 지금처럼 도전하는 자세를 유지하자고 말하고 싶습니다.

지금까지 저는 많은 분들의 도움으로 성장해왔다고 생각합니다. 모든 분들의 성원에 힘입어, 앞으로 더욱 발전하는 훌륭한 연구자가 될 수 있도록 하겠습니다. 감사합니다.

2021년 1월의 어느 날

박 주 현

